THE UNIVERSITY OF
WARWICK

University of Warwick institutional repository: http://go.warwick.ac.uk/wrap

A Thesis Submitted for the Degree of PhD at the University of Warwick

http://go.warwick.ac.uk/wrap/55855

Development and Application of Imaging Techniques for the Investigation of Dentinal Hypersensitivity

Cara Gail Williams

A thesis submitted for the degree of Doctor of Philosophy

Department of Chemistry

University of Warwick

September 2008

THE UNIVERSITY OF

WARWICK

For my parents – I would never have reached this point without you, and I will never be able to thank you enough.

Contents

Chapter 1: Introduction

Chapter 3: SECM & SICM Studies of Fluid Flow through Human and Bovine Dentine, and the Effect of Occlusion Actives on this Flow

Chapter 4: Laser Scanning Confocal Microscopy (LSCM) Studies of the Permeation of Dentine by Rhodamine B

Chapter 5: Localised Dissolution of Enamel

Chapter 6: Carbon as an Electrode Material

List of Figures

Chapter 1: Introduction

Chapter 2: Experimental

Chapter 3: SECM & SICM Studies of Fluid Flow through Human and Bovine Dentine, and the Effect of Occlusion Actives on this Flow

Chapter 4: Laser Scanning Confocal Microscopy (LSCM) Studies of the Permeation of Dentine by Rhodamine B

Chapter 5: Localised Dissolution of Enamel

Chapter 6: Carbon as an Electrode Material

List of Tables

Acknowledgements

Firstly I would like to thank Prof. Julie Macpherson for all her help, patience and guidance throughout my PhD, and for seeing potential in me (no electrochemistry pun intended) when I really couldn't see it myself. Many thanks also to Prof. Pat Unwin, for sharing his knowledge and his ever-present optimism, even when things weren't going so well. Huge thanks must also go to Charlie Parkinson at GSK for all his support and enthusiasm during my PhD and for giving me a fantastic insight into industry.

Thanks to Sara Dale for being my singing partner in the office and a great ear to sound off to when things got hard, and to Anna Colley for her constant stream of gossip and for being a fantastic running partner. Special thanks also to Martin Edwards - your patience knows no bounds, even when I'm having my dimmest moments. You've helped me more over the past few years than I could even begin to tell you, and I really appreciate it. Plus of course you introduced me to Quean's, and my palate is indebted to you for that.

To my fellow members of the C111 crew (massive), thanks for helping the days to go quickly whether experiments were going well or otherwise. To all the members of the Electrochemistry and Interfaces group, past and present, I wouldn't have changed the past four years for anything – thank you.

Thanks must go to Neil Wilson for helpful discussions, and even the odd chocolate biscuit here and there. Thanks to Steve York for his guidance on FE-SEM and not getting annoyed when I was just forgetting something simple. Thanks to Marcus Grant and Lee Butcher for all their help with my rig setup requests, and for the frequent comic interludes. Many thanks to Peter Brindley for the enormous number of SECM cell bodies he made over the duration of my PhD.

Special thanks must go to Lisa for all her love and support, especially over the final stages of writing up when I know I've been a pain in the neck. Finally I would like to thank my family, especially my mam and dad for all their love, support, advice and guidance throughout my PhD. Thank you for giving me the opportunity to achieve this, I appreciate it more than I could ever tell you.

Declaration

The work contained within this thesis is entirely original and my own work, except where acknowledged. I confirm that this thesis has not been submitted for a degree at another university. All Comsol simulations were developed by Martin Edwards. All work on boron-doped diamond was carried out in conjunction with Anna Colley. SMCM and SICM work was carried out with the help of Martin Edwards. AFM images of HOPG were recorded by Manon Guille.

Parts of this thesis have been published as detailed below:

"Examination of the Spatially Heterogeneous Electroactivity of Boron-Doped Diamond Microarray Electrodes", A. L. Colley, C. G. Williams, U. D'Haenens Johansson, M. E. Newton, P. R. Unwin, N. R. Wilson, J. V. Macpherson, *Anal. Chem.* **2006**, *78*(8), 2539-2548.

"Laser Scanning Confocal Microscopy Coupled with Hydraulic Permeability Measurements for Elucidating Fluid Flow across Porous Materials: Application to Human Dentine", C. G. Williams, J. V. Macpherson, P. R. Unwin and C. Parkinson, *Anal. Sci.*, **2008**, *24*, 437–442.

"Scanning Micropipet Contact Method (SMCM) for High Resolution Imaging of Electrode Surface Redox Activity", Cara G. Williams, Martin A. Edwards, Anna L. Colley, Julie V. Macpherson, Patrick R. Unwin, *in preparation.*

"A Realistic Model for the Current Response in Scanning Ion Conductance Microscopy (SICM) and Implications for Imaging", Martin A. Edwards, Cara G. Williams, Anna L. Whitworth and Patrick R. Unwin, *in preparation.*

Abstract

The overall aim of this thesis is to examine the underlying physical basis of dentinal hypersensitivity and to assess methods of treating this cause using imaging techniques. The scanned probe microscopy (SPM) techniques are then extended to the study of carbon-based electrode surfaces, as described in the final chapter.

The use of scanning electrochemical microscopy (SECM), combined with *in situ* pressure-time measurements, is described as a means to investigate the flow of fluid through human and bovine dentine, and the subsequent effect of occlusion treatments on this flow. Scanning Ion Conductance Microscopy (SICM) is also introduced as a technique for imaging dentine, with instrument design and development described, and also calibration of the technique.

Laser scanning confocal microscopy (LSCM) coupled to a constant volume flow-pressure measuring system is introduced as a new technique for the quantitative measurement of fluid flow across porous materials. The methodology described herein firstly allows a ready assessment of the general efficacy of treatments via hydraulic permeability measurements. Second, LSCM images allow the nature of the flow process and the mode of action of the treatments to be revealed at high spatial resolution. For the particular case of dentine, we demonstrate how the method allows candidate treatments to be compared and assessed.

To complement the studies into dentinal hypersensitivity, microscopic dissolution of bovine enamel is investigated. This chapter describes a novel approach, based on SECM, to promote the localised dissolution of bovine enamel, effected by the application of a proton flux to the enamel surface from a UME positioned within 5 μm of the surface, in aqueous solution. The approach results in a well-defined "acid challenge" yielding well-defined etch pits that were characterised using light microscopy and white light interferometry. The effect of etching in the presence of lactate is considered, as is the effect of treating the enamel samples with sodium fluoride prior to etching. The approach described is amenable to mass transport modelling, allowing quantitative interpretation of etch features.

The techniques developed throughout the thesis are applied to the investigation of two types of carbon electrodes: boron-doped diamond (BDD) and highly ordered pyrolytic graphite (HOPG). Heterogeneities in the electroactivity of these substrates are explored.A scanning micropipet contact method (SMCM) is described which promises wide-ranging application in imaging and quantifying electrode activity at high spatial resolution.

Abbreviations

Abbreviation	Description
AFM	Atomic Force Microscopy
BDD	Boron-doped diamond
CV	Cyclic voltammetry /cyclic voltammogram
FE-SEM	Field-emission Scanning Electron Microscopy
HOPG	Highly Ordered Pyrolytic Graphite
LSCM	Laser Scanning Confocal Microscopy
SECM	Scanning Electrochemical Microscopy
SG-TC	Substrate generation-tip collection
SICM	Scanning Ion Conductance Microscopy
SMCM	Scanning Microcapillary Contact Microscopy
TG-SC	Tip generation – substrate collection
UME	Ultramicroelectrode
WLI	White-light interferometry

Glossary of Symbols

Symbol	Description
A	Area of electrode
a	Radius of disc UME
a	Contact radius of the meniscus with substrate
C	Concentration
d	UME-surface separation
D	Diffusion coefficient
F	Faraday's constant
h	Height of the meniscus
h_{syrf}	Height of the surface
h_{UME}	Height of the UME
i	Current
i_t	Current at time t
i_∞	Diffusion-limited current
j	Flux
l	Length of pipette
λ	Wavelength
λ	Pipette semi-angle
n	Number of electrons
η	Overpotential
R	Gas constant
r_{pit}	Radius of etch pit
r_{surf}	Radius of surface

r_p Pipette radius

T Temperature

Chapter 1

Introduction

The overall aim of this thesis was to examine the underlying physical basis of dentinal hypersensitivity and to assess methods of treating this cause using imaging techniques. Two major themes were considered; the first was the flow of fluid through exposed dentine and methods used to retard flow, and the second was the dissolution of the protective enamel layer which covers the porous dentine. The latter was probed using a localised technique which employed an ultramicroelectrode (UME) as a source of protons. The former was investigated using scanned probe techniques and laser scanning confocal microscopy. These scanned probe microscopy (SPM) techniques were then extended to the study of carbon-based electrode surfaces, as described in the final chapter.

Chapter 1 briefly introduces a number of techniques and theories that were important to the studies described herein. These are then explained in more detail in subsequent, specific chapters. The aims of the studies in this thesis are listed at the end of this introductory chapter.

1.1   Dentinal Hypersensitivity

The condition of dentinal hypersensitivity, more commonly known as sensitive teeth, affects a large proportion of the adult population. It arises from the movement of fluid from the pulp in the tooth interior to the mouth. This occurs

when enamel erodes, or gums recess, and the underlying, porous dentine becomes exposed. As such, this thesis is concerned with two main themes: (i) occluding open tubules to prevent the movement of fluid; and (ii) investigating factors which affect the dissolution of dental enamel.

1.1.1   The Structure of the Tooth: Dentine and Enamel

The human tooth consists of two major sections; the crown, which projects from the gum; and the root, which is embedded within the gum. The structure of the tooth is shown in Figure 1.01.
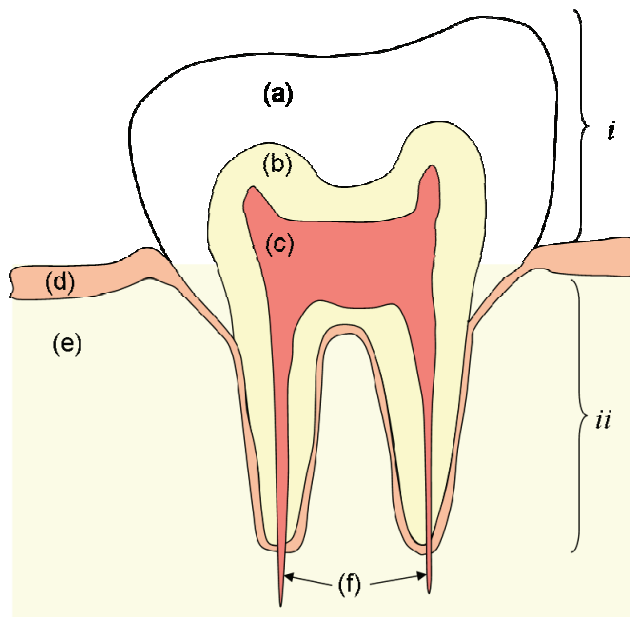
Figure 1.01: The anatomy of the tooth, where *i* is the crown and *ii* is the root of the tooth. (a) is the enamel, (b) is dentine, (c) is the pulp, (d) is the gingiva (gum), and (e) is the bone of the jaw. (f) shows the apical foramen, where the blood and nerve supply enters the pulp.

The crown is covered with enamel, the hardest substance in the body. It consists of 96–98 % (w/w) hydroxyapatite crystals and extends from the underlying dentine to a maximum thickness of *ca.* 2.5 mm.[1] It consists of closely packed

enamel rods, each of which is shaped like a keyhole in cross-section and is *ca.* 5 μm in diameter. In between rods there is a region *ca.* 100 nm in width where the rods pack poorly and some organic material remains.[2] Dentine lies centrally between the enamel and the pulp, and makes up the bulk of the tooth. Dentine is a hard, yellow-white, avascular tissue, consisting of *ca.* 70% calcium hydroxyapatite and *ca.* 30% (by volume) organic component. The organic component is made up of a variety of proteins, mainly collagen.[3] Dentine acts as a supporting material for the brittle enamel. The characteristic feature of dentine is its permeation by closely packed tubules, usually 1-2 μm in diameter, which traverse it completely from the pulp to the enamel.[4] The tubules radiate from the pulp in a near-parallel fashion. The tubules contain cytoplasmic extensions of the odontoblast cells. Odontoblasts are responsible for the initial formation of dentine, and then continue to maintain it.

1.1.2   Dentinal Hypersensitivity

Dentinal hypersensitivity is a common problem within the adult population. It has been defined as a condition "characterised by short, sharp pain arising from exposed dentine in response to stimuli typically thermal, evaporative, tactile, osmotic or chemical and which cannot be ascribed to any other form of dental defect or pathology".[5] It has been estimated to affect approximately 15% of the adult population.[6] Several theories have been proposed to explain dentine sensitivity. One of these hypotheses suggests that odontoblast processes within dentine itself contain sections of nerve fibres, and that these effect sensitivity rather than the nerves in the pulp. Another proposal is that nerve impulses in the pulp are controlled by the release of polypeptides during pulp injury.[7] The most

widely accepted hypothesis to date is the hydrodynamic theory of sensitivity, first proposed in 1900.[8] Supporting evidence was collected in the 1950s and 1960s.[9] When the enamel is eroded or gums recess, the tubules become exposed, and dentinal fluid flows outward due to the positive pulpal pressure in the oral cavity. This fluid flow increases in response to tactile, thermal and osmotic stimuli. The increased flow causes a pressure change across the dentine. This is thought to trigger a mechanoreceptor response in the A-δ nerve fibres of the pulp. The A-δ fibres are associated with the rapid transmission of pain impulses,[10] and thus pain is experienced by the sufferer.[11] If the hydrodynamic theory is to be considered plausible, then tubules must provide an open pathway from the dentine surface to the pulpal nerve tissues. Dye penetration studies have revealed that this is indeed the case in hypersensitive teeth.[12]

1.1.3 Treatments for Dentinal Hypersensitivity

The methods used to treat dentinal hypersensitivity fall into two categories. Occlusive (blocking) treatments aim to occlude the dentinal tubules, and thus retard outward fluid flow or stop it completely. Another approach is to swamp the nerve fibres with K^+ ions, thus preventing the pain response.[13] The mechanism of the potassium ion effect is, as yet, unclear. It has been suggested that K^+ ions exert their effect by sufficiently raising the extracellular K^+ concentration to inactivate intradential nerves. Peacock and Orchardson[14] found the required K^+ concentration to be approximately 10 mM. Hence, the K^+ ions must diffuse along dentinal tubules to achieve this concentration and consequently inactivate nerves at the pulpal end. Stead, Orchardson and Warren[15] proposed a mathematical model for this, supporting the diffusion theory.

McCormack and Davies[16] suggested a model involving the role of a second messenger in the action of K^+.

1.1.4 Sodium Alginate

Alginates are a family of polysaccharides produced by brown algae and bacteria.[17] They are used extensively in the food industry due to their ability to form stable gels in the presence of divalent cations, such as calcium. This gelling process may be exploited to occlude dentinal tubules. The mechanism of gelation has been studied extensively. Morris *et al*[18] showed that calcium ions induce chain-chain associations in alginates. Calcium ions and blocks of guluronic acid residues interact strongly and specifically. These chain-chain associations make up the junctions responsible for gel formation. A model for these junction zones was derived by Grant *et al*[19], known popularly as the "egg-box model". This is shown schematically in Figure 1.02.
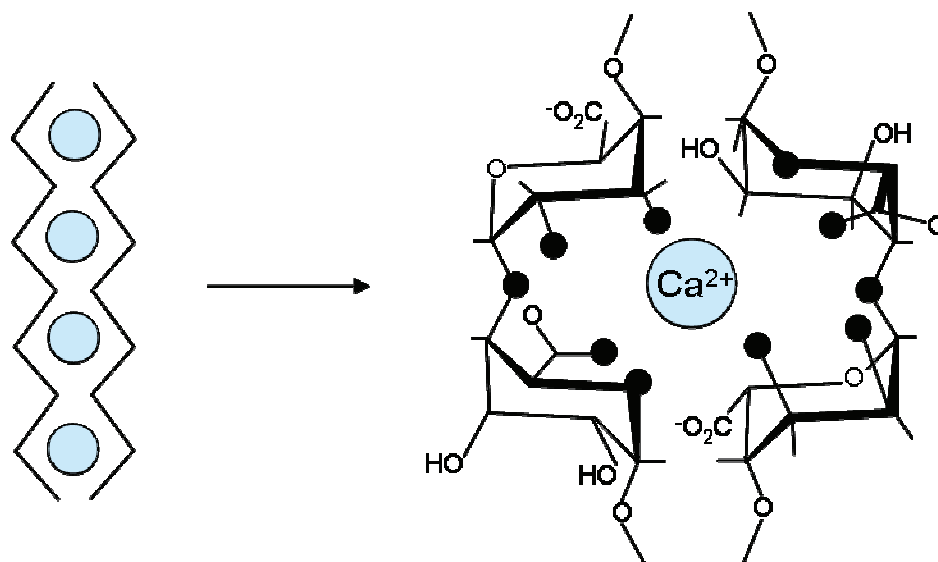
Figure 1.02: Schematic showing calcium coordination in the "egg box model". The dark circles represent the oxygen atoms involved in the coordination of the calcium ion. (Figure adapted from reference 20).

In this model, pairs of helical chains are packed with Ca^{2+} ions positioned between them. However, this model has been criticised as it does not agree with commonly seen Ca^{2+} coordination mechanisms.[20] Mackie *et al*[21] proposed a more realistic coordination pattern, supported by molecular modelling.

1.2 Microscopy

There have been many advances in microscopy since Anton van Leeuwenhoek and Robert Hooke took the first steps in the field during the mid 17th century.[22] Scientists now have a huge range of microscopy techniques at their disposal, ranging from the simpler techniques, such as light microscopy, through to more complicated scanned probe approaches. Those techniques relevant to the studies detailed herein are introduced in this section.

1.2.1 Optical Microscopy

Probably the most well known "traditional" method of examining samples is optical microscopy. A white light source is used to illuminate the sample, and an image is formed via a series of magnifying lenses. The resolution of this technique is limited by both the wavelength of the light source employed and the numerical aperture of the objective lens used.[23] Light propagates as a wave and is thus subject to diffraction. As such, the best possible resolution achievable with standard light microscopy is 200 nm.[24]

A variation on optical microscopy is Differential Interference Contrast (DIC) microscopy.[25, 26] In this method the light is first polarised and then passes through a DIC slider. This slider acts as two Woolaston prisms. As the light

passes from the source of illumination to the sample, the prism interacts with the light to produce two separate wavefronts, termed the ordinary and extraordinary rays. These are polarised perpendicularly to one another, with one lying slightly offset with respect to the other. The two wavefronts then hit the sample and are reflected to slightly varying extents. The light enters the prism once again and the rays are recombined. A rotating analyser is then employed to highlight optical gradients in the specimen as different colours. In the studies on dentine detailed in this thesis, the DIC mode of the optical microscope makes it possible to obtain an estimate of the roughness of the dentine samples. Note that DIC was not used quantitatively here as interpreting the images can be difficult. For example, a region that looks like a peak may indeed be a raised feature, or it may simply be a region of high refractive index.

1.2.2   Scanning Electron Microscopy (SEM)

The development of the electron microscope represented a massive breakthrough in microscopy. The first working (transmission) electron microscopes were constructed by German engineers Ernst Ruska and Max Knoll in 1931. Scanning electron microscopy (SEM) as it exists today did not emerge until the mid 1960s, with the first commercial instrument appearing in 1964.[27]

SEM is used to study surface structure and generally yields easily interpretable images, in contrast with transmission electron microscope (TEM) images which can be difficult to analyse. The electron source produces an electron beam which is accelerated to an energy of between 1 keV and 30 keV. Condenser lenses then focus the beam to a diameter of 2-10 nm before it hits the surface of the

specimen. A number of phenomena occur at the surface as a result of primary electron (electrons from the beam) impact, as shown in Figure 1.03.
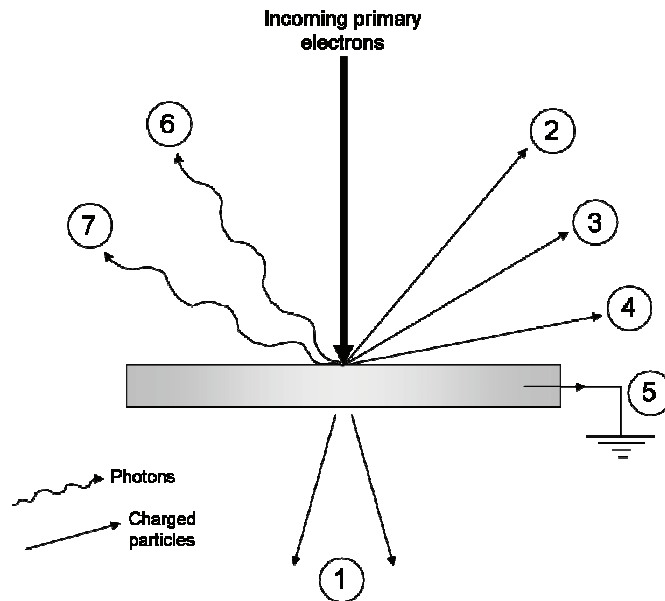
Figure 1.03: Schematic showing photon and charged particle emission from a surface following electron bombardment. 1 = transmitted electrons, 2 = secondary electrons, 3 = backscattered electrons, 4 = Auger electrons, 5 = absorbed current, 6 = X-rays, and 7 = cathodoluminescence. (Figure adapted from ref 27).

Two of these emissions (2 and 3 in Figure 1.03) are of note for SEM. In a thick specimen, the energy of the electron beam is dissipated, which results in low energy secondary electrons being emitted (2). Primary electrons may also collide with atoms in the sample and deflect to the extent that they are "reflected", or backscattered, away from the sample (3). Scanning electron microscopes usually have detectors for both these types of electron. Secondary electrons produce basic topographic images; backscattered electrons can give information on the elementary composition of the specimen.

1.2.3 White-Light Interferometry

White-light interferometry (WLI)[28] is a non-destructive optical profiling method which can be used to investigate surface topography. In a typical interferometer, a beam splitter (a 50% reflective/50% transmitting silvered glass plate) divides the beam into two parts, as shown in Figure 1.04. One beam is reflected from the specimen while the other is reflected from a reference mirror. The beams recombine and interfere as they travel towards the camera. The interferometer is calibrated to give maximum constructive interference at the point of best focus. The combination of the two light paths causes the production of a pattern of light and dark bands, known as fringes.
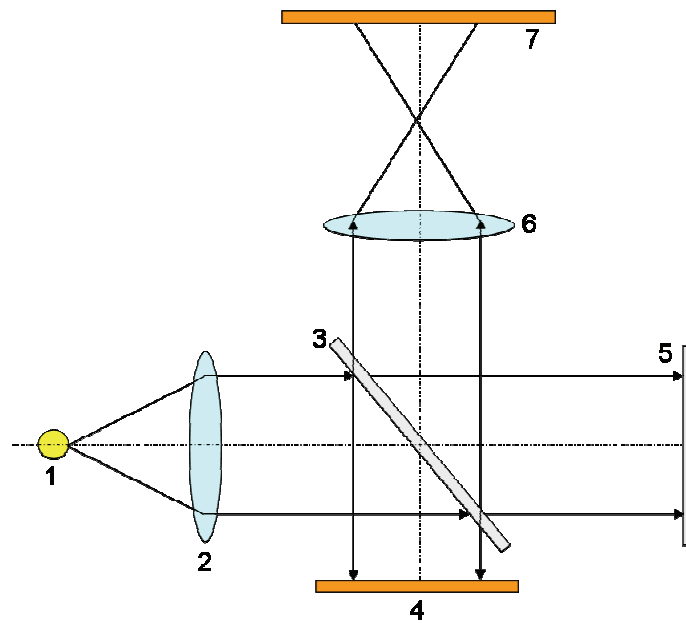
Figure 1.04: Schematic of a white light interferometer. White light from the light source (1) passes through a collimator (2) before being divided by a beam splitter (3). One beam reflects from the sample (4) while the other reflects from a reference mirror (5). They recombine and pass through an objective lens (6) before being detected by the camera (7).

There are two modes of operation: Vertical scanning interferometry (VSI) and phase stepping interferometry (PSI). VSI was utilised in the studies detailed in

this thesis. VSI employs a white light source and allows relatively coarse measurements to be made. The lens scans vertically towards the sample, allowing the height of all points of the sample to be precisely determined, provided that all regions of the sample reflect enough light back to the lens. This is achieved through capture of the pattern of the interference fringes at each point on the sample. This mode of operation allows features as small as a few nm to be discerned in tandem with larger features in the order of 10^2 µm. When using VSI, it is possible to gather images as large as ~ 400 µm x 600 µm in a time frame of ~15 s. PSI allows smaller images (typically tens of µm) to be recorded in one or two seconds. Compared with AFM, introduced in section 1.2.5.1, WLI allows imaging of much larger areas of a sample in much shorter times. However, WLI is restricted to samples which are sufficiently reflective, although this problem may be overcome by coating samples with a thin layer of gold prior to imaging.

1.2.4   Laser Scanning Confocal Microscopy (LSCM)

Laser scanning confocal microscopy (LSCM) is a powerful imaging technique. A laser is used to provide a point source of illumination, there is a point focus within the sample, and there is a detector pinhole, and all three are confocal with one another. These factors combine to minimise interference from lateral stray light, and so maximise contrast in the image formed. Figure 1.05 shows a schematic of the confocal principle.
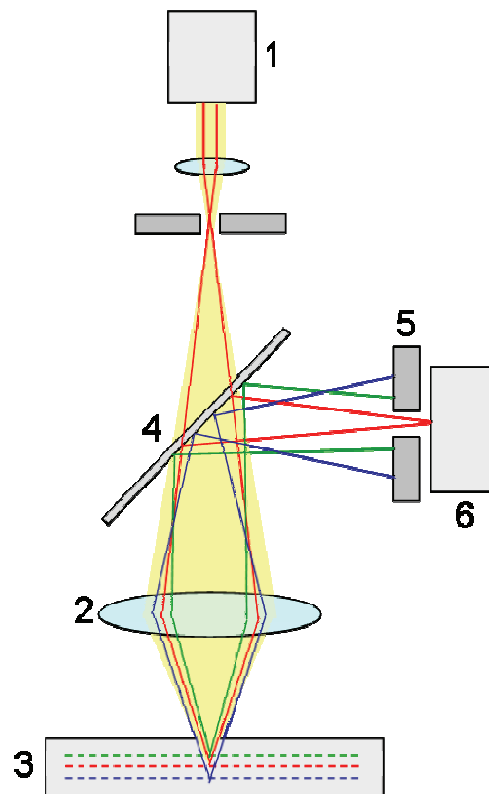
Figure 1.05: The confocal principle. A laser (1) is focused by the objective lens (2) and illuminates the sample (3). Light from the focal place (red) hits the beam splitter (4) and passes through the detector pinhole (5) to the photomultiplier (6). Out-of-focus light (green and blue) is rejected by the pinhole and does not reach the photomultiplier.

The basic steps involved in deriving an image using the confocal microscope may be summarised as follows. The objective lens focuses the laser beam into an hourglass shape. The brightest part is the waist of this hourglass, and this strikes a specific point at a certain depth of the sample. This is achieved either by moving the scanning stage in a raster pattern, computer controlled, or by reflecting the laser with mirrors, effectively moving the laser beam itself. Light emitted from this specific spot is focused to a point and passes through a pinhole. It is detected by a photomultiplier. The pinhole rejects light that would obscure the image, i.e. light reflected by areas of the sample above and below the plane of

interest. The entire plane is scanned in this manner. The spatial resolution of the technique is ultimately governed by the wavelength of laser used.[29] As a rule of thumb, images typically take only a few seconds to acquire, although this obviously depends upon the number of pixels recorded in the image, and the signal-to-noise requirements.

1.2.5 Scanned Probe Microscopy Techniques

1.2.5.1 Atomic Force Microscopy (AFM)

AFM [30-32] is a technique in which topographical information is obtained by scanning a sharp tip attached to a force sensing cantilever over a surface. A schematic of the technique is shown in Figure 1.06.
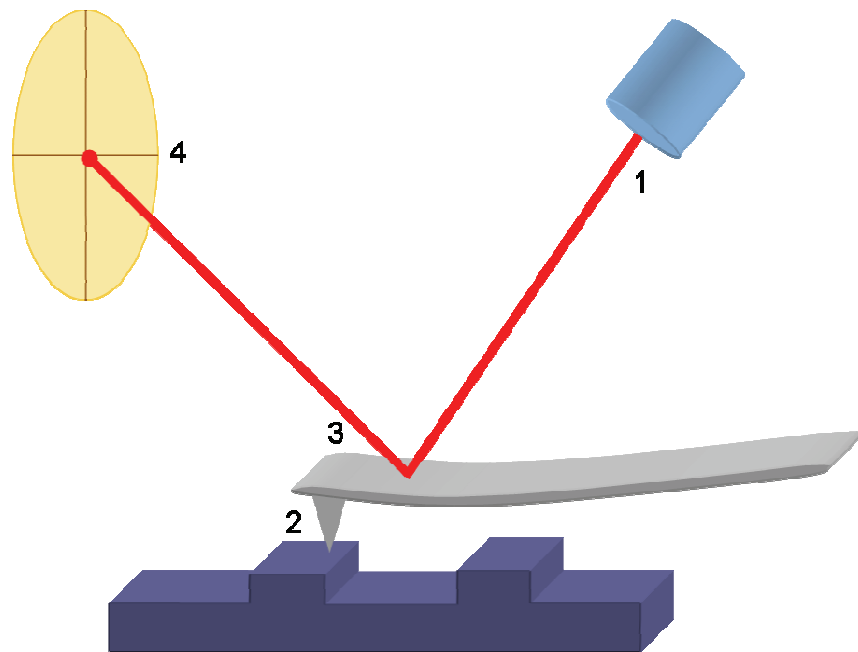
Figure 1.06: Schematic of the atomic force microscope (AFM). A laser beam (1) is shone onto the cantilever as the tip (2) scans across the surface of the sample. The laser reflects off the back of the cantilever (3) into a photodiode detector (4).

Attractive or repulsive forces result in deflection of the cantilever. A laser beam reflected from the back of the cantilever into a photodiode detects the deflections. The AFM is most commonly operated in contact mode[32] or tapping mode. In the studies detailed herein the former was employed, where the sample, attached to a very sensitive piezo positioner, is moved up or down to maintain a constant cantilever deflection. The deflections are used to provide a topographical map of the surface. Lateral resolution is dependent on the radius of curvature of the apex of the tip. Commercially available silicon nitride tips, as used in the studies detailed herein, typically have a radius of curvature of $10 - 40$ nm.[33] A drawback of the technique is the limited *xy* scan size, usually up to a maximum of *ca.* 120 μm. The maximum *z* range is usually *ca.* ± 2.5 μm.

1.2.5.2 Scanning Electrochemical Microscopy (SECM)

SECM is a powerful electrochemical SPM technique which allows topographical imaging and elucidation of electroactivity of a sample. The technique is discussed in depth in section 1.4.

1.2.5.3 Scanning Ion Conductance Microscopy (SICM)

SICM was first reported by Hansma *et al*[34] in 1989. It was developed to allow high resolution imaging of biological samples under physiological solution conditions. The technique employs a micropipette as the imaging probe, and is discussed fully in section 1.5.

1.3 Dynamic Electrochemistry

1.3.1 Introduction

Dynamic electrochemistry is a term which encompasses all studies of the processes occurring at the electrode/electrolyte interface. These processes require the application of a potential to drive them. The consequent current that passes may be analysed to elucidate a huge amount of information about the interface.

In the simplest case, the electrochemical cell is a two-electrode system. This comprises a working electrode and a reference electrode, but may only be used when the current flowing is less than 1 μA. The reaction of interest takes place at the working electrode. The reference electrode has a constant potential. The current that passes between the two electrodes is a measure of the rate of reaction at the working electrode, as defined in equation 1.01:

$$i = nAFj \tag{1.01}$$

Where i is the current, n is the number of electrons transferred, A is the area of the electrode, and j is the flux. This depends on a number of processes, which are summarised in Figure 1.07.[35] Each reaction step (apart from mass transfer) has an associated overpotential; this is the potential which must be applied to provide enough energy to drive that particular process. The overpotential for the overall electrode process is equal to the sum of the overpotentials of these individual elements. The rate of the electrode reaction therefore depends upon the relative ease with which each step occurs.
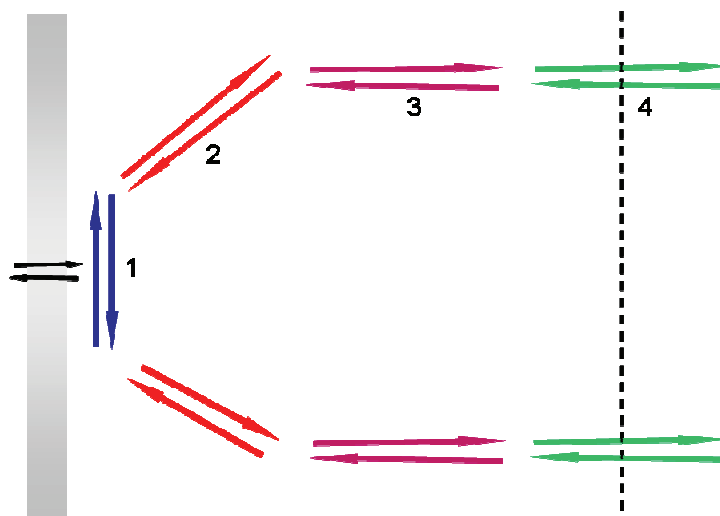
Figure 1.07: Processes occurring at the electrode surface. 1: electron transfer at the electrode surface; 2: Surface reactions such as adsorption/desorption; 3: chemical reactions preceding/following electron transfer; 4: mass transport of the redox active from bulk solution to/from the electrode surface. Figure adapted from reference 34.

In simple electrochemical experiments, electron transfer and mass transport are the only pertinent steps in the reaction. Electron transfer is easily controllable by altering the applied potential and is often very fast, and thus mass transport of the electroactive species to the electrode surface often becomes the rate determining step. There are three modes of mass transport; migration, convection and diffusion. In order to simplify analysis, the effect of two of these mass transport components is removed or made negligible. Any additional convection to that which is present naturally due to thermal considerations may be avoided by preventing the movement of solution in the cell; solutions are not stirred and experiments are carried out on vibrationally-isolated tables. Migration is made negligible by the addition of an excess of an electrochemically inert electrolyte, known as a supporting electrolyte. This increases the conductivity of the solution

and decreases the size of the electrical double layer, acting to provide an alternative, preferable pathway for the current to flow.[36] As such, diffusion is often the limiting factor for the development of a current at the electrode, under mass transfer controlled conditions.

1.3.2 Macroelectrodes vs Ultramicroelectrodes (UMEs)

UMEs first emerged in the early 1970s, and are defined as electrodes with a characteristic feature in the micron or submicron range.[37] UMEs have a range of interesting and useful properties which have led to an enhancement in the variety of experimental timescales and environments that may be studied using electrochemically. UMEs are now used routinely for many electrochemical applications.

The interest in UMEs arose due to their unique properties. These attributes include (i) fast response times, free from non-faradaic contributions;[38] (ii) the capacity to measure the small currents that arise from low analyte concentrations;[39] (iii) the development of a steady-state current response under diffusion-limited control;[40] and (iv) a reduction in ohmic drop effects.[41] Fast response times to changes in applied electrode potential mean that UMEs may be used to monitor electrochemical processes free from capacitative charging on a microsecond timescale. This is particularly useful in the study of short timescale homogeneous and heterogeneous electron transfer processes. In addition, the diminutive size of the UME means that it may be used to probe small volumes, to the extent that *in-vivo* electrophysiological measurements are possible.[42]

The size of the working electrode is an important consideration in electrochemical experiments. First, let us look at the traditional macroelectrode, which may have a diameter in the millimetre or centimetre range. Diffusion to this type of electrode is predominately planar, as shown in Figure 1.08(*i*). In contrast, the small size of UMEs results in extremely efficient diffusional mass transport due to the significant contribution of radial diffusion, resulting in the formation of a steady-state hemispherical diffusion field (in the case of a disc electrode). This is illustrated in Figure 1.08(*ii*). Thus, more rapid and efficient mass transport occurs at a UME than that at a macroelectrode. This has important ramifications for the voltammetric response of UMEs, as discussed in section 1.3.4.
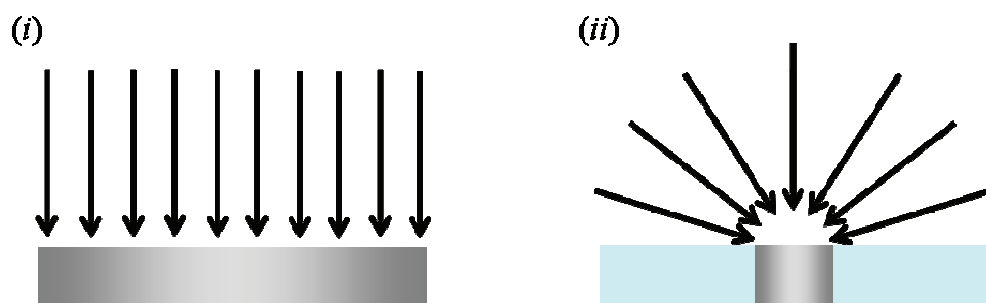
Figure 1.08: Diffusion fields to (*i*) a macroelectrode, and (*ii*) a disc UME.

1.3.3   Ultramicroelectrodes: Fabrication

A number of UME geometries have been developed and applied to various electrochemical applications.[43] These include disc electrodes,[44] band electrodes,[45, 46] hemispherical or spherical mercury electrodes,[47, 48] ring electrodes,[49, 50] and carbon fibre electrodes.[51, 52] For the studies included herein, the most important geometry is the disc UME. These are typically fabricated by sealing a microwire in glass and polishing flat.[53] UMEs fabricated in this manner

17

typically range from 2 μm to 100 μm in diameter. Characterisation is often achieved using two electrochemical techniques: cyclic voltammetry (CV), and scanning electrochemical microscopy (SECM) in conjunction with optical microscopy. These techniques and their application in the characterisation of UMEs are discussed in sections 1.3.4 and 1.4, respectively.

1.3.4 Cyclic Voltammetry (CV)

Cyclic voltammetry (CV) is one of the simplest electrochemical techniques, and is used in most electrochemical investigations to provide information on the electrode/electrolyte interface. This technique provides an "average" response for the surface, ie for heterogeneously active electrode surfaces, it is extremely useful to use other techniques to characterise the interface in order to correctly interpret the voltammetric response of the electrode.

Consider the system $O + e^- \rightarrow R$. In CV, the potential of the working electrode (in this first case, a macroelectrode) is swept from one where no reduction occurs, E_1, to one where electron transfer is driven very quickly, E_2. Upon reaching E_2, the direction of the sweep is reversed and the potential is scanned back to E_1. At E_1, no reduction occurs and so the current is zero. As the potential increases, the rate of reduction increases, and so the current increases approximately exponentially with increasing potential (and thus time), as predicted by the Butler-Volmer equation.[54] The current reaches a maximum value and a peak is seen. This occurs because the current depends not only on the rate constant for reduction, k_{red}, but also on the surface concentration of the redox species. Once this peak in the current is reached, the current is limited by the rate

of mass transport (i.e. diffusion) of reactant to the electrode surface. The fall in current that occurs is due to an increase in the depth of the depleted region next to the electrode and the inability of mass transfer to compete with the rate of electron transfer. Once the sweep reaches the switching potential, E_2, the potential reverses and the reaction proceeds in the opposite direction. The voltammogram takes the form of a mirror image of the forward sweep, but is shifted by $59/n$ mV, as dictated by the Nernst equation (at 298 K). A typical voltammogram obtained for a macroelectrode is shown in Figure 1.09(*i*).
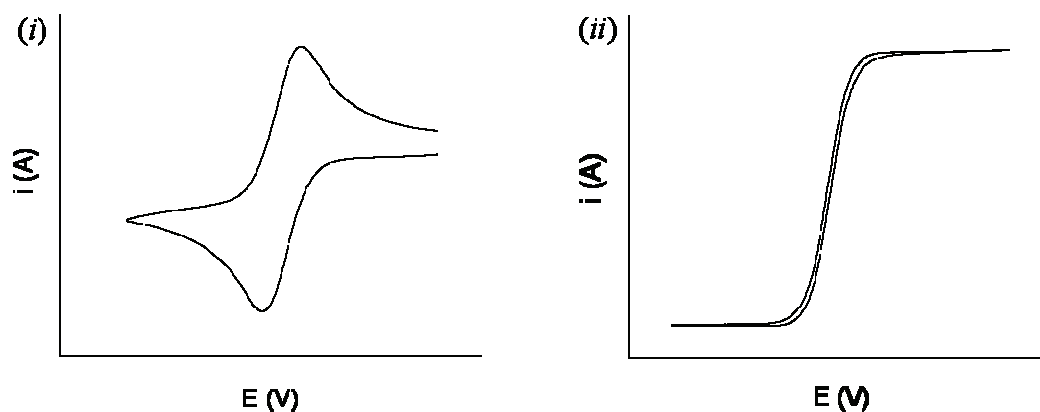
Figure 1.09: Typical shapes of cyclic voltammograms obtained at (*i*) a macroelectrode, and (*ii*) a UME.

The cyclic voltammogram observed for a UME takes a different form to that described above for a traditional macroelectrode. Instead of the peaked reponse, the voltammogram takes a sigmoidal shape, as shown in Figure 1.09(*ii*). A maximum value of the current is observed, and the voltammogram plateaus at this value. This is termed the diffusion-limited current. This value of the current is maintained due to efficient replenishment of reactant at the electrode surface, resulting from rapid hemispherical diffusion to the UME.

CV can be used to verify the size and quality (i.e. how well the wire is sealed into the glass) of an ultramicroelectrode. The current expected at an ultramicroelectrode is given by equation 1.02:

$$i_\infty = 4nFaDc^*$$
(1.02)

where n is the number of electrons transferred, F is Faraday's constant, a is the radius of the UME, D is the diffusion coefficient and c^* is the bulk concentration of the electroactive species in solution. Thus one is able to calculate the expected current and compare it to that achieved experimentally. It is also possible to extract information about the quality of the seal between the microwire and the surrounding glass sheath from the shape of the CV acquired. If the seal is perfect, a CV run at a low scan rate (ie 10 mVs^{-1}) will take the perfect sigmoidal form, as shown in Figure1.09 indicating hemispherical diffusion.

1.3.5   Ultramicroelectrode Arrays

Arrays of UMEs have all the interesting and useful properties of individual UMEs, but with the added advantage of an increased current, i.e. an increased signal-to-noise ratio, which is of great importance for systems involving trace electroanalysis. Under certain conditions, the steady-state current at a UME array is equal to that for a single UME multiplied by the number of electrodes in the array. This is only true for an array of UMEs in which the individual electrodes are spaced a distance greater than $10a$ apart, where a is the radius of the (disc) UME. It also depends on the timescale of the experiment. This is because, for a UME with radius a, the largest diffusion layer that may be formed will span a

distance of *ca*. $10a$ from the UME. The size of the diffusion layer increases with time, and thus high scan rates yield thin diffusion layers, whereas low scan rates yield thick diffusion layers.

Consider an array of UMEs, as shown in Figure 1.10. If the distance between individual UMEs is greater than $10a$, then the diffusion layers will only interact on very long timescales, and the array will have the characteristics of a single UME, but an increased current response equal to the sum of the individual current responses. This is illustrated in Figure 1.10(*i*). However, this situation is complicated when UMEs in an array are separated by less than $10a$. The diffusion layers interact and become pseudo-planar, as shown in Figure 1.10(*ii*). This results in linear diffusion, and the electrochemical response is similar to that of a macroelectrode of the same size as the total size of the array. However, if the scan rate is high enough, the diffusion layers have less time to develop and may not interact.

(i) *(ii)*
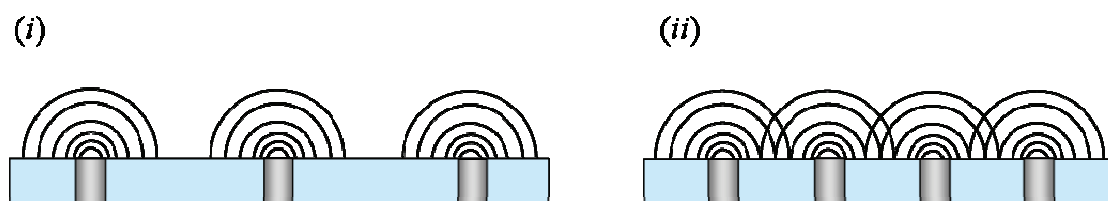
Figure 1.10: Diffusion profile at a UME array when the individual electrodes are spaced by (*i*) > $10a$ and (*ii*) <$10\,a$.

UME arrays may be fabricated in a variety of ways[55-59] and applied to research in areas such as environmental analysis,[60] biomedical applications[61] and drug development.[62] Heterogeneous surfaces which contain regions of electroactivity

on the micron scale in an insulating (or low activity) matrix may be considered as UME arrays. Studies on such a substrate are discussed in Chapter 6

.

1.4   Scanning Electrochemical Microscopy (SECM)

1.4.1   Introduction

Among chemical mapping techniques, scanning electrochemical microscopy (SECM)[63, 64] is particularly popular and now well established for imaging both surface topography[65] and the chemical reactivity of substrates.[66] SECM utilises an UME as a scanning probe, the response of which provides information on an underlying substrate. When preparing a UME for use in SECM, it is important to consider the ratio of the radius of the insulator to radius of the wire, the *RG* value, as described by equation 1.03:

$$RG = \frac{r_{insulator}}{a}$$
(1.03)

where $r_{insulator}$ is the radius of the insulating glass sheath surrounding the wire and *a* is the radius of the wire itself. Typically for SECM disc UMEs are fabricated with an *RG* value of 10.

There is a growing family of SECM operation modes,[67] among which the feedback mode[68] and generation/collection modes are the most used to investigate electrode surfaces and related interfaces. In the feedback mode, the tip is used to generate a redox species from a precursor in solution, in close proximity to a sample surface. The current that flows as a function of

tip/substrate separation provides information on the surface electroactivity. In the generation-collection modes, one working electrode generates a species which is then collected by the second electrode. Tip generation-substrate collection (TG-SC) can be used to investigate local heterogeneous kinetics,[69, 70] including coupled chemical reactions,[71] while the substrate generation-tip collection (SG-TC) mode has been used to probe a wide variety of electrochemical reactions and at heterogeneous electrode surfaces.[72-74] The resolution of SECM is limited by the diameter of the UME probe,[68] the tip-substrate separation and the detection mode employed.

1.4.2   Feedback Mode of the SECM

Consider case 1, shown in Figure 1.11(*i*). A UME approaches an insulating substrate. A potential is applied to the UME in order to reduce electroactive species O (present in solution) to species R at a diffusion limited rate, which leads to generation of a current, i_∞, at the tip electrode. As the UME gets closer to the surface, the hemispherical diffusion to the tip becomes hindered, and as such the current generated begins to decrease in magnitude. This is known as negative feedback. It is possible to plot curves showing i_t/i_∞ vs d, where i_t is the current at the tip, i_t/i_∞ is the normalised current, and d is the distance between the electrode and the surface. These are known as approach curves. Theoretical approach curves may be constructed using the tables of Kwak and Bard [68] and experimental data compared to them.
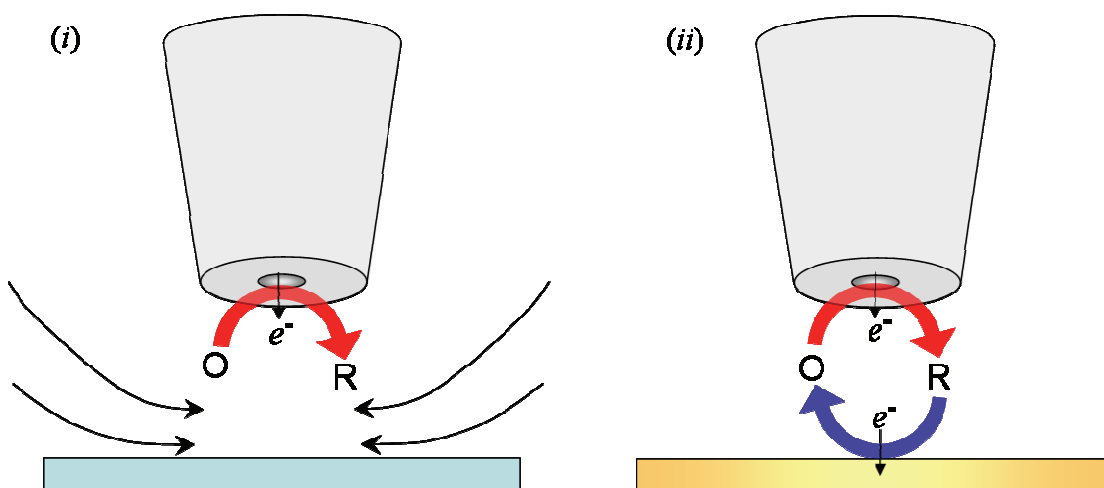
Figure 1.11: Schematic (not to scale) of SECM feedback modes. (*i*) shows how hindered diffusion leads to negative feedback; (*ii*) illustrates regeneration of the redox mediator, which leads to positive feedback.

In case 2, shown in Figure 1.11(*ii*), the UME approaches a conducting substrate. In this situation, when the UME reaches a certain tip-surface separation, species R which has been generated at the tip is oxidised back to species O at the surface. This leads to an increasing concentration of species O being provided for reduction at the UME, and as such an increase in the current is seen. This is termed positive feedback. Theoretical approach curves for conducting surfaces may be plotted in a similar manner to those for insulating surfaces. Theoretical approach curves for both negative and positive feedback are shown in Figure 1.12.
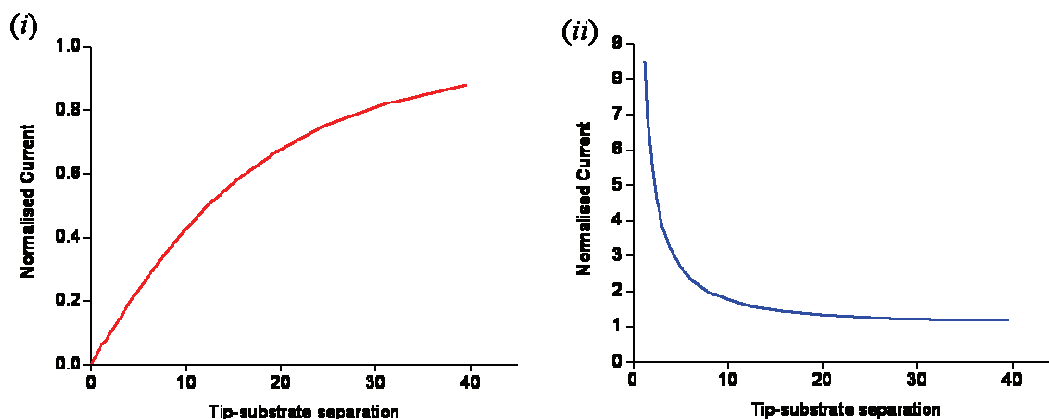
Figure 1.12: Theoretical approach curves for (*i*) negative feedback and (*ii*) positive feedback for a 25 μm diameter disc UME.

Approach curves may be used in a number of ways. If the nature of the substrate is fully known and understood, the approach curve may be used to characterise the tip UME and experimental set-up. For example, if a perfectly flat glass disk is employed as the substrate, then this may be assumed to be a perfect insulator. A UME is considered sufficiently flat for use in SECM if a normalised current which is less than 10% of the bulk current is reached before the curve plateaus. This plateau indicates that the UME is touching the substrate. If the UME (and the substrate) are perfectly flat, then there should be no space for the redox species to diffuse to the UME at touch and hence there should be zero current. However, in practice this is almost impossible to achieve, and so a current of less than 10% of bulk at touch is considered sufficient, i.e. the electrode and substrate are well aligned and the UME is well polished.

The feedback mode may also be used to characterise surfaces that exhibit intermediate behaviour between insulating and conducting, or those which are a heterogeneous mixture of the two regimes. However it is necessary to know that

these variations in current are due to surface kinetics/conductivity and not sample topography (see below) It is possible to simulate approach curves for these surfaces.

1.4.3   SECM: Probing surface topography and activity

SECM is a powerful technique for elucidating the topography of an insulating substrate. The most commonly employed method for achieving this is fixed-height imaging. An approach curve is carried out to the substrate and fitted to the theoretical curve. This allows the UME to be positioned a known distance from the surface, generally *a*. A constant potential is applied to the UME, typically to maintain the diffusion-limited current. The UME is then scanned across the sample at this constant height. As the topography of the substrate changes underneath the tip, the tip-substrate separation changes and thus the measured current varies in accordance with the negative feedback approach curve, as shown in Figure 1.13 (*i-iii*). A map of the surface topography may then be plotted.
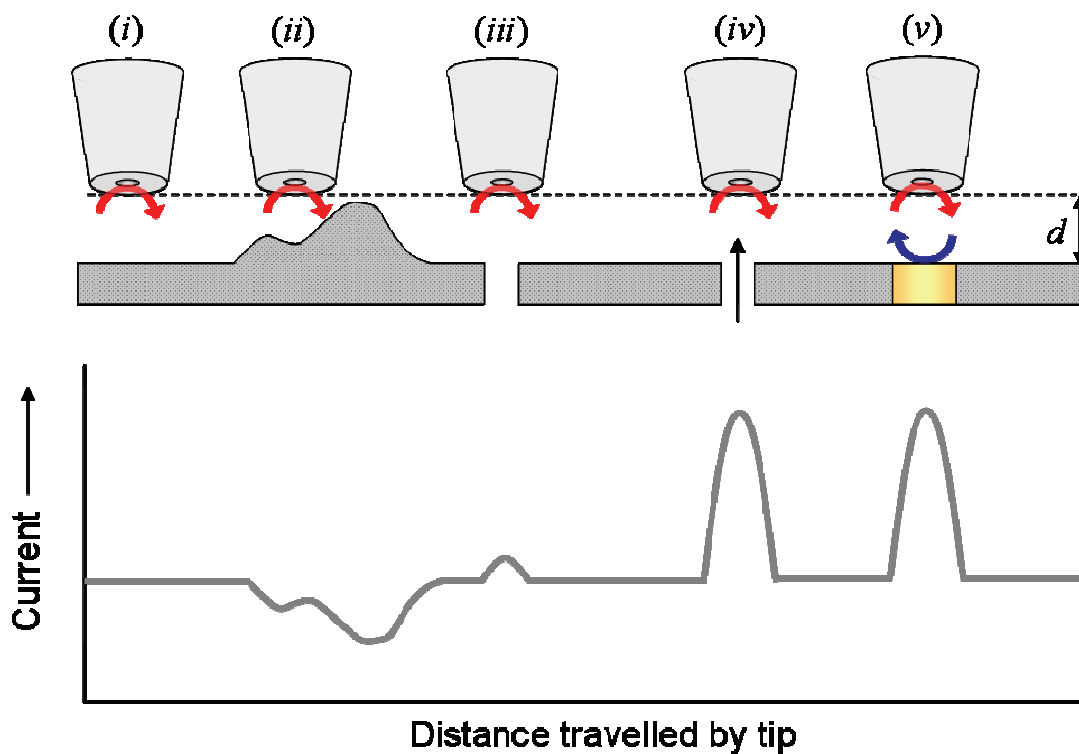
Figure 1.13: An illustration of the varying feedback modes of SECM. The tip is scanned at a fixed height, so the tip-substrate separation, *d,* and thus the current, changes as the topography of the surface changes (*i-iii*). Addition of convection to a porous system causes large current increases (*iv*). The presence of electroactive regions may also be confirmed by large increases in current (*v*).

If the substrate has heterogeneous regions of activity (be it transport or electroactivity) these regions can act to modify the current at the UME compared to negative feedback, and thus there will be an increase in the current in these regions compared with the surrounding areas. One mechanism via which this can occur is flow of fresh solution through a porous sample, as shown in Figure 1.13 (*iv*), the addition of convection to the diffusive response of the electrode. In this thesis, this characteristic of SECM is exploited in order to map the permeability of dentine samples, and the subsequent effect of treatments on this permeability.

The second mechanism is electron transfer in amenable regions of the sample, as shown in Figure 1.13 (*v*), i.e. positive feedback, as described above in section 1.4.2.

Note that many substrates are heterogeneously active and exhibit both insulating and conducting behaviour. There is a second mode of operation of SECM, substrate generation-tip collection (SG-TC) mode, which can accentuate the differences between conducting and insulating regions. In this case, the substrate is biased at a potential to generate an electroactive species of interest, whilst the tip UME is biased at a suitable potential to collect this species of interest at a diffusion-controlled rate. Thus, a map of the electroactivity of the substrate is revealed, with a spatial resolution determined by the dimensions of the UME. For efficient profiling of the diffusional activity of the substrate small cone-shaped electrodes, with minimal insulating sheaths, are often preferred so as not to perturb the resulting diffusion profile too much during tip collection. This is shown schematically in Figure 1.14.[75, 76]
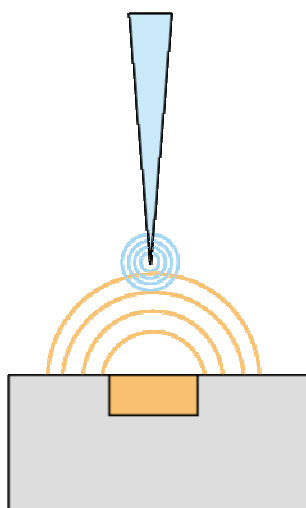
Figure 1.14: Schematic showing the interaction of diffusion fields in the SG-TC mode of SECM.

Commonly, UMEs with diameters of 25, 10, 5 and 2 μm are employed. [77-81] Although probe electrodes with characteristic dimensions of less than 1 μm have been fabricated,[82-85] they have proved generally difficult to reproduce, characterise and deploy as imaging probes. Edge diffusion to the tip in all SECM modes and overlapping diffusion fields of neighbouring active sites in SECM substrate generation-tip collection may lead to loss of lateral resolution in SECM measurements.

1.5   Scanning Ion Conductance Microscopy (SICM)

The scanning ion conductance microscope (SICM) was first developed by Hansma and co-workers in 1989.[34] This scanned probe microscope employs a micropipette as the scanning probe, where the resolution is ultimately determined by the radius of this micropipette. The sample sits in an inert electrolyte solution, and as such the technique has been utilised for the study of biological substrates. These studies include imaging of living cells,[86] cell volume measurement,[87] and the measurement of local Ca^{2+} concentrations in cardiac myocytes.[88]

In this project, the aim was to use SICM to study ion transport across synthetic and biological membranes.

1.5.1   Principles and Instrumentation

The SICM consists of a micropipette which is scanned over the sample. The micropipette tips are prepared from standard borosilicate capillaries using a laser puller, and typically have diameters in the range 500 nm – 4 μm. The laser puller allows highly reproducible tips to be fabricated quickly and simply. The sample

sits in an inert electrolyte solution (for example NaCl or KCl). The micropipette contains an intrapipette Ag/AgCl electrode. A potential, V, is applied between this and an external Ag/AgCl electrode placed in the solution. An ion migration current flows between the Ag/AgCl electrodes. A schematic of the basic SICM set up is shown in Figure 1.15.
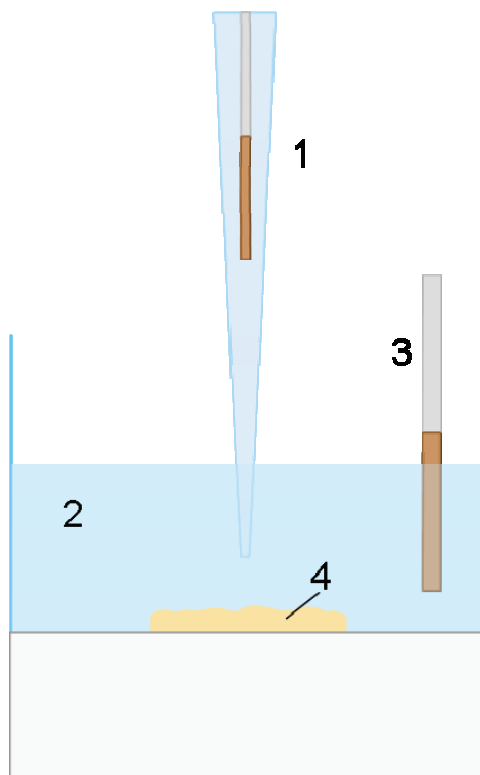
Figure 1.15: Schematic showing the SICM experimental set-up. A micropipette tip containing an intra-pipette Ag/AgCl reference electrode (1) is filled with an inert electrolyte solution, as is the reservoir (2). A second Ag/AgCl reference electrode (3) sits in the reservoir and a potential is applied between the two electrodes. The magnitude of the resulting migration current that flows is dependent on the distance between the tip and the sample (4).

The magnitude of the ion current, i, that flows is determined by the overall resistance, R. R is a combination of micropipette resistance, R_p, and the access resistance of the micropipette aperture, R_{ac}. These resistances are shown schematically in Figure 1.16. The ion current is given by Equation 1.04:

$$i = V(R_p + R_{ac})$$ (1.04)
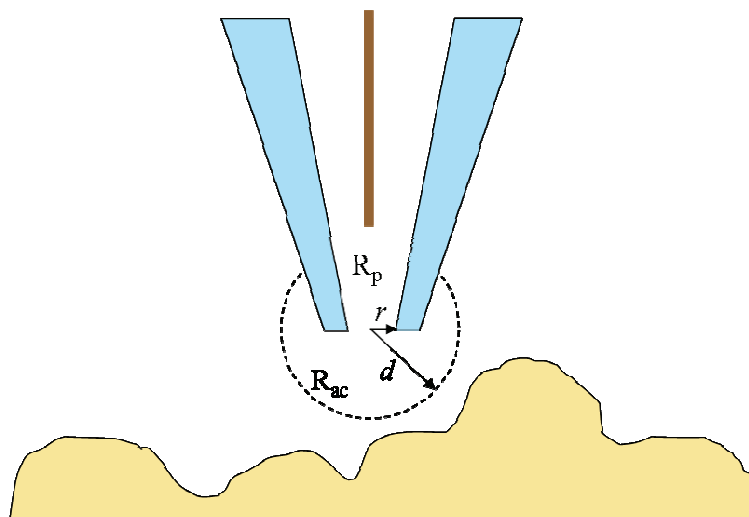
Figure 1.16: Schematic showing the resistances associated with the SICM technique. R_p is the resistance of the pipette opening; R_{ac} is the access resistance of the pipette. *r* is the radius of the pipette and *d* is the tip-substrate separation.

The SICM has a number of modes of operation. The most simple is constant height mode, where the tip is scanned across the surface at a particular distance. However this mode is susceptible to tip crash as prominent features can easily break the probe. A more ideal method of operation is to keep the tip at a constant distance from the substrate, ie to keep the current constant. This requires a feedback mechanism, which is discussed in detail in Chapter 3.

1.6   Carbon as an Electrode Material

Currently in the field of electrochemistry, there is a great deal of interest in carbon-based electrode materials. These range from the more established forms

of graphite-based electrode, such as glassy carbon (GC),[89-92] highly ordered pyrolytic graphite (HOPG), and carbon fibres,[93] through to the much discussed area of carbon nanotubes[94-98] and their derivatives,[99-102] and also include boron-doped diamond (BDD) electrodes[103-106] which are beginning to emerge as excellent electrode candidates. In this thesis, the local electroactivity of polycrystalline BDD was investigated using SECM. To extend this work a new technique, the scanning micropipette contact method (SMCM), has been developed and used to further study BDD and highly ordered pyrolytic graphite (HOPG).

1.6.1   Boron-Doped Diamond (BDD)

Boron-doped diamond (BDD) has been touted as an interesting electrode material in the areas of electroanalysis[107] and electrosynthesis.[108] Intrinsic diamond is one of the best known natural insulators, with a resistivity greater than 2×10^{15} Ω cm.[109] However, on doping with boron, this resistivity may be reduced to 0.1 Ω cm. Moreover, at sufficiently high dopant densities ($> 2 \times 10^{20}$ boron atoms cm^{-3}), the material becomes metallic.[110] BDD possesses a number of useful properties. It exhibits a very wide potential window (ca. -1.35 V to 2.3 V vs NHE) in aqueous solution, generates very low background currents, and is stable in aggressive media.[107, 108, 111] BDD is produced by chemical vapour deposition (CVD) techniques as shown in Figure 1.17.
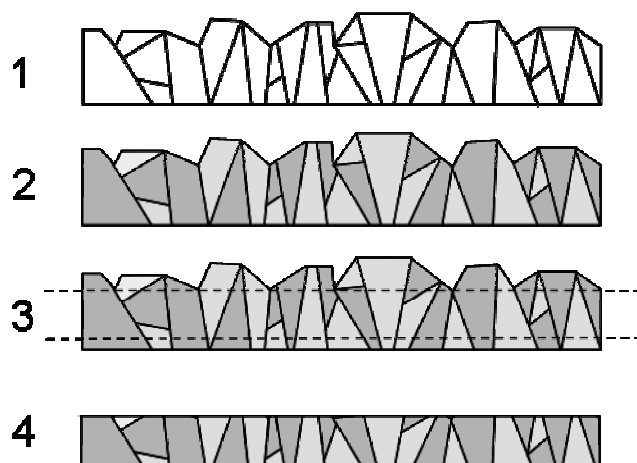
Figure 1.17: (1) Schematic showing grain structure of a polycrystalline diamond film. (2) Differential boron uptake in different grains is indicated by dark and light regions. (3) The sample is processed to remove the growth and nucleation surfaces. (4) Resultant sample for investigation; note the complex interconnection of grains with different dopant densities.

The electrochemical response of BDD may be affected by three major factors. The first is dopant density; as mentioned above, at boron levels > 2 x 10^{20} the material undergoes a transition from p-type semiconducting to semimetallic. This is known as degenerative doping.[112, 113] The second factor is surface termination. The surface of BDD may be hydrogen- or oxygen-terminated. The surface chemical functionality can have a dramatic effect on the electron-transfer kinetics of certain redox species.[114, 115] For example, it has been reported that oxygen-termination severely inhibits the electron-transfer kinetics for the $Fe(CN)_6^{3-/4-}$ couple compared with a hydrogen-terminated surface.[114, 116] The third factor which may influence BDD's electrochemical response is the purity of the growth process. In certain cases, the CVD process may yield some non-diamond, sp^2-bonded carbon, and this will show differing activity from the surrounding BDD material.[117, 118]

1.6.2 Highly Ordered Pyrolytic Graphite (HOPG)

Highly ordered pyrolytic graphite (HOPG) is a highly anisotropic carbon material that is thought to exhibit differing electron transfer kinetics on its basal plane and edge plane sites. This anisotropy can lead to complications in analysing electrochemical data yielded by HOPG electrodes. Changes in capacitance and electron transfer kinetics are observed which depend on randomly created defects arising from surface cleaving.[119] This has been confirmed in studies which have shown that treating the HOPG surface using a laser[120] or electrochemical pre-treatment[121] also effects significant changes in electron transfer rates.

1.6.3 Scanning Microcapillary Contact Method (SMCM)

It is possible to utilise glass microcapillaries, as described in section 1.5, for localised electrochemical measurements. A scanning micropipette contact method (SMCM) has been developed which promises to have wide-ranging application in the field of electrochemistry. SMCM makes it possible to perform highly localised electrochemical experiments. Heterogeneous electrode surfaces may be investigated without the substrate being immersed in solution. This eliminates the problem of overlapping diffusion fields from active sites located adjacent to one another, as may be encountered in SECM. In SMCM, the scanning micropipette probe is brought directly into contact with the sample, and as such no difficulties arise from tip-substrate separation considerations as may be the case with SECM and SICM. The micropipette probes are simple to fabricate, highly reproducible and inexpensive.

1.7   Aims of the Thesis

The overall aim of this thesis was to develop a sound understanding of the nature of fluid flow through dentine, and to explore the effects of a potential active on this fluid flow. In this opening chapter, the problem of dentinal hypersensitivity has been introduced, with reference to the structure of dentine. Sodium alginate, a potential active in the treatment of dentinal hypersensitivity, has been discussed, as have the techniques utilised in this thesis for investigating fluid flow through dentine, including SECM and LSCM.

The instruments, experimental setups and apparatus used are discussed in Chapter 2. Specific details relating to each technique are discussed in the relevant chapters.

Chapter 3, the first results chapter, describes the use of SECM to investigate fluid flow through bovine dentine. The effect of the redox mediator is examined and optimised in order to allow the fluid to flow as freely as possible through the substrate. The subsequent effect of sodium alginate on this fluid flow is explored over a range of pH values. SICM is introduced as a complementary technique for high resolution imaging of the dentine substrate. The development and calibration of the SICM is described.

In Chapter 4, LSCM is introduced as a new complementary approach for imaging flow across porous materials, supported by a simple method for measuring hydraulic permeability. Again, the effect of sodium alginate gel on this fluid flow is investigated, but in this case a larger area of the dentine surface

is captured than is possible using SECM or SICM. The effect of a commercial varnish (Cervitec ®) on the fluid flow is also explored.

Acid dissolution of dental enamel is a common problem, and leads to exposure of the underlying dentine. Once the dentine is exposed, dentinal hypersensitivity can develop. Thus to complement the studies into dentinal hypersensitivity, in Chapter 5, the microscopic dissolution of bovine enamel was investigated. The chapter describes a novel approach, based on SECM, to promote the localised dissolution of bovine enamel, effected by the application of a proton flux to the enamel surface from a UME positioned within 5 µm of the surface, in aqueous solution. The approach results in a well-defined "acid challenge" yielding well-defined etch pits that were characterised using light microscopy and white light interferometry.

Finally, Chapter 6 describes the application of the techniques developed throughout the thesis to the investigation of two types of carbon electrodes: boron-doped diamond (BDD) and highly ordered pyrolytic graphite (HOPG). Heterogeneities in the electroactivity of these substrates are explored.

Conclusions are drawn and described in Chapter 7.

1.8   References

(1)   J.B. Kerr in *Atlas of Functional Histology*; Mosby: London, 1999, pp 220.

(2)   N. Rao in *in Textbook of Oral and Maxillofacial Anatomy, Histology, and Embryology*; Prabhu, S. R., Ed.; Oxford University Press: Oxford, UK, 2006.

(3)   R.M. Carvalho, M. Yoshiyama, E.L. Pashley, D.H. Pashley *Archs. Oral Biol.* **1996**, *41*, 369-377.

(4)   M. Addy, G. Embery, W.M. Edgar, R. Orchardson in *Tooth Wear and Sensitivity: Clinical Advances in Restorative Dentistry*; Taylor & Francis: London, 2000, pp 8.

(5)   G.R. Holland, M.N. Narhi, M. Addy, M. Gangarosa, R. Orchardson *J. Clin. Periodont.* **1997**, *24*, 808.

(6)   R.H. Dababneh, A.T. Khouri,, M. Addy *Br. Dent. J.* **1999**, *187*, 606.

(7)   P. Dowell, M. Addy *J. Clin. Periodont.* **1983**, *10*, 341.

(8)   A. Gysi *J. Dent. Sci.* **1900**, *43*, 865.

(9)   M. Brännström in *Sensory Mechanisms in Dentine*; Anderson, D. J., Ed.; Pergamon Press: Oxford, 1962, pp 73-79.

(10)   http://www.neuropathy-trust.org/mainpages/education/pn/definitions.htm.

(11)   J.V. Macpherson, P.R. Unwin *Electroanalysis* **2005**, *17*, 197-204.

(12)   E.G. Absi, M. Addy, D. Adams, *J. Clin. Periodont.* **1987**, *14*, 280.

(13)   A. Vander, J. Sherman, D. Luciano, in *Human Physiology: The Mechanisms of Body Function,* 8th ed.; McGraw-Hill: New York, 2001, pp 175-196.

(14)   J.M. Peacock, R. Orchardson *J. Dent. Res.* **1995**, *74*, 634.

(15)   W.J. Stead, R. Orchardson, P.B. Warren *Archs. Oral Biol.* **1996**, *41*, 679.

(16)   K. McCormack, R. Davies *Pain* **1996**, *68*, 5.

(17)   I. Donati, S. Holtan, Y.A. Mørch, M. Borgognam, M. Dentini, G. Skjåk-Bræk *Biomacromolecules* **2005**, *6*, 1031.

(18)   E.R. Morris, D.A. Rees, D. Thom, J. Boyd *J. Carbohyd. Res.* **1978**, *66*, 145.

(19)   G.T. Grant, E.R. Morris, D.A. Rees, P.J.C. Smith, D. Thom *FEBS Lett.* **1973**, *32*, 195.

(20)   I. Braccini, S. Pérez *Biomacromolecules* **2001**, *2*, 1089.

(21)   W. Mackie, S. Pérez, R. Rizzo, F. Taravel, M. Vignon *Int. J. Biol. Macromol.* **1983**, *5*, 329.

(22)   W.J. Croft *Under the Microscope: A Brief History of Microscopy*; World Scientific, 2006.

(23)   J.H. Richardson *Optical Microscopy for the Materials Sciences*; Marcel Dekker: New York, 1971.

(24)   M. Spencer *Fundamentals of Light Microscopy*; Cambridge University Press: Cambridge, 1982.

(25)   S.H. Kang, S. Lee, E.S. Yeung *Anal. Chem.* **2004**, *76*, 4459.

(26)   H-W. Li, M. McCloskey, Y. He, E.S. Yeung *Anal. Bioanal. Chem.* **2007**, *387*, 63.

(27)   I.M. Watt *The Principles and Practice of Electron Microscopy*, 2nd ed.; Cambridge University Press: Cambridge, 1997.

(28)   F. Mücklich in *Handbook of Microscopy:Applications in Materials Science, Solid-State Physics and Chemistry*; S. Amelinckx, D. van Dyck, J. van Landuyt, G. van Tendeloo, Ed.; VCH: Weinheim, 1997, pp 49.

(29)   C.J.R. Sheppard, D.M. Shotton *Confocal Laser Scanning Microscopy*;
        Bios Scientific Publishers: Oxford, 1997.

(30)   G. Binnig, C.F. Quate, Ch. Gerber *Phys. Rev. Lett.* **1986**, *56*, 930.

(31)   D. Rugar, P.K. Hansma *Physics Today* **1990**, *43*, 23.

(32)   C.F. Quate *Surface Science* **1994**, *299*, 980.

(33)   P. Neuzil, R. Nagarajan *J. Micromech. Microeng.* **2006**, *16*, 1298.

(34)   P.K. Hansma, B. Drake, O. Marti, S.A.C. Gould, C.B. Prater *Science*
        1989, *243*, 641-643.

(35)   A.J. Bard, L.R. Faulkner in *Electrochemical Methods: Fundamentals and
        Applications,* 2nd ed.; Wiley: New York, 2001.

(36)   C.H. Hamann, A. Hamnett, W. Vielstich *Electrochemistry*; Wiley-VCH:
        Chichester, 1998.

(37)   R.J. Forster *Chem. Soc. Rev.* **1994**, *23*, 289.

(38)   P. Bindra, A.P. Brown, M. Fleischmann, D. Pletcher *J. Electroanal.
        Chem.* **1975**, *58*, 31.

(39)   P. Norouzi, M. Namazian, A. Badiei *Anal. Sci.* **2004**, *20*, 519.

(40)   R.M. Wightman *Anal. Chem.* **1981**, *53*, 1125A.

(41)   A.M. Bond, M. Fleischmann, J. Robinson *J. Electroanal. Chem.* **1984**,
        168, 299.

(42)   R.M. Huff, R.N. Adams *Neuropharmacology* **1980**, *19*, 587.

(43)   R.M. Wightman *Science* **1988**, *240*, 415.

(44)   R.M. Wightman, D.O. Wipf *Electroanalytical Chemistry: A Series of
        Advances*; A.J. Bard (Ed.), Marcel Dekker: New York, 1989.

(45)   K.R. Wehmeyer, M.R. Deakin, R.M. Wightman *Anal. Chem.* **1985**, *57*,
        1913.

(46)   T.V. Shea, A.J. Bard *Anal. Chem.* **1987**, *59*, 524.

(47)   K.R. Wehmeyer, M.R. Deakin, R.M. Wightman *Anal. Chem.* **1985**, *57*, 1989.

(48)   M. Antonietta Baldo, S. Daniele, M. Corbetta, G.A. Mazzocchin *Electroanalysis* **1995**, *7*, 980.

(49)   D.R. MacFarlane, D.K.Y. Wong *J. Electroanal. Chem.* **1985**, *185*, 197.

(50)   M. Fleischmann, S. Bandyopadyhay, S. Pons *J. Phys. Chem.* **1985**, *89*, 5537.

(51)   J.L. Ponchon, R. Cespuglio, F. Gonon, M. Jouvet, J.F. Pujol *Anal. Chem.* **1979**, *51*, 1483.

(52)   M.A. Dayton, J.C. Brown, K.J. Stutts, R.M. Wightman *Anal. Chem.* **1980**, *52*, 946.

(53)   J.O. Howell, R.M. Wightman *Anal. Chem.* **1984**, *56*, 524.

(54)   C.M.A. Brett, A.M.O. Brett *Electrochemistry: Principles, Methods and Applications*; Oxford University Press: Oxford, 2000, p. 74.

(55)   S.K. Chakarvarti, J. Vetter *J. Micromech. Microeng.* **1993**, *3*, 57.

(56)   T.M. Whitney, J.S. Jiang, P.C. Searson, C.L. Chien *Science* **1993**, *261*, 1316.

(57)   C.D. Merritt, B.L. Justus *Chem. Mater.* **2003**, *15*, 2520.

(58)   V.P. Menon, C.R. Martin *J. Mater. Chem.* **1997**, *7*, 1075.

(59)   C.R. Martin *Science* **1994**, *266*, 1961.

(60)   R. Feeney, S.P. Kounaves *Electroanalysis* **2000**, *12*, 677.

(61)   I. Kleps, A. Angelescu *Biomed. Microdev.* **2001**, *3*, 29.

(62)   A. Stett, U. Egert, E. Guenther, F. Hoffman, T. Meyer, W. Nisch, H. Hammerle *Anal. Bioanal. Chem.* **2003**, *377*, 486.

(63)   J. Kwak, A.J. Bard *Anal. Chem.* **1989**, *61*, 1794.

(64)   R.C. Engstrom, M.Weber, D.J. Wunder, R. Burgess, S. Winquist *Anal. Chem.* **1986**, *58*, 844.

(65)   H. Sugimura, N. Shimo, N. Kitamura, H. Masuhara *J. Electroanal. Chem.* **1993**, *346*, 147.

(66)   S.B. Basame, H.S. White *J. Phys. Chem.* **1995**, *99*, 16430.

(67)   A.J. Bard, F.Fan, J. Kwak, O. Lev *Anal. Chem.* **1989**, *61*, 132.

(68)   J. Kwak, A.J. Bard *Anal. Chem.* **1989**, *61*, 1221.

(69)   J.L. Fernández, A.J. Bard *Anal. Chem.* **2004**, *76*, 2281.

(70)   C. Demaille, P.R. Unwin, A.J. Bard *J. Phys. Chem.* **1996**, *100*, 14137.

(71)   S. Bollo, L. Núñez-Vergara, J.A. Squella *J. Electroanal. Chem.* **2004**, *151*, E322.

(72)   R.C. Engstrom, B. Small, L. Kattan *Anal. Chem.* **1992**, *64*, 241.

(73)   S.B. Basame, H.S. White *J. Phys. Chem. B* **1998**, *102*, 9812.

(74)   R.D. Martin, P.R. Unwin *Anal. Chem.* **1998**, *70*, 276.

(75)   S. Cannan, J. Zhang, F. Grunfeld, P.R. Unwin *Langmuir* **2004**, *20*, 701.

(76)   B. Liu, S.A. Rotenberg, M.V. Mirkin *Proc. Nat. Acad. Sci. USA* **2000**, *97*, 9855.

(77)   C. Lee, J. Kwak, A.J. Bard *Proc. Nat. Acad. Sci. USA* **1990**, *87*, 1740.

(78)   S. Fonseca, A.L. Barker, S. Ahmed, T.J. Kemp, P.R. Unwin *Phys. Chem. Chem. Phys.* **2004**, *6*, 5218.

(79)   C. Amatore, F. Bonhomme, J.-L. Bruneel, L. Servant, L. Thouin *J. Electroanal. Chem.* **2000**, *484*, 1.

(80)   N.J. Gray, P.R. Unwin *Analyst* **2000**, *125*, 889.

(81)   M. Mirkin, F. Fan, A.J. Bard *J. Electroanal. Chem.* **1992**, *328*, 47.

(82)   B.B. Kateman, W. Schuhmann *Electroanalysis* **2002**, *14*, 22.

(83)   Y. Shao, M.V. Mirkin, G. Fish, S. Kokotov, D. Palanker, A. Lewis *Anal. Chem.* **1997**, *69*, 1627.

(84)   J. Gorelik, Y.J. Zhang, A.I. Shevchuk, G.I. Frolenkov, D. Sanchez, M.J. Lab, I. Vodyanoy, C.R.W. Edwards, D. Klenerman, Y.E. Korchev *Mol Cell Endocrinol* **2004**, *217*, 101-108.

(85)   Y.E. Korchev, J.Gorelik, M.J. Lab, E.V. Sviderskaya, C.L. Johnston, C.R. Coombes, I. Vodyanoy, C.R.W. Edwards *Biophys J* **2000**, *78*, 451-457.

(86)   A.I. Shevchuk, J. Gorelik, S.E. Harding, M.J. Lab, D. Klenerman, Y.E. Korchev *Biophys J* **2001**, *81*, 1759-1764.

(87)   R.J. Taylor, A.A. Humffry *J. Electroanal. Chem.* **1973**, *42*, 321.

(88)   Q. Chen, G.M. Swain *Langmuir* **1998**, *14*, 7017.

(89)   N. Sinkaset, A.M. Nishimura, J.A. Pihl, W.C. Trogler *J. Phys. Chem. A* **1999**, *103*, 10461.

(90)   P. Chen, R.L. McCreery, *Anal. Chem.* **2006**, *68*, 3958.

(91)   P.L. Runnels, J.D. Joseph, M.J. Logman, R.M. Wightman *Anal. Chem.* **1996**, *71*, 2782.

(92)   T.M. Day, P.R. Unwin, J.V. Macpherson *Nano Lett.* **2007**, *7*, 51.

(93)   J.M. Nugent, K.S.V. Santhanam, A. Rubio, P.M. Ajayan *Nano Lett.* **2001**, *1*, 87.

(94)   H. Dai, J. Kong, C. Zhou, N. Franklin, T. Tombler, A. Cassell, S. Fan, M. Chapline *J. Phys. Chem. B* **1999**, *103*, 11246.

(95)   Y. Yao, K-K Shiu *Anal. Bioanal. Chem.* **2007**, *387*, 303.

(96)   J.J. Gooding, A. Chou, J. Liu, D. Losic, J.G. Shapter, D.B. Hibbert *Electrochem. Comm.* **2007**, *9*, 1677.

(97)   E. Katz, I. Willner *ChemPhysChem* **2004**, *5*, 1084.

(98)   P.G. Whitten, A.A. Gestos, G.M. Spinks, K.J. Gilmore, G.G. Wallace *J. Biomed. Mater. Res Part B: Appl. Biomater.* **2006**, *82B*, 37.

(99)   S. Liu, C. Cai *J. Electroanal. Chem.* **2007**, *602*, 103.

(100)   Y. Zhang, Y. Pan, S. Su, L. Zhang, S. Li, M. Shao *Electroanalysis* **2007**, *19*, 1695.

(101)   N.R. Wilson, S.L. Clewes, M. E. Newton, P.R.Unwin, J.V. Macpherson *J. Phys. Chem. B* **2006**, *110*, 5639.

(102)   B.V. Sarada, T.N. Rao, D.A. Tryk, A. Fujishima *Anal. Chem.* **2000**, *72*, 1632.

(103)   K.B. Holt, A.J. Bard, Y. Show, G.M. Swain *J. Phys. Chem. B* **2004**, *108*, 15117.

(104)   G.W. Muna, N. Tasheva, G.M. Swain *Environ. Sci. Technol.* **2004**, *38*, 3674.

(105)   R.G. Compton, J.S. Foord, F. Marken *Electroanalysis* **2003**, *15*, 1349.

(106)   E. Brillas, B. Boye, I. Sires, J.A. Garrido, R.M. Rodriguez, C. Arias, P.L. Cabot, C. Comninellis *Electrochim. Acta* **2004**, *49*, 4487.

(107)   A.T. Collins in *Properties and Growth of Diamond*; Davies, G., Ed.; Institute of Electrical Engineers: London, 1884.

(108)   J.P. Legrange, A. Deneuville, E. Gheeraert *Carbon* **1999**, *37*, 807.

(109)   Y. V. Pleskov *Russ. J. Electrochem.* **2002**, *38*, 1275.

(110)   K. Nishimura, K. Das, J.T. Glass *J. Appl. Phys.* **1991**, *69*, 3142.

(111)   M. Werner, R. Job, A. Zaitzev, W.R. Fahrner, W. Seifert, C. Johnston, P.R. Chalker *Phys. Status Solidi A* **1996**, *154*, 385.

(112)   M.C. Granger, M. Witek, J.S. Xu, J. Wang, M. Hupert, A. Hanks, M.D. Koppang, J.E. Butler, G. Lucazeau, M. Mermoux, J.W. Strojek, G.M. Swain *Anal. Chem.* **2000**, *72*, 3793.

(113)   D.A. Tryk, K. Tsunozaki, T.N. Rao, A. Fujishima *Diamond Relat. Mater.* **2001**, *10*, 1804.

(114)   M.C. Granger, G.M. Swain *J. Electrochem. Soc.* **1999**, *146*, 4551.

(115)   E. Mahé, D. Devilliers, Ch. Comininellis *Electrochim. Acta* **2005**, *50*, 2263.

(116)   J.A. Bennett, J. A. W., Y. Show, G.M. Swain *J. Electrochem. Soc.* **2004**, *151*, E306.

(117)   H. Chang, A.J. Bard *Langmuir* **1991**, *7*, 1143.

(118)   R.J. Rice, R.L. McCreery *Anal. Chem.* **1989**, *61*, 1637.

(119)   R.J. Bowling, R.L. McCreery, C.M. Pharr, R.C. Engstrom *Anal. Chem.* **1989**, *61*, 2763.

(120)   D.H. Pashley, H.J. Andringa, G.D. Derkson, S.R. Kalathoor *Archs. Oral Biol.* **1987**, *32*, 519.

(121)   N.J. Mordan, P.M. Barber, D.G. Gillam *J. Oral Rehab.* **1997**, *24*, 148.

(122)   D.H. Pashley *J. Endodont.* **1986**, *12*, 465.

(123)   L. Breschi, P. Gobbi, G. Azzotti, M. Falconi, T.H. Ellis, I. Stangel *Dent. Mat.* **2002**, *18*, 26.

(124)   L.P Gartner, J.L. Hiatt in *Color Atlas of Histology,* 4th ed.; Lippincott Williams & Wilkins: Baltimore, MA, USA, 2006, pp 260.

(125)   D.Scott, T.R.Tempel *J. Dent. Res.* **1965**, *44*, 20.

(126)   M. Brännström *Archs. Oral Biol.* **1962**, *7*, 59.

(127)   D.J. Anderson, M.P. Curwen, L.V. Howard *J Dent. Res.* **1958**, *37*, 669.

(128)   M. Brännström, A. Åström *J Dent. Res.* **1964**, *43*, 619.

(129)   M.R. Byers *Archs. Oral Biol.* **1994**, *39 (S)*, S13.

(130)   N. Vongsavan, B. Matthews *Archs. Oral Biol.* **1992**, *37*, 175.

(131)   I.A. Mjör, I. Nordahl *Archs. Oral Biol.* **1996**, *41*, 401.

(132)   B. Ciucchi, S. Bouillaguet, J. Holz, D. Pashley *J. Endodont.* **1995**, *21*, 191.

(133)   J. Camps, V. Santin, R. Rieu, J. Fuseri, J.C. Franquin *Archs. Oral Biol.* **1996**, *41*, 837.

(134)   O.W. Reeder, R.E. Walton, M.J. Livingston, D.H. Pashley *J. Dent. Res.* **1978**, *57*, 187.

(135)   E.R. Van der Graaf, J.J. Ten Bosch *Archs. Oral Biol.* **1988**, *33*, 375.

(136)   A.R. Özok, M.-K. Wu, P.R. Wesselink *J. Dent.* **2002**, *30*, 107.

(137)   W.C. Outhwaite, D.M. McKenzie, D.H. Pashley *J. Dent. Res.* **1974**, *53*, 1503.

(138)   D.H. Pashley, W.G. Matthews, Y. Zhang, M. Johnson *Archs. Oral Biol.* **1996**, *41*, 1065.

(139)   D.H. Pashley, W.G. Matthews *Archs. Oral Biol.* **1993**, *38*, 577.

(140)   N. Vongsavan, B. Matthews *Archs. Oral Biol.* **1991**, *36*, 641.

(141)   D.H. Pashley, R. Nelson, E.L. Pashley *Archs. Oral Biol.* **1981**, *26*, 707.

(142)   H. Griffiths, G. Morgan, K. Williams, M. Addy *J. Periodont. Res.* **1993**, *28*, 60.

(143)   F. Greenwood, H. Horiuchi, B. Matthews *Archs. Oral Biol.* **1972**, *17*, 701.

(144) E.R. Scott, H.S. White, J.B. Phipps *Anal. Chem.* **1993**, *65*, 1537.

(145) J.V. Macpherson, D. O'Hare, P.R. Unwin, C.P. Winlove *Biophys. J.* **1997**, *73*, 2771.

(146) S. Nugues, G. Denuault *J. Electroanal. Chem.* **1996**, *408*, 125.

(147) J.V. Macpherson, M.A Beeston, P.R. Unwin, N.P. Hughes, D. Littlewood *J. Chem. Soc., Faraday Trans.* **1995**, *91*, 1407.

(148) J.V. Macpherson, M.A. Beeston, P.R. Unwin, N.P. Hughes *Langmuir* **1995**, *11*, 3959.

(149) A.M. Cherng, L.C. Chow, S. Takagi *Archs. Oral Biol.* **2004**, *49*, 91.

(150) D.H. Pashley, J.G. Leibach, J.A. Hornert *J. Periodont.* **1987**, *58*, 19.

(151) K. Markowitz, K. Bilotto, M.-T. Lui, Y.-T. Jou, S. Kim *Archs. Oral Biol.* **1991**, *36*, 1.

(152) K. Markowitz, S. Kim *Proc. Finn. Dent. Soc.* **1992**, *88*, (supp 1) 39.

(153) M. Kagayama, Y. Sasano, H. Sato, S. Kamakura, K. Motegi, I. Mizoguchi *Anat. Embryol.* **1999**, *199*, 233.

(154) N. Silikas, D.C. Watts, K.E.R. England, K.D. Jandt *J. Dent.* **1999**, *27*, 137.

(155) M. Yoshiyama, Y. N., K. Ozaki, A. Uchida, Y. Ishikawa, H. Ishida *J. Dent. Res.* **1990**, *69*, 1293.

(156) H.F. Thomas, R.C. Payne *J. Dent. Res.* **1983**, *62*, 532.

(157) R. Schilke, J.A. Lisson, O. Bauß, W. Geurtsen *Archs. Oral Biol.* **2000**, *45*, 355.

Chapter 2

Experimental

This section details the instrumentation, methodologies, reagents and apparatus used in the experiments described within this thesis.

2.1 Preparation of Tooth Surfaces

The experiments detailed within this thesis largely centred on dentine and enamel tooth surfaces. Preparation of these surfaces is detailed here.

2.1.1 Dentine Sample Preparation

In vitro experiments traditionally employ dentine discs as a substrate. They are convenient to use because of their uniform thickness and their capacity for smoothness. Occlusal discs are normally used, although root discs have also been studied. Occlusal discs are cut parallel to the occlusal plane, the imaginary surface on which upper and lower teeth meet in the crown of the tooth. These discs have higher permeability over pulp horns and lower permeability in the centre, due to the greater density of tubules over the pulp horns.[122] Figure 2.01 shows the location from which these discs are taken.
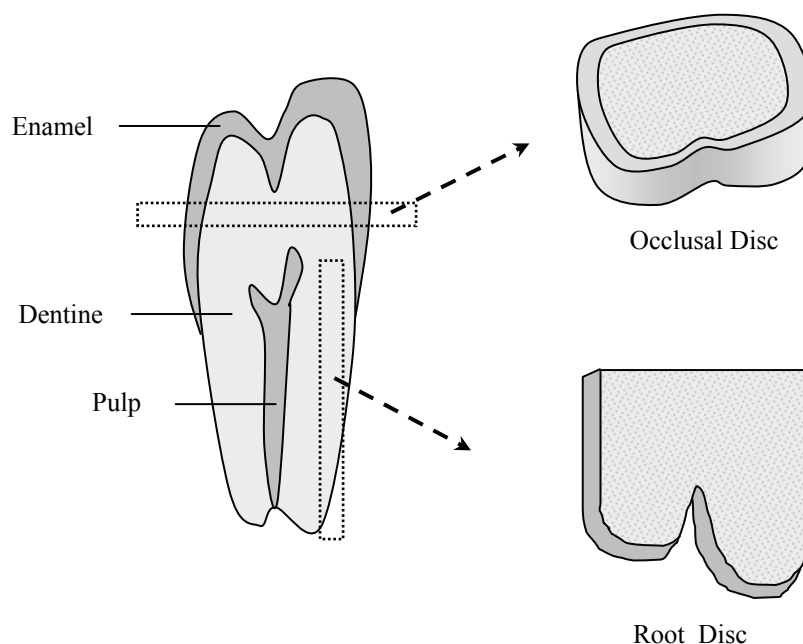
Figure 2.01: Schematic displaying the location from which the occlusal and root discs are taken (Adapted from reference 2).

The applicability of the dentine disc as a model for *in vitro* studies of dentinal hypersensitivity has been reviewed.[123] The conclusion was made that the dentine disc is a reliable model, provided a precise control procedure is applied. The procedure involved using two adjacent areas of the same dentine disc, one as a test surface, and the other as a control. This direct comparison between two neighbouring regions allowed for the natural variation in tubule morphology across the dentine disc, and also for the diverse effect of etching.

Dentine slices *ca*. $100 - 150$ μm in thickness were used in all experiments (except for the pressure transient experiments described in Chapter 3). For a number of experiments, these were taken from a coronal section of the outer third of dentine from human third molars, supplied by ABSBio, USA with informed patient consent and in accordance with current human tissue acquisition legislation. In the remaining experiments, the slices were taken from the buccal

face of bovine incisors. The teeth were sterilised in 20,000 ppm sodium hypochlorite prior to sectioning. The slices were polished on 600 grit Carbimet polishing paper (Buehler, Coventry, UK), followed by 4000 grit silicon carbide paper (Buehler), to remove ridges inherent to the cutting process. The organic smear layer[124] was removed by etching the dentine in 10% citric acid (Aldrich, UK) for 8-10 minutes and then thoroughly rinsing in Milli-Q reagent water. The smear layer is an adherent layer of debris produced during toothbrushing or cutting during dental procedures. It covers the surface of the dentine, thus occluding exposed tubules and reducing permeability. Smear plugs are small masses of this debris that form within the tubules. It has been shown that maleic acid and citric acid both remove the smear layer and partially remove smear plugs.[125] For SECM and LSCM experiments, once prepared, each dentine disc was sealed flush on the end of a glass capillary (4.0 mm o.d., Harvard Apparatus, Kent, UK) using a superglue/nail varnish mixture (Bostik, UK). The dentine thus served as the membrane separating a donor from a receptor solution for SECM and LSCM measurements, as described in section 2.1.2.

2.1.2   Setup for SECM and LSCM Studies on Dentine

The experimental setups for the SECM and LSCM studies on dentine were largely the same. Experiments were carried out in a cell comprising of a PTFE base and glass cell body. The glass capillary was secured through a hole in the bottom of the cell and sealed in with wax to avoid leakage of solution. A photograph of the experimental setup for SECM is shown in Figure 2.02.
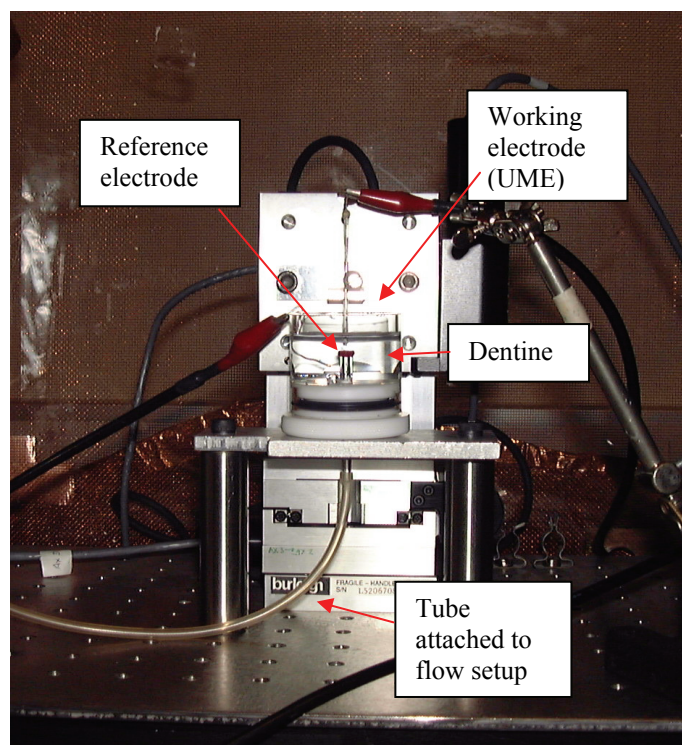
Figure 2.02: Photograph showing the SECM experimental set-up.

For SECM studies, the capillary and the cell were both filled with the redox mediator solution that was being studied. For LSCM studies, the capillary was filled with a solution containing 10 μM Rhodamine B (Fluka) and 1 mM $CaCl_2$ (Sigma-Aldrich) in 20 mM HEPES buffer (Fluka) and the cell was filled with a solution containing 1 mM $CaCl_2$ in 20 mM HEPES buffer. In both instances it was necessary to induce flow of solution from the capillary through the dentine into the cell. This was effected in one of two ways. In the first method, the glass capillary was connected to a 100 ml syringe pump (KD Scientific, Holliston, MA), containing the same solution as the capillary, via silicone rubber tubing. The second method utilised a gravity feed system. This was only used for SECM studies. A reservoir of the redox mediator was connected to the glass capillary, again using silicone tubing. The reservoir was held at a fixed height above the

dentine sample in order to determine the applied pressure; for example 24 cm corresponds to a pressure of 2.4 kPa. In both cases, fluid flow led to the development of trans-dentine pressure which encompassed that measured *in-vivo* and led to higher pressures to provide a challenge to the various treatments considered. Pressure-time data were measured simultaneously via a digital differential pressure sensor, built in-house.

2.1.3   Enamel Preparation

Sections of enamel from bovine incisors were polished sequentially with 600 and 4000 grit polishing papers, as described for the dentine samples. To further remove scratches from the enamel surface the samples were then polished in alumina slurry (0.05 μm). For dissolution experiments, the enamel was attached to a PTFE base using double-sided tape.

2.2   Ultramicroelectrode (UME) Fabrication

A borosilicate glass capillary (2.0 mm o.d., 1.16 mm i.d., Harvard Apparatus, Kent) was pulled to a fine point using a pipette puller (model PB-7, Narishige Co. Ltd, Japan). The fine point was sealed in a Bunsen burner flame, and the open end flame-polished until smooth. A 1 cm length of 25 μm diameter Pt wire (Goodfellow Ltd, Cambridge, UK) was placed in the capillary, which was tapped gently to ensure that the wire sat in the sealed end of the capillary. The sealed capillary was then placed in a holder and the tip held in the centre of a nichrome wire heater coil. The capillary was held under vacuum for 20 minutes. The tip of the capillary was then heated, under vacuum, to seal the wire and glass. A solid-core tinned-copper connecting wire was attached to the Pt wire using a small

amount of silver epoxy (RS, UK), and the connecting wire stabilised using Araldite (Bostik, UK). The platinum wire was exposed using 240 grit Carbimet polishing paper (Buehler, Coventry, UK). The connection was tested by running cyclic voltammetry in a solution comprising 5 mM potassium ferrocyanide, $K_4Fe(CN)_6$ (Aldrich, UK), and 0.1 M potassium nitrate, KNO_3 (Aldrich, UK).

For SECM experiments, it was essential that the tip was polished flat, and had the correct RG value, i.e. RG = 10, as described in section 1.4.1. To achieve this, the tip was first 'coned' using 600 grit Carbimet polishing paper (Buehler, Coventry, UK). This involved polishing the electrode tip by hand until the total diameter of the tip was ten times the diameter of the Pt wire. The optical microscope was used regularly to check the diameter. Once the tip was of the required RG value, a brace was used to flatten the tip as much as possible. This brace, consisting of a holder and a precision engineered metal block, ensured that the electrode was held perpendicular to the polishing paper, thus guaranteeing a flat surface. To ensure a completely flat electrode had been produced, the electrode was placed on a polishing wheel (grit 0.1 μm, Buehler, Coventry, UK) for a few seconds. Finally, 0.05 μm alumina on a polishing cloth (Buehler, Coventry, UK) was used to give a fine finish. Dimensions of the finished UME were determined using an optical microscope (Olympus BH2). A typical UME is shown in Figure 2.03. Electrochemical characterisation of the UME is described in Chapter 3.3.
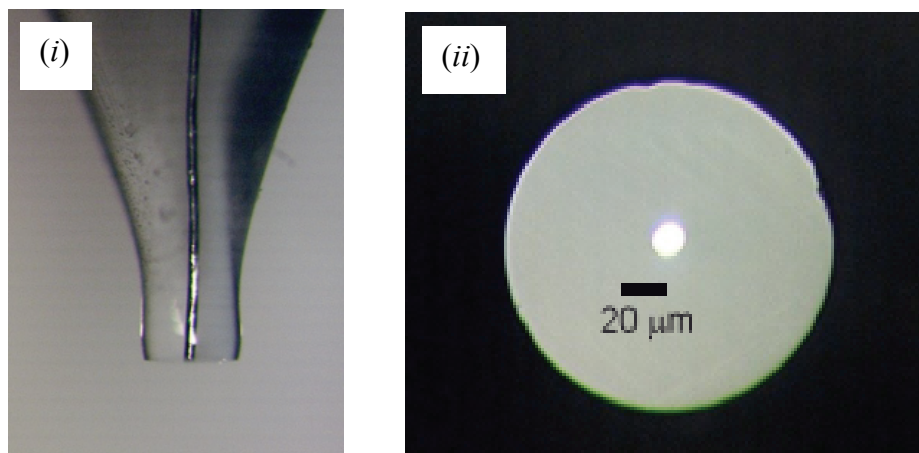
Figure 2.03: Images obtained using optical microscopy showing (*i*) a side view of a 10 µm

diameter Pt UME, and (*ii*) an end-on view of the same Pt UME.

2.3   Instrumentation

A large variety of instrumentation was employed in the studies described herein.

Here, the general equipment used for each technique is introduced.

2.3.1   Cyclic Voltammetry (CV)

Stand-alone cyclic voltammetry (CV) experiments, such as those described in

Chapter 3.4, were carried out using a CH Instruments bipotentiostat, model

730A. Unless otherwise stated, CV measurements were made using a 25 µm

diameter Pt UME in a two-electrode setup vs a Ag/AgCl reference electrode. CV

experiments carried out in conjunction with SECM and SICM studies utilised

software written in-house, with the tip potential applied from a wave generator or

directly from the PC, respectively.

2.3.2 SECM

SECM experiments on dentine were carried out using the cell setup described in section 2.1.2. (Details of SECM measurements made on BDD are found in Chapter 6.) The position of the UME tip with respect to the substrate was controlled by three TSE-75 stages (Burleigh Instruments, NJ, USA) in an x,y,z configuration. These were linked to a 6200-3-3 controller unit, interfaced to a PC by a Burleigh 660 interface card. The stages were mounted on a vibrationally-isolated bench and the entire experimental setup shielded with a Faraday cage, built in-house.

2.3.3 AFM

A Nanoscope E AFM was used to image the dentine and enamel surfaces (Chapters 3 and 5 respectively). The instrument was enclosed in a Faraday cage, manufactured in-house, and this was in turn placed on a granite bench incorporating vibration isolators. All images were obtained in contact mode. Silicon nitride probes (Digital Instruments), comprising 200 μm cantilevers with integrated pyramidal tips, were employed for image acquisition. Details of AFM studies on BDD are detailed in Chapter 6.

2.3.4 FE-SEM

In order to obtain images of dentine, the samples were mounted on aluminium stubs using carbon adhesive discs (Agar Scientific, UK). The specimens were sputter-coated with a thin layer of gold. Imaging was carried out using a Zeiss Supra 55VP FE-SEM.

Micropipette tips used in SICM and SMCM experiments (Chapters 4 and 6 respectively) were imaged in a similar manner. The tips were secured to the stubs using carbon discs and an additional coating of silver dag (Agar Scientific, UK) before being coated with gold. This was necessary to secure the micropipettes sufficiently so they could be tilted in the FE-SEM and the dimensions of the tip openings determined.

BDD, described in Chapter 6, is a (semi)conducting material and thus it was unnecessary to coat the sample in gold prior to imaging.

2.3.5   LSCM

For fluid flow studies on dentine (Chapter 4), the cell setup, as described in section 2.1.2, was placed on the stage of a Zeiss LSM 510, Axioplan 2, confocal microscope. The glass stage plate and condenser of the microscope were removed to allow positioning of the dentine substrate attached to the glass capillary. Flow was achieved using a syringe pump. A schematic of the LSCM set-up for flow experiments is shown in Figure 2.04.
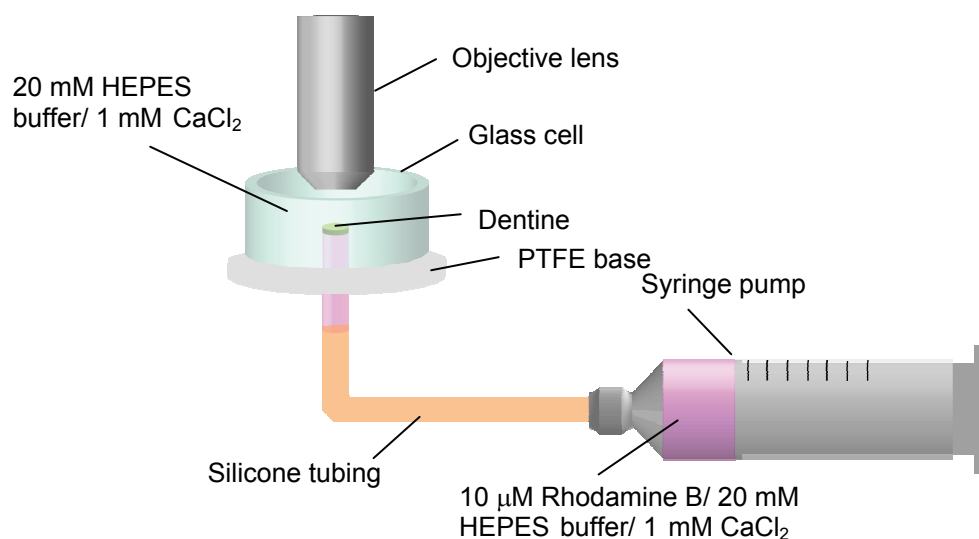
Figure 2.04: Schematic showing the experimental set-up for all LSCM fluid flow experiments.

For all studies on dentine, a helium/neon laser (λ = 543 nm) was used to induce fluorescence and a long pass filter (λ = 560 nm) employed to collect the emitted light. For images obtained in solution, a water immersion objective lens (Zeiss, Achroplan 20× / 0.50W) with a 10 × tube lens was used, whereas for images recorded in air, a Zeiss Epiplan Neofluar 20 ×/ 0.50 lens was employed. Experimental details for combined electrochemical/LSCM experiments on BDD are given in Chapter 6.

2.3.6 SICM

Micropipettes were pulled from sodium borosilicate capillaries (Either 1.2 μm O.D., 0.69 μm I.D., or 1.0 μm O.D., 0.58 μm I.D., Harvard Apparatus, Kent) using a laser puller (Model P-2000, Sutter Instrument Co, Intracel, Hertfordshire). The exact tip diameter was determined using an optical microscope (Olympus BH2) before carrying out SICM experiments. The

substrate was secured to a glass microscope slide using Gel-Pak 8 (Gel-Pak, Hayward, CA) and a glass cylinder of suitable diameter glued to the slide to form a reservoir. This was then secured to the stage of the microscope and the reservoir filled with 0.1 M NaCl solution. The micropipette was also filled with the NaCl solution. A Ag/AgCl electrode (diameter ~ 200 μm) was introduced into the micropipette, as far as the widest part of the tip. A second Ag/AgCl electrode (diameter ~ 1mm) was placed in the solution contained within the reservoir. A potential was applied between the two electrodes, via a PCI-6731 DAQ (National Instruments, Austin, TX). The ion current that flowed through the tip of the micropipette, with a magnitude dependent on the position of the micropipette relative to the sample, was converted to a voltage via a current follower, built in-house. This voltage was recorded by a BNC-2110 DAQ (National Instruments), which was in turn controlled by software developed in-house using Labview (v. 7.1, National Instruments). The micropipette was attached to a P-611.3S NanoCube piezo positioner (Physik Instruments, Germany) that allowed movement relative to the sample interface (z direction) and in the x and y axes with a resolution of 2 nm (closed loop). The NanoCube was controlled with an E-664 LVPZT amplifier/servo. This was interfaced to the PC. The whole set-up was mounted on an inverted microscope (Zeiss Axiovert 25) to aid positioning of the tip relative to the sample. Initial tip positioning was achieved using a micrometer-controlled x,y,z positioner (461 series, Newport, NJ).

2.4   Materials

All solutions were prepared using Milli-Q water (Resistivity ≥18 MΩ). The mass of solid materials was measured on a four-figure analytical balance (Sartorius A2008). All pH measurements were made using an UltraBasic pH meter (Denver Instruments). The grades and suppliers of all the chemicals used are listed in Table 2.01. The composition of each solution used will be detailed in subsequent chapters.

CHEMICAL	GRADE	SUPPLIER
Acetone	>99%	Fisher
Isopropanol (IPA)	HPLC grade	Fisher
Potassium Nitrate (KNO_3)	>99.5%	Fisher
Potassium Chloride (KCl)	A.R.	Fisher
Sodium Chloride (NaCl)	A.R.	Fisher
Potassium hexacyanoferrate (II) ($K_4Fe(CN)_6$)	A.R.	Fisher
Hexaammineruthenium chloride (III) ($Ru(NH_3)_6Cl_3$)	99%	Strem Chemicals
Potassium hexachloroiridate (II) (K_3IrCl_6)	99%	Sigma Aldrich
Ferrocenemethanol (FcMeOH)	97%	Aldrich
p-benzoquinone	98%	Aldrich
Fluorescein	-	Aldrich
Rhodamine B	-	Fluka
Citric Acid	99.5%	Aldrich
Calcium Chloride ($CaCl_2$)	99%	Sigma

HEPES	-	Fluka
Sodium Alginate	Manucol	ISP

Table 2.01: Grades and suppliers of all chemicals used in the studies described within this thesis.

2.5   References

(1)   D.H. Pashley, H.J. Andringa, G.D. Derkson, S.R. Kalathoor *Archs. Oral Biol.* **1987**, *32*, 519.

(2)   N.J. Mordan, P.M. Barber, D.G. Gillam *J. Oral Rehab.* **1997**, *24*, 148.

(3)   D.H. Pashley *J. Endodont.* **1986**, *12*, 465.

(4)   L. Breschi, P. Gobbi, G. Azzotti, M. Falconi, T.H. Ellis, I. Stangel *Dent. Mat.* **2002**, *18*, 26.

Chapter 3

SECM & SICM Studies of Fluid Flow through Human and Bovine Dentine, and the Effect of Occlusion Actives on this Flow

This chapter describes the use of scanning electrochemical microscopy (SECM), combined with *in situ* pressure-time measurements, to investigate the flow of fluid through human and bovine dentine, and the subsequent effect of occlusion treatments on this flow. Scanning Ion Conductance Microscopy (SICM) is also introduced as a technique for imaging dentine, with instrument design and development described, and also calibration of the technique.

3.1   Introduction

Dentinal hypersensitivity is a prevalent condition affecting a large proportion of the adult population. A number of theories have been proposed to explain the origins of the problem.[1] One of these, the dentinal receptor theory, postulates that the odontoblasts and the finger-like processes that extend from them, act as dentinal receptors. Odontoblasts are the cells responsible for the maintenance and repair of dentine.[2] The processes from these cells penetrate the tubules to varying extents. The theory proposes that nerves within these processes may elicit the pain response, rather than nerves within the pulp itself. Electrical activity from dental nerve fibres has been recorded;[3] however it is possible that the activity resulted from pulp nerves. Some studies have involved the application of pain-inducing substances to dentine.[4] These failed to elicit pain and so suggested that

the odontoblasts within the dentine are not involved in the pain response.[5] Additionally, dentine remained sensitive even after disruption of the odontoblast cells.[6] A second hypothesis suggests that the nerves in the pulp are the pain receptors, and that nerve impulses are controlled by the secretion of particular polypeptides during injury of the pulp.[7] The most widely accepted hypothesis is the hydrodynamic theory, as introduced briefly in section 1.1.2. This theory was introduced by Gysi in 1900[8] with supporting evidence produced in the 1950's and 1960's.[9] The premise of this theory revolves around the fact that once dentine is exposed, either by enamel erosion or gingival recession, fluid flows from the pulp to the buccal cavity (the mouth). This fluid flow arises because the dentine is subject to a positive pressure of *ca*. 1.47 kPa. A resting flow rate of 18.1 pl s^{-1} mm^{-2} has been estimated.[10] After the application of a stimulus (e.g. heat or coldness) that causes a change in the pressure of the buccal cavity, there is a rapid shift in the fluid flow. This shift may occur in either direction. The result is activation of sensory nerves in the pulp, and thus pain is felt by the sufferer. Consequently, a better understanding of this mechanism requires the investigation of fluid movement through dentine. A schematic demonstrating the premise of the theory is shown in Figure 3.01.
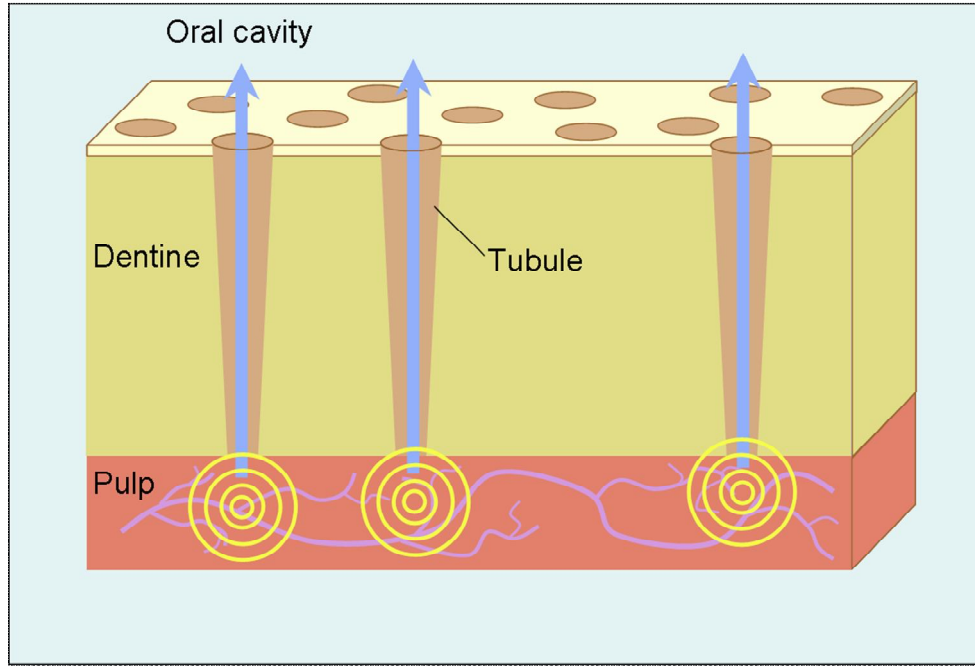
Figure 3.01: Schematic to demonstrate the hydrodynamic theory of dentinal hypersensitivity

The established methods of determining fluid flow, as described below, measure only the net permeability of the sample. However, as previous studies show,[11, 12] the arrangement of tubules in dentine is such that permeability is not uniform across a sample. Also, subsurface blocking can cause heterogeneities.

The best established method for bulk quantitative studies of dentine permeability is the measurement of hydraulic conductance.[13, 14] Reeder *et al* [15] proposed a theoretical model for the hydraulic conductance of dentine. This measurement describes the ease with which fluid flows through dentinal tubules. Hydraulic conductance, L_p, may be defined as follows:

$$L_p = \frac{J}{\Delta PA} \tag{3.01}$$

where J is the water flux (m^3 s^{-1}), ΔP is the applied fluid pressure gradient (Nm^{-2}), and A (m^2) is the surface area of the disc. Other equations may be derived by taking into account the non-linear morphology of dentinal tubules.[16]

The permeability of occlusal and root dentine discs has been compared using the hydraulic conductance method.[17] Discs taken from these regions were seen to have similar permeabilities *in vitro*. The system used is shown schematically in Figure 3.02.
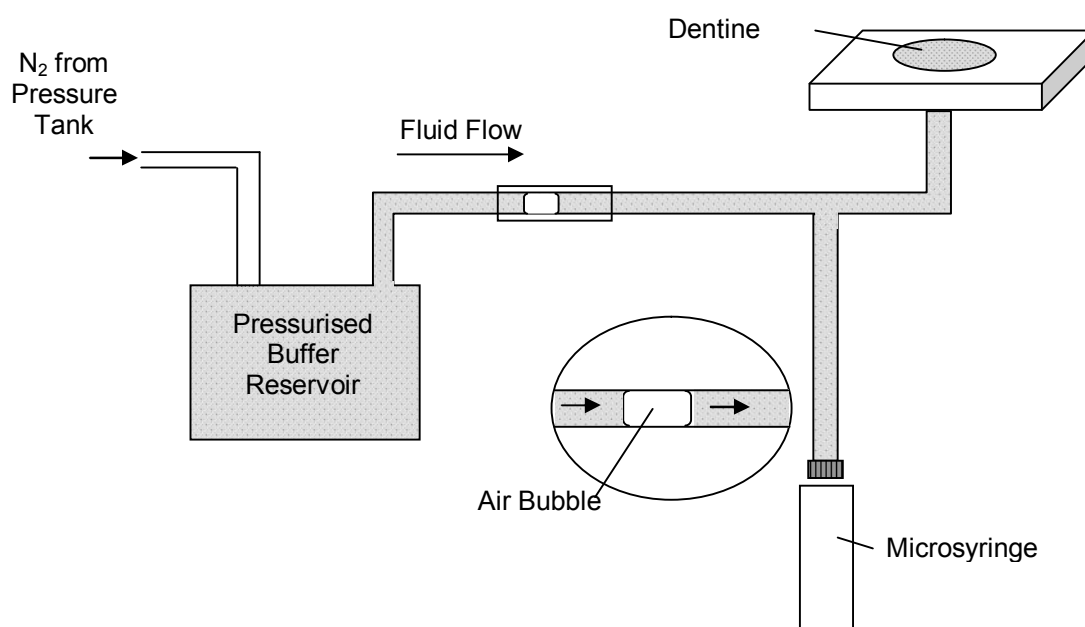
Figure 3.02: Schematic showing the set-up used for hydraulic conductance measurements.

Fluid was forced from the pulpal side of dentine to the surface, and the rate of fluid movement was studied by measuring the progress of an air bubble in a micropipette and converting this distance to a volume of fluid. The dentine disc was held in a split chamber device.[18] The effect of various hydrodynamic stimuli on fluid shifts across human dentine has been elucidated.[19] Fluid flow was

studied using a device which again measured the linear displacement of an air bubble over time, and hydraulic conductance was calculated. The ranking of the effect of stimuli on fluid flow was found to be hot>cold>air blast>osmotic>tactile. [19]

A number of reports have been published which describe various methods of investigating bulk fluid flow through dentine. These include studies on the inward diffusion of radioactive iodide in human dentine,[20] and investigations of the uptake of Evans' blue dye solution by feline dentine.[21, 22] These latter studies concluded that there is sufficient outward fluid flow *in vivo* to reduce the inward diffusion of chemicals such as Evans' blue into the tubules. This has implications for dentinal hypersensitivity treatments which contain K^+, as K^+ is thought to diffuse down concentration gradients in the dentine tubules to the pulp. This may raise the extracellular potassium concentration sufficiently to inactivate the nerve cells, as described in section 1.1.3. Bacteria may also play a role in exacerbating dentinal hypersensitivity, but this role is not clearly understood.[23] Again, any diffusion of toxins to the pulp would be opposed by the outward fluid flow.[1]

As an alternative method to the flow studies, streaming potentials across dentine have been measured *in vitro*.[24] Streaming potentials are electrical potentials created when fluid flows through a porous structure, and should be proportional to pressure. These potentials were measured using silver electrodes over a pressure range of 1-6 atmospheres. It was found that at low pressures, excitation of pulpal nerves did not occur, as discovered in previous studies,[25] and thus no pain was felt. However, stimuli applied to dentine that evoke painful responses

may cause a great increase in pressure, maybe hundreds of atmospheres, and therefore large enough streaming potentials would be created and would be able to stimulate the nerves.

Importantly, all of the studies described above involved bulk measurement of fluid flow over the whole surface, therefore gross assumptions had to be made, such as: the surface is uniformly flow active; the tubules have the same diameter; and all tubules are open.

Scanning electrochemical microscopy (SECM) has been shown to be a powerful tool for imaging topography, interfacial reactivity, and also local transport processes across interfaces. The technique has been used to image local diffusion and migration processes, in particular across skin,[26] cartilage,[27] and polycarbonate membranes.[28] Unwin and co-workers have shown in previous reports[29] that SECM can be used to quantify flow through single dentinal tubules *in-vitro,* under similar pressure conditions to those found in the oral cavity. Fluid flow was achieved by the application of a hydrostatic pressure gradient across a slice (*ca* 50 μm thick) of dentine. A 2 μm electrode was used to obtain information on flow through a single tubule. A pressure of approximately 2 kPa was applied across the sample, and fluid flow was found to vary significantly across dentine. The flow solution contained a suitable mediator, potassium hexacyanoferrate (II) trihydrate (10 mM, in an aqueous solution containing potassium chloride (0.5 M) as a supporting electrolyte), which could be detected at the tip electrode.

For a tip UME of similar size to the tubules, the current data recorded at the tip UME due to diffusion controlled electrolysis of $Fe(CN)_6^{4-}$ was converted to local flow rates using equation 3.2:

$$i/i(\infty) = 0.726 \bar{U}^{-\frac{1}{3}} (b/d)^{\frac{2}{3}} (a/D)^{\frac{1}{3}} \qquad (3.02)$$

where $i/i(\infty)$ is the normalised tip current, $\bar{U}$ is the mean velocity of the solution flowing through the tubule, a is the tip radius (μm), b is the tubule diameter (μm), d is the tip-surface separation (μm) and D is the diffusion coefficient of the mediator (cm^2 s^{-1}). A flow rate of 12 pLs^{-1} through a single tubule was determined. Only one tubule was seen to be active within the 50 μm $\times$ 50 μm region scanned. This observation suggests that the mean tubule flow rate for the area studied would be much lower than the flow rate determined for the individual tubule, and would therefore be in broad agreement with previously reported values. [10, 15, 21, 22]

SECM was also employed to image the effect of blocking agents on fluid flow.[30] The blocking agent investigated was calcium oxalate, which was formed *in-situ* due to the chemical displacement reaction between potassium oxalate and soluble calcium ions (calcium chloride solution). This resulted in the formation of an insoluble layer of calcium oxalate, which acted to occlude tubules. For electrochemical visualisation and quantification, the dentine was subjected to a sequential procedure: (i) scan with no pressure applied; (ii) scan with 2 kPa of pressure applied; (iii) Blocking agent in the form of calcium chloride and

potassium oxalate solutions applied to surface, followed by scan with no pressure applied; and (iv) scan with 2 kPa of pressure applied, with blocking agent present on surface. All imaging was carried out with a 25 μm diameter Pt UME, with the tip UME maintained at a fixed height throughout. A loss of spatial resolution was seen, compared with the experiments carried out with the 2 μm diameter UME, however a larger area of the dentine was imaged giving an overall indication of the effect of the blocking agent.

The fluid flow data before application of the blocking agent was similar to that seen previously.[10, 15, 21, 22] After application of the blocking agent, the tip currents recorded under no pressure conditions were lower than those obtained without the blocking agent. This is due to the decreased distance between the tip and the surface, resulting from the formation of the oxalate layer. With the pressure on, the currents recorded at the tip UME indicated the blocking film had successfully retarded fluid flow. From the tip current decrease it was possible to estimate the thickness of the film. Further work[31] demonstrated that a glycerol monooleate-base paste could also be used to significantly lower fluid velocities trough tubules, however this treatment was not as effective as the calcium oxalate.

Other treatments for dentinal hypersensitivity have also been studied, but again using procedures which average fluid flow over the whole surface. Cherng *et al* [32] investigated the short-term effects of treating dentine discs with supersaturated calcium phosphate solutions. These solutions appeared to lead to precipitation of calcium phosphate salts on the dentine surface, occluding tubules. They found that consecutive treatments appeared to be effective in reducing the hydraulic

conductance of the dentine discs. Pashley *et al* [33] looked at the effects on dentine permeability of burnishing a dentine sample with anumber of treatments, including a NaF/Kaolin/Glycerin paste. The burnishing process itself was found to be the important factor in tubule occlusion, rather than the paste constituents. Another approach to treating dentinal hypersensitivity is to use potassium as a densensitising agent [34, 35] as detailed in section 1.1.3.

3.2   Dentine Structure

The morphology of dentine has been investigated using many different methods. Confocal microscopy has been employed to visualise dentinal tubules using alizarin red as a stain.[36] Tapping mode AFM has been used to investigate the surface morphology and roughness of human dentine after the application of various acid treatment agents.[37] It was found that tubule diameters and depths, as well as the morphology of intertubular regions, varied between samples. The roughness of the samples ranged from 244–445 nm and tubule diameters ranged from 2.85-4.08 μm. Electron microscopy has been utilised in a variety of forms. Transmission electron microscopy (TEM) has been used to characterise the general morphology of dentine and dentinal tubules.[38, 39] Scanning electron microscopy (SEM) has been employed to compare the number and diameter of tubules in human and bovine dentine.[40] It was found that there was no significant difference in the tubule diameters of human dentine and bovine dentine. Tubule density was variable in bovine dentine itself, however it was found that bovine incisor crown dentine was a suitable substitute for human dentine.

The dentine discs employed in the studies detailed in this thesis were examined using optical microscopy, FE-SEM and AFM. An optical image of dentine is shown in Figure 3.03. The dentinal tubules are visible.
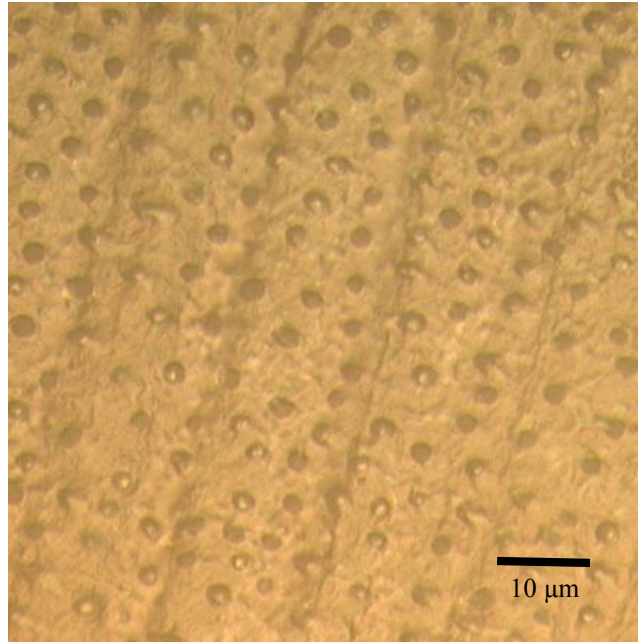
Figure 3.03: Optical image of bovine dentine showing dentinal tubules. Scale bar represents 10 μm.

AFM was utilised to elucidate tubules diameters and investigate the roughness of the sample. Figure 3.04 shows a typical AFM image recorded in contact mode. The diameters of two tubules were measured and the roughness of the sample was estimated.
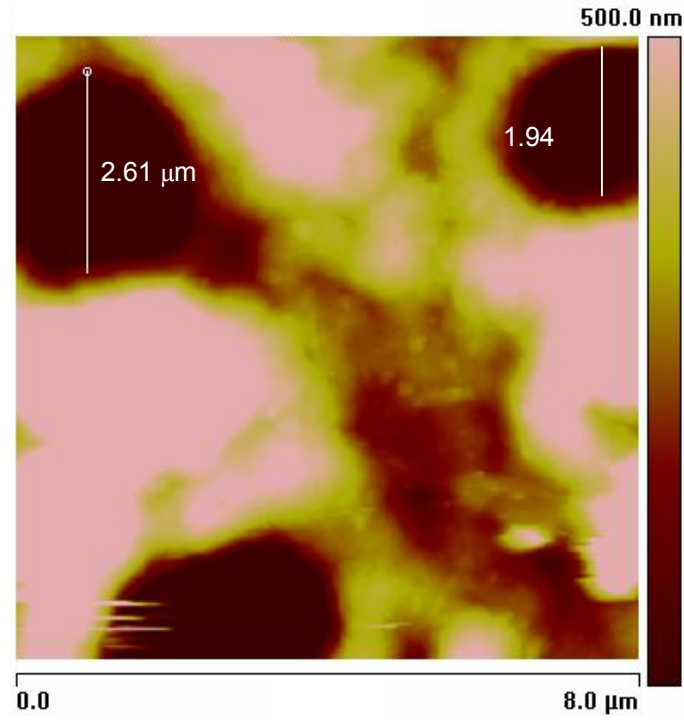
Figure 3.04: Contact-mode AFM height image showing tubule diameters of 2.61 and 1.94 μm

and surface roughness of the order of 500 nm for a bovine dentine sample.

FE-SEM is a powerful, high-resolution imaging technique[41] that was used to probe dentine morphology further. Figure 3.05 shows FE-SEM images of bovine dentine. Image (*i*) was recorded at a lower resolution than (*ii*).
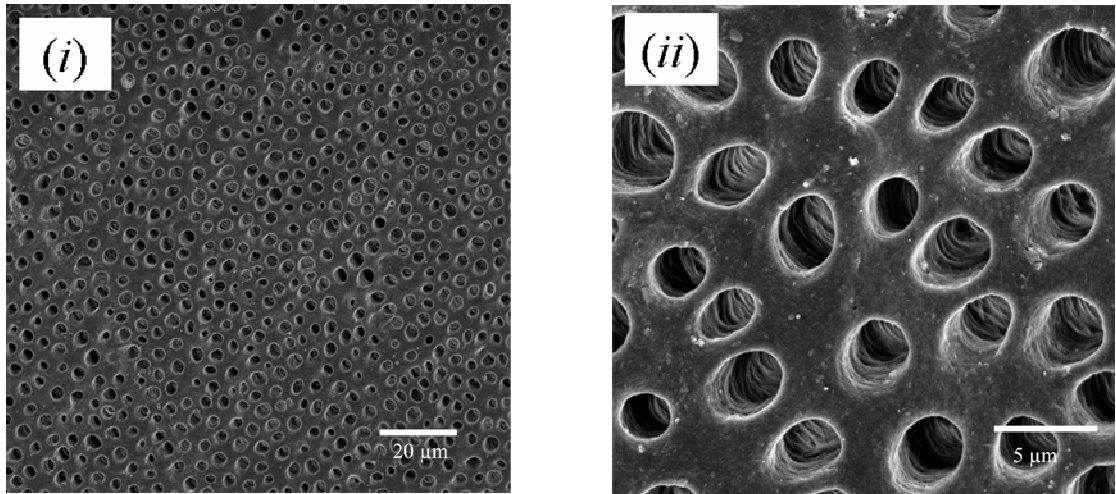
Figure 3.05: FE-SEM images of bovine dentine. Scale bar represents (*i*) 20 μm and (*ii*) 5 μm.

It was also possible to determine the thickness of the dentine disc using FE-SEM, as demonstrated in Figure 3.06(*i*).
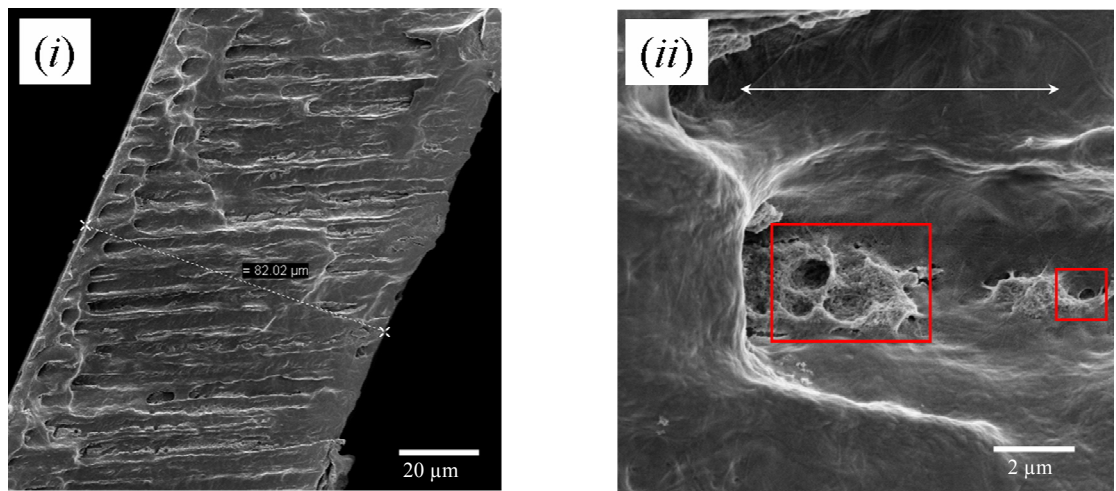
Figure 3.06: FE-SEM images of bovine dentine. (*i*) shows the thickness of the dentine slice (*ca.* 82 μm); (*ii*) is a higher resolution image of a region from (*i*), and shows microtubules (indicated by the red squares) branching normal to the pulp-enamel direction, indicated by the double-headed arrow. Scale bar represents (*i*) 20 μm and (*ii*) 2 μm.

Figure 3.06 (*ii*) shows evidence of branching of the tubules; microbranches running normal to the tubules traversing the dentine in the pulp-enamel direction were visible, as has been seen by others.[11]

3.3   Experimental Details

Initial experiments on dentine investigated the bulk flow characteristics of the substrate. Dentine was prepared as described in Chapter 2.1.1, and the syringe pump flow system set up as described in Chapter 2.1.2. Pressure-time data were measured simultaneously via a digital differential pressure sensor, built in-house.

Initial experiments on alginate sought to quantitatively verify gelation of the substance in the presence of Ca^{2+}. CVs were carried out at a scan rate of 10 mV s^{-1} in a solution containing 5 mM $Ru(NH_3)_6^{3+}$ with 0.1 M KNO_3 as supporting electrolyte. 1 mM $CaCl_2$ was also present in the solution. Increasing amounts of 3% (w/w) sodium alginate gel were added in 0.5 cm^3 aliquots.

For all SECM experiments a 25 μm diameter platinum UME (fabricated as described in Chapter 2.2) was employed as the tip probe. The experiments were set up as described in Chapter 2.1.2. The optimal redox mediator was found to be potassium hexachloroiridate (III), K_3IrCl_6, as will be discussed in section 3.5.1. This was present in the reaction solution at a concentration of 5 mM, with 0.1 M KNO_3 as supporting electrolyte. Also present was Ca^{2+}, in the form of $CaCl_2$, at a concentration of 1 mM. The solution was buffered at a pH of 7.2 using 20 mM HEPES buffer. The solution electrolyte composition was chosen to mimic *in vivo* conditions.

Initially the UME was positioned a large distance (*ca.* 300 μm from the substrate) and a CV recorded. A typical CV is shown in Figure 3.07. The diffusion-limited current, i_∞, was determined from the CV. For subsequent SECM approach curve and *xy* scanning experiments, the potential was held at a sufficiently high value, in this case 1.0 V, in order to oxidise $IrCl_6^{3-}$ at a diffusion-controlled rate.
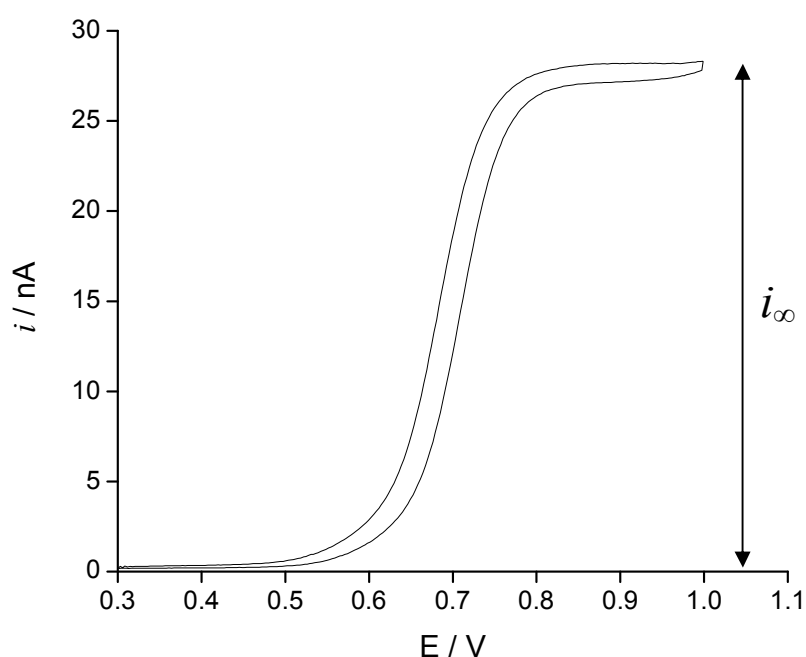
Figure 3.07: A typical CV recorded using a 25 μm diameter Pt UME in a 5 mM solution of $IrCl_6^{3-}$, containing 0.1 M KNO_3 as supporting electrolyte. Also present in solution were HEPES buffer (20 mM) and $CaCl_2$ (1 mM). The observed limiting current (~27 nA) is slightly higher than the expected current from theory (19.78 nA, applying a diffusion coefficient for $IrCl_6^{3-}$ of 8.2 $\times 10^{-6}$ cm s^{-1} [42]); this is probably due to a very slight error in preparing the solution (the observed current would be obtained if the solution had a concentration of 5.0001 mM)

SECM approach curves were carried out to a glass substrate as a means of establishing the tip-substrate distance from measurements of the current. This

method was used to estimate the separation between the UME and the dentine in subsequent experiments, as it was not possible to record a representative approach curve to the dentine itself due to the roughness of the material. This was possible as both set-ups had a parallel alignment in which the sample and UME were perfectly flat. The UME was translated towards the glass disc in the *z* direction at a rate of 1 μm s^{-1} and the current recorded. This tip current (i_t) was then normalised with respect to the diffusion-limited current (i_∞) and the normalised current (i_t/i_∞) plotted against the theoretical approach curve of Kwak and Bard.[43] Such a curve is shown in Figure 3.08.
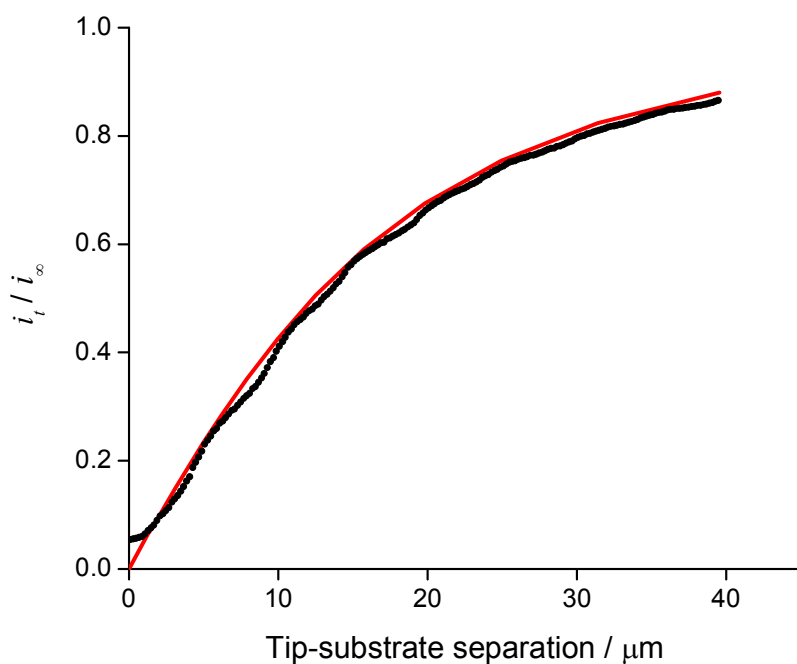
Figure 3.08: A plot showing an experimental approach curve to an insulator (black) fitted to a theoretical approach curve (red) for a 25 μm diameter tip UME with RG = 10.

It is clear from Figure 3.08 that a tip current approximately one third of magnitude of the bulk current (i.e. $i_t/i_\infty \approx 0.3$) corresponds to a tip-substrate separation distance of *ca*. 7 μm. This was deemed to be a sufficient distance from the surface for the tip for *xy* imaging experiments. Care was taken to position the

dentine sample as flat as possible to eliminate the risk of crashing the tip due to a sharp increase in the slope of the sample.

xy scanning experiments were carried out by first positioning the UME a large distance (~ 150 – 200 μm) from the sample and applying a potential to produce i_∞. The UME was then translated toward the dentine using the manual control of the inchworm positioner. The current was monitored as this occurred. When i_t/i_∞ ≈ 0.3 the movement was stopped. A raster scan, typically 400 μm x 400 μm, was then carried out under computer control.

Flow of fluid was effected using the gravity feed system as described in Chapter 2.1.2.

All experimental details for SICM are described in Chapter 2.3.6.

3.4   Bulk Examination of Dentine Permeability

As introduced in Chapter 2.1.1, it was necessary to remove the smear layer[44] from the dentine prior to experiments being carried out. The smear layer is an adherent layer of debris produced during toothbrushing or cutting during dental procedures. It covers the surface of the dentine, thus occluding exposed tubules and reducing permeability. Smear plugs are small masses of this debris that form within the tubules. It has been shown that maleic acid and citric acid both remove the smear layer and partially remove smear plugs. Removing the smear layer and smear plugs meant that the dentine was then as open to flow as possible. Thus, if a treatment were found to be effective in the retardation of this maximum

possible flow, it would be expected to be effective *in vivo* where the fluid flow may not be as great. The etching process was described in Chapter 2.1.1. Optimal etching conditions were determined using pressure transient measurements.

Figure 3.09 shows the results of an initial experiment to investigate the effect that the thickness of the disc had on the pressure increase over a 10 minute period. No significant difference was seen between discs of thickness 50 µm, 100 µm and 200 µm.
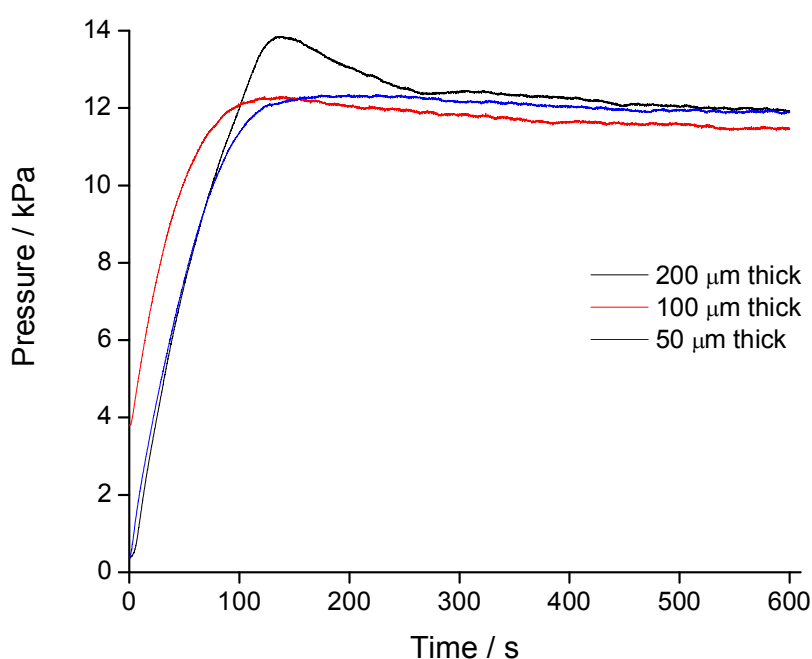
Figure 3.09: Plots of pressure vs time showing the difference in the pressure increase for dentine discs of different thicknesses.

Figure 3.10 shows the effect that etching with 3% citric acid (w/w) for different time periods has on the pressure increase over a ten minute time period.
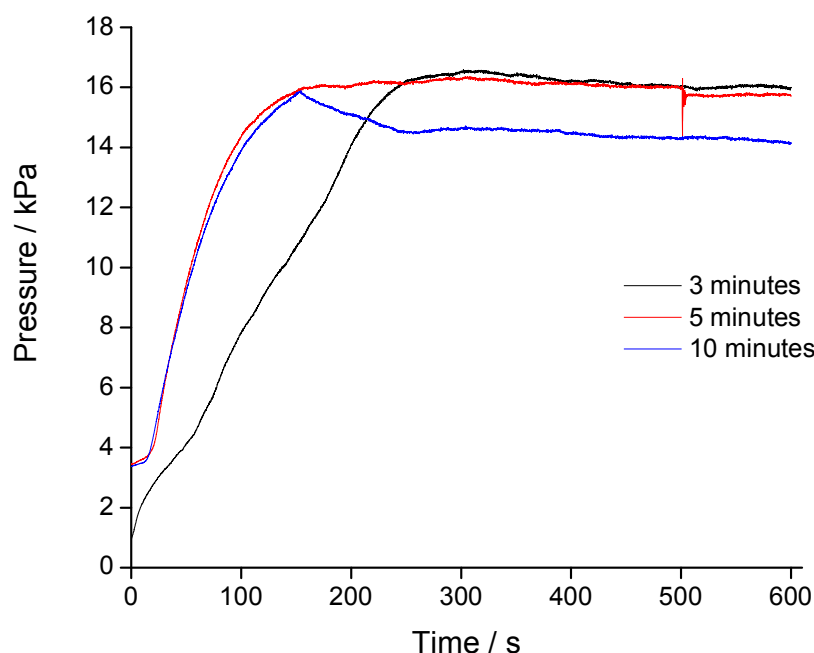
Figure 3.10: Plots of pressure vs time showing the difference in the pressure increase for dentine discs etched with 3% citric acid for different time periods.

It is clear that the pressure increased with time for all the samples in this experiment. This was likely to be due to partially etched debris still attached to the tubule walls breaking free and accumulating within the tubules. No significant difference was seen between the discs etched for 3 minutes and 5 minutes respectively; however there was approximately a 12.5% decrease in the maximum pressure reached for the sample that was etched for 10 minutes in comparison to the other discs. This suggests, as would be expected, that etching for ten minutes opened up the tubules to a greater degree, by removing a larger amount of debris, than etching for three or five minutes.

In the experiments described in this thesis, the effect on fluid flow after applying an alginate gel to the dentine surface was studied by a variety of methods. The simplest method for seeing the bulk effect of the gel on the flow characteristics

of dentine was to make pressure measurements on a dentine disc before and after application of the treatment. The results of this experiment are shown in Figure 3.11.
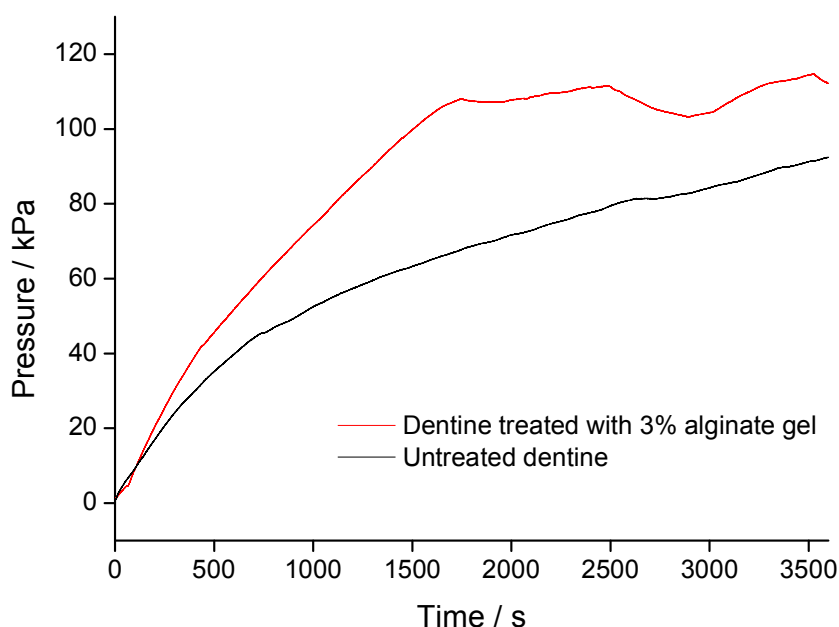
Figure 3.11: Plots of pressure vs time showing the difference in the pressure increase for untreated dentine compared with dentine treated with 3% alginate gel. The flow solution was 1 mM $CaCl_2$.

It is clear that the pressure increase over 60 minutes was greater for the treated dentine than for the untreated dentine. This suggests that the alginate gel blocked the tubules. In addition, the gel appeared to be mechanically stable over this 60 minute time period and thus over this pressure range; had it become mechanically unstable and been forced out of the tubules and off the dentine surface, it would be likely that a sharp decrease in pressure would have been observed. The pressure within the mouth is approximately 14 kPa; the gel was seen to withstand pressures exceeding 100 kPa.

A preliminary electrochemical experiment sought to quantitatively verify gelation of the alginate in the presence of Ca^{2+}. Cyclic voltammograms (CVs) for the reduction of a simple redox mediator were carried out in the presence of increasing amounts of alginate using a 25 μm diameter Pt UME. It was expected that the solution would become more viscous in increasing concentrations of sodium alginate, as it would be expected to form a gel in the presence of Ca^{2+}. This would be detected as a decrease in the current which was greater than the decrease that would be seen due to dilution effects only. The cause of this decrease in the magnitude of the current would be due to the sensitivity of the current to the diffusion coefficient, D, which is affected by both the solution viscosity and the concentration of the redox mediator. The CVs obtained in this experiment are shown in Figure 3.12.
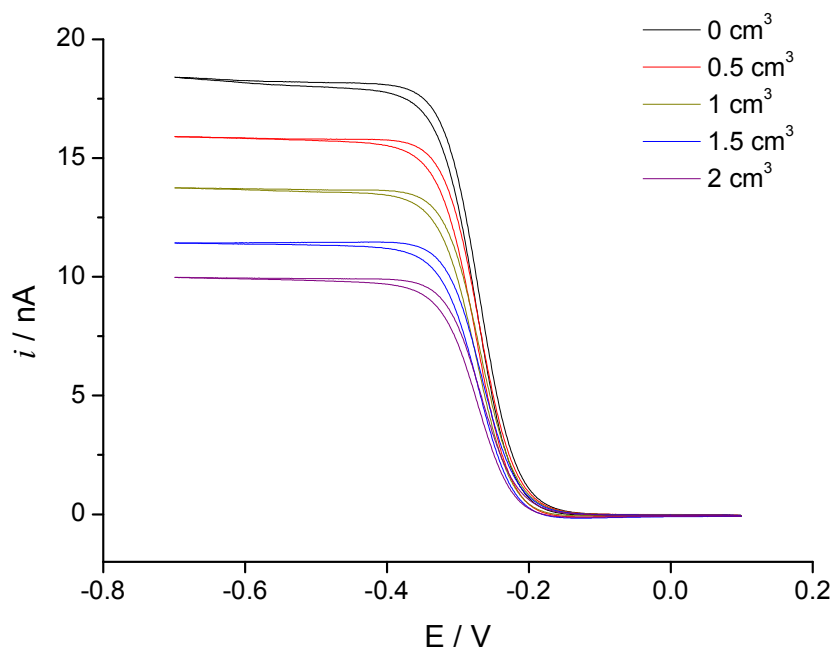
Figure 3.12: A series of cyclic voltammograms (CVs) recorded in 5 mM $Ru(NH_3)_6^{3-}$ with 0.1 M KNO$_3$ as supporting electrolyte. 1 mM CaCl$_2$ was also present in the solution. CVs were run at a scan rate of 10 mV s^{-1}. Increasing amounts of 3% alginate gel were added in 0.5 cm^3 aliquots; black: 0 cm^3 added; red: 0.5 cm^3 added; dark yellow: 1 cm^3 added; blue: 1.5 cm^3 added; purple: 2 cm^3 added.

It is clear that the limiting current, i_∞, decreased as more alginate was added. This could be due to two main factors: (*i*) the alginate gelled in the presence of the 1 mM CaCl$_2$, thus reducing the apparent diffusion coefficient of the $Ru(NH_3)_6^{3-}$; or, (*ii*) the addition of increasing amounts of the alginate gel diluted the concentration of the $Ru(NH_3)_6^{3+}$ and thus i_∞ decreased due to this effect. In fact, both of these factors were found to affect i_∞. The decrease in i_∞ was found to be greater than that expected from only dilution effects, and so must also have been due to the alginate gel decreasing the diffusion coefficient of the $Ru(NH_3)_6^{3+}$. For example, the first addition of a 0.5 cm^3 aliquot of sodium alginate to the 15 cm^3 of 4.34 mM $Ru(NH_3)_6^{3+}$ solution diluted it to a concentration of 4.2 mM. The

expected i_∞ that would be seen for this concentration is 17.83 nA. However, in reality a current of only 15.91 nA was observed, thus the gelling of the alginate must have affected the diffusion coefficient of $Ru(NH_3)_6^{3+}$ and consequently caused a decrease in i_∞. The results are summarised in Table 3.01.

Amount of alginate added (cm^3)	Actual concentration (mM)	Observed i_∞ (nA)	Theoretical i_∞ (nA)	Theoretical % decrease (due to dilution only)	Observed % decrease
0	4.34	18.41	18.41	-	-
0.5	4.2	15.91	17.83	3.15	15.86
1	4.07	13.74	17.28	3.08	13.64
1.5	3.95	11.43	16.77	2.95	16.81
2	3.83	9.98	16.26	3.04	12.69

Table 3.01: Summary of results from CV experiments on the effect of adding 0.5 cm^3 aliquots of 3% alginate gel to a 5 mM $Ru(NH_3)_6^{3-}$ solution in the presence of 1 mM $CaCl_2$. The solution also contained 0.1 M KNO_3.

From these preliminary experiments on the bulk effect of alginate gel, it was clear that the substance showed promise as an effective treatment for dentinal hypersensitivity. The next stage involved making localised measurements of fluid flow across dentine, and investigating the effect of the alginate gel on this fluid flow.

3.5 Localised Examination of Dentine Permeability using SECM

SECM was used to map the topography and permeability of both human and bovine dentine. Initially, it was necessary to find the optimal redox mediator for the studies. This was crucial as it became clear that certain mediators caused undesirable effects during experiments.

3.5.1 Results and Discussion: Examination of Redox Mediators

Initially it was necessary to determine the optimal redox mediator for SECM studies of fluid flow through dentine. The effect of each mediator on the dentine and the UME tip is discussed in this section.

Hexammineruthenium (III) chloride, $Ru(NH_3)_6^{3+}$, is a frequently used cationic redox mediator. Although expensive, it displays considerably superior stability over the majority of other redox mediators, making it an obvious choice for the SECM experiments on dentine. However, it was apparent that there were undesirable effects of using $Ru(NH_3)_6^{3+}$. As discussed in section 3.3.1, Ca^{2+} was added to the mediator solution in order to mimic *in vivo* conditions in the mouth, and also to act as the gelation agent for the alginate films. $Ru(NH_3)_6^{3+}$ was thought to interact with the dentine surface. This occurred in both the absence and presence of Ca^{2+}. Figure 3.13 shows a pressure-time profile for the flow of $Ru(NH_3)_6^{3+}$ through dentine. A pressure increase of 130 kPa was observed over 66 minutes. At this pressure (130 kPa), leaks occurred within the experimental flow system. This large increase in pressure was consistent with the thought that the mediator interacts with dentine to form a precipitate which acts to block the

tubules; cationic mediators such as $Ru(NH_3)_6^{3+}$ interact strongly with the negatively-charged hydroxyl end groups of the hydroxyapatite component of dentine.
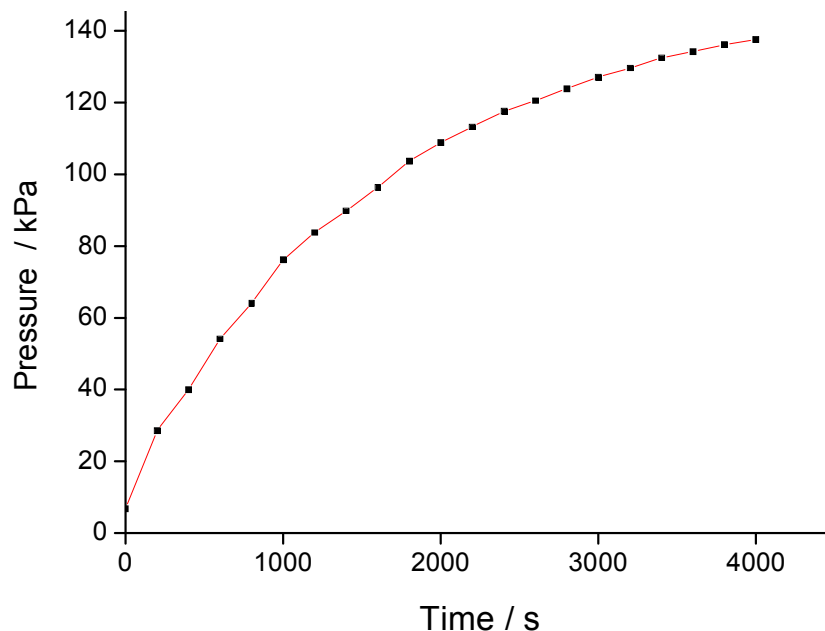
Figure 3.13: Pressure-time profile recorded for flow of $Ru(NH_3)_6^{3+}$ through dentine over 66 minutes.

This significant increase in pressure corresponded with a notable decrease in the tip current, i_t, which was not attributable to fouling of the electrode, and thus represented retardation of the flow rate. This again supported the notion that the tubules were becoming blocked. In order to visualise blocking effects from the mediator itself, a 25 μm diameter UME was scanned over an area of size 400 μm × 5 μm, with a step size of 0.05 μm. This was analogous to scanning the same region repeatedly. $Ru(NH_3)_6^{3+}$ was pumped through the dentine at a rate of 3ml/hr. Figure 3.14 shows images obtained in this manner both in the presence and absence of Ca^{2+}.
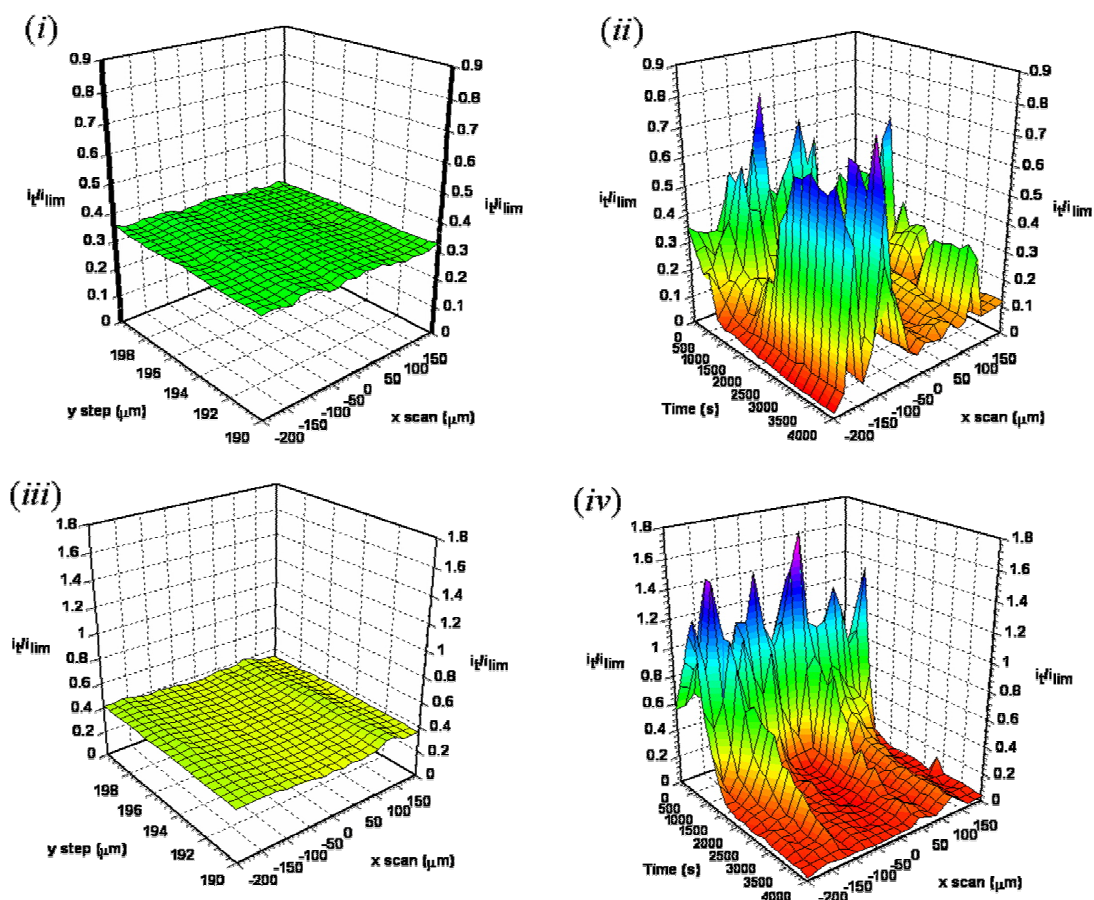
Figure 3.14: Current images for the diffusion controlled reduction of $Ru(NH_3)_6^{3+}$ as a tip UME is scanned over the dentine surface. (*i*) is the image obtained with no flow, and (*ii*) with 3 ml/hr flow, both in the absence of Ca^{2+}. (*iii*) and (*iv*) were both obtained in the presence of Ca^{2+}, and are images acquired with no flow and 3 ml/hr flow respectively. The tip UME ($a = 12.5$ μm) was initially positioned at a distance of 7μm from the surface. The image was recorded with a tip scan rate of 10 μms^{-1}.

The effect of adding Ca^{2+} was clear. In the absence of Ca^{2+} (Figure 3.14(*ii*)), with time and under flow, the dentine appeared to firstly block, and then free itself in certain regions, seen as a decrease in tip current followed by a sharp increase. In the presence of Ca^{2+} (Figure 3.14(*iv*)), the blocking was uniform across the 400 μm scan and was apparently not reversible. Thus Ca^{2+} appears to exacerbate the

interaction between dentine and $Ru(NH_3)_6^{3+}$. The minimum tip currents observed under flow conditions for both samples were lower than those seen under no flow conditions (the tip current effectively maps the topography of the surface). This suggests a precipitation on the surface under flow conditions; effectively the same as reducing the tip-surface separation.

Additionally, bulk current measurements were carried out to determine whether fouling of the UME contributed to the loss in tip current. Figure 3.15 shows the change in i_∞ over 20 minutes. There was a 6.2 % current loss, which is not a significant decrease. Thus, the gross loss in current is likely to be attributed almost wholly to blocking and precipitation effects on (and within) the porous dentine surface.
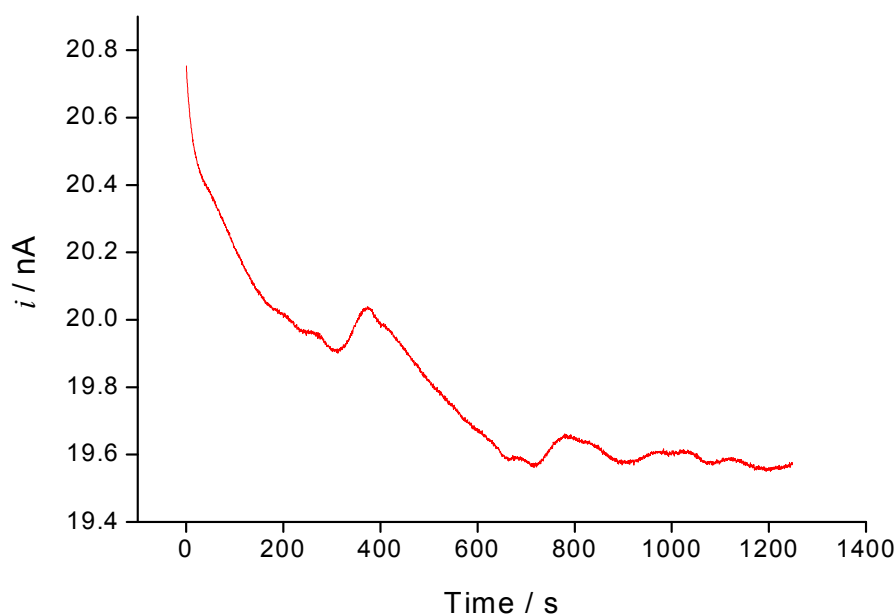
Figure 3.15: *i-t* transient measured for $Ru(NH_3)_6^{3+}$ over a 20 minute period with the tip held at a diffusion-controlled potential.

Neutral mediators, such as ferrocenemethanol, and anionic mediators, such as potassium hexacyanoferrate (II) and potassium hexachloroiridate (III), were not

found to interact with the dentine in the same manner as cationic mediators, as the pressure build-up was not as great. This was true both in the presence and absence of Ca^{2+}. They showed a slight increase in fouling of the UME with time. Figure 3.16 shows a 10.1% decrease in bulk current observed for ferrocenemethanol over a period of 30 minutes.
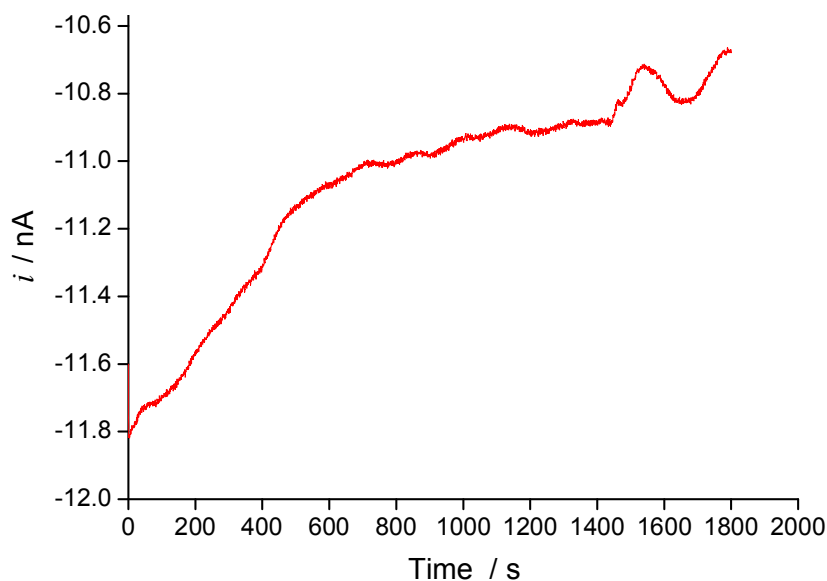
Figure 3.16: *i-t* transient measured for ferrocenemethanol over a 30 minute period

Benzoquinone was also evaluated for its suitability as a redox mediator for this system. However, the mediator suffers badly from decomposition in light, which is a major drawback. In addition, there were stability considerations; initial experiments carried out using a Ag quasi-reference electrode proved difficult and results were poor. A Ag/AgCl reference electrode was introduced instead which improved stability; however, this shifted the potential window more negative, and thus the contribution to the current from oxygen reduction became significant. Degassing the system would have been extremely difficult, as in later experiments treatments were brushed onto the dentine sample, thus necessitating an open system. Thus benzoquinone was rejected as a redox mediator.

During experiments attempted with potassium hexacyanoferrate (II), $Fe(CN)_6^{4-}$, and potassium hexachloroiridate (III), $IrCl_6^{3-}$, it was possible to electrochemically clean the UME between scans by holding at a potential of -1 V for 5 seconds in bulk solution, and thus rectify the loss in tip current due to product fouling. Of the two anionic mediators investigated, potassium hexachloroiridate (III) was found to be the most stable and was utilised in all subsequent SECM experiments on dentine.

3.5.2   Results and Discussion: Effect of Occlusion Actives

The permeability of the dentine substrate was investigated by carrying out large scale (400 μm × 400 μm) *xy* SECM scans in both the absence and presence of fluid flow. A typical set of images is shown in Figure 3.17. The images were obtained (*i*) without the application of a pressure and (*ii*) in the presence of an applied flow rate of 3ml/hr. (*iii*) shows the image obtained on subtraction of (*i*) from (*ii*) in order to remove the topographic effects. In (*i*), ridges that are inherent to the polishing process were clearly visible. Note that this image shows i_t/i_∞ and as such represents an inverted topography image. As in SECM negative feedback, the larger the current ratio the greater the the tip-substrate separation (see Chapter 1.4 for an introduction to SECM). After application of a pressure, large increases in the current were seen. The magnitude of i_t/i_∞ was seen to increase to values well above 1 (ie a positive feedback response was seen), indicating that the sample was highly amenable to flow as there was now a convective response contributing to the current due only to hindered diffusion. (*iii*) shows the current due to convection only, with topographical considerations removed.
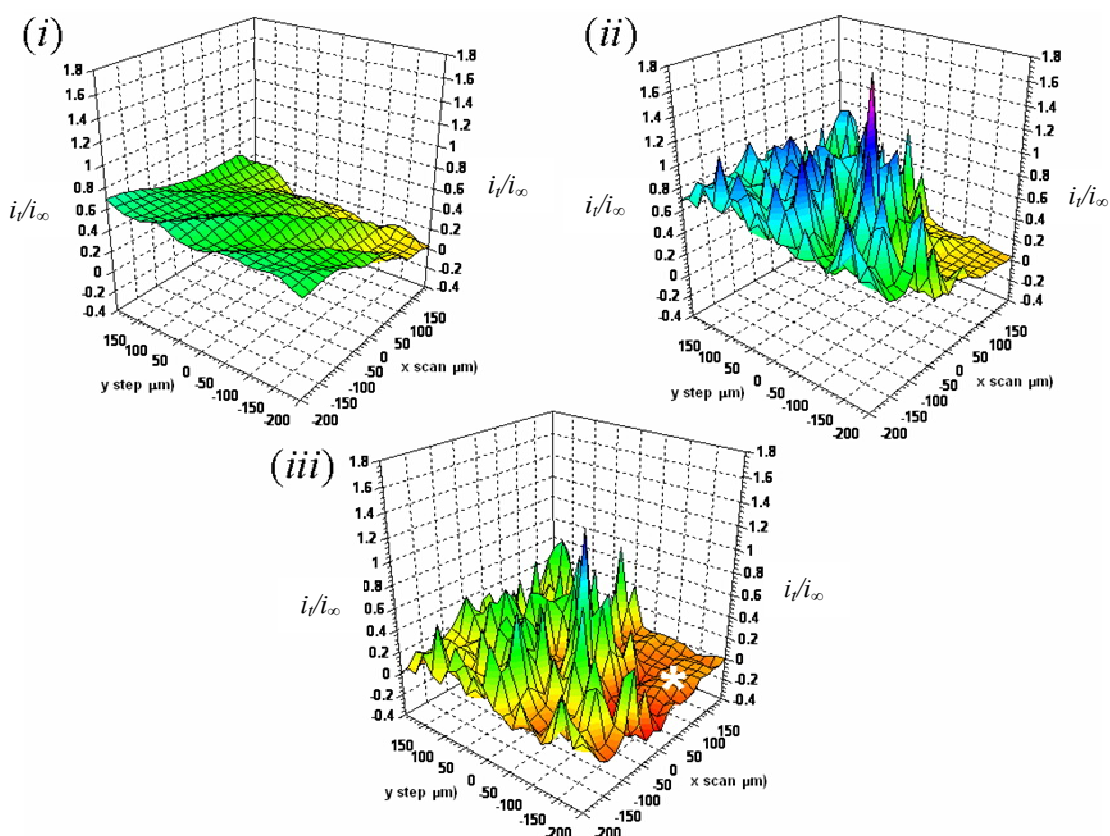
Figure 3.17: Large scan current images for the diffusion-controlled oxidation of $IrCl_6^{3-}$ as a tip UME is scanned over the dentine surface. (*i*) is the image obtained with no flow, and (*ii*) with 3ml/hr flow. (*iii*) is the image obtained on subtraction of (*i*) from (*ii*), i.e. the image due to convection only. The tip UME (*a* = 12.5 μm) was initially positioned at distance of 7 μm from the surface. All images were recorded at a tip scan rate of 10 μm s^{-1}.

The data recorded inferred that the sample was active to flow, but on inspection of the images it was clear that this flow was spatially heterogeneous. It is also of note that the UME employed as the imaging tip in these experiments had a diameter of 25 μm. The dentinal tubules ranged in diameter from 2 – 5 μm, thus the UME was likely to be detecting fluid flow through regions containing a number of tubules, rather than through individual tubules themselves. If a smaller UME were utilised, it would be possible to resolve much smaller areas, even

individual tubules.[29] However, employing a larger electrode allowed larger scan areas to be imaged without fear of tip crash on the surface.

A pressure sensor was introduced to the system so that pressure changes could be monitored over the course of the experiments. Figure 3.18 shows a typical pressure-time profile for $IrCl_6^{3-}$ transport across dentine at a flow rate of 3 cm^3 hour^{-1}.
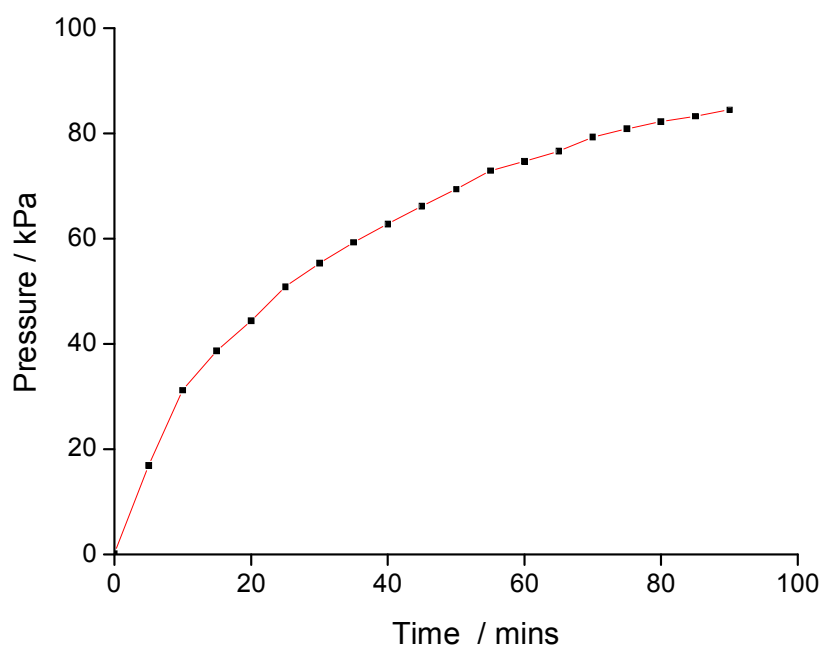
Figure 3.18: Pressure-time profile recorded for flow of $IrCl_6^{3-}$ at a flow rate of 3 cm^3 hour^{-1} through dentine over 90 minutes.

As described earlier in this chapter (section 3.4) the pressure is seen to increase over time. The pressure increase is shown over 90 minutes, a typical length of time for an experiment. The pressure increase was likely to be due to loose dentine fragments present on the tubule walls being disturbed by the fluid flow and consequently becoming lodged within the tubules. Thus, in some regions of

the dentine, flow may be retarded. Note that the increase in pressure for flow of $IrCl_6^{3-}$ over the 90 minute time period is not as great as that observed for $Ru(NH_3)_6^{3+}$ over a 66 minute period (80 kPa vs 130 kPa).

In subsequent experiments, a paste containing 3% alginate gel as a candidate active for dentinal hypersensitivity was applied to dentine, and its effect on fluid flow investigated. This was carried out at 3 different pH values; 6, 7 and 8. For these experiments, a gravity feed system was used to induce fluid flow rather than a syringe pump. This system consisted of a reservoir containing the redox species in solution, which was attached to the capillary in the same manner as the syringe pump in previous experiments, and was held at a set distance above the dentine, in this case 20 cm. This allowed the applied pressure to be maintained at *ca*. 2 kPa, analogous to the pressure within the mouth. Figure 3.19 shows a typical series of images obtained at pH 6.
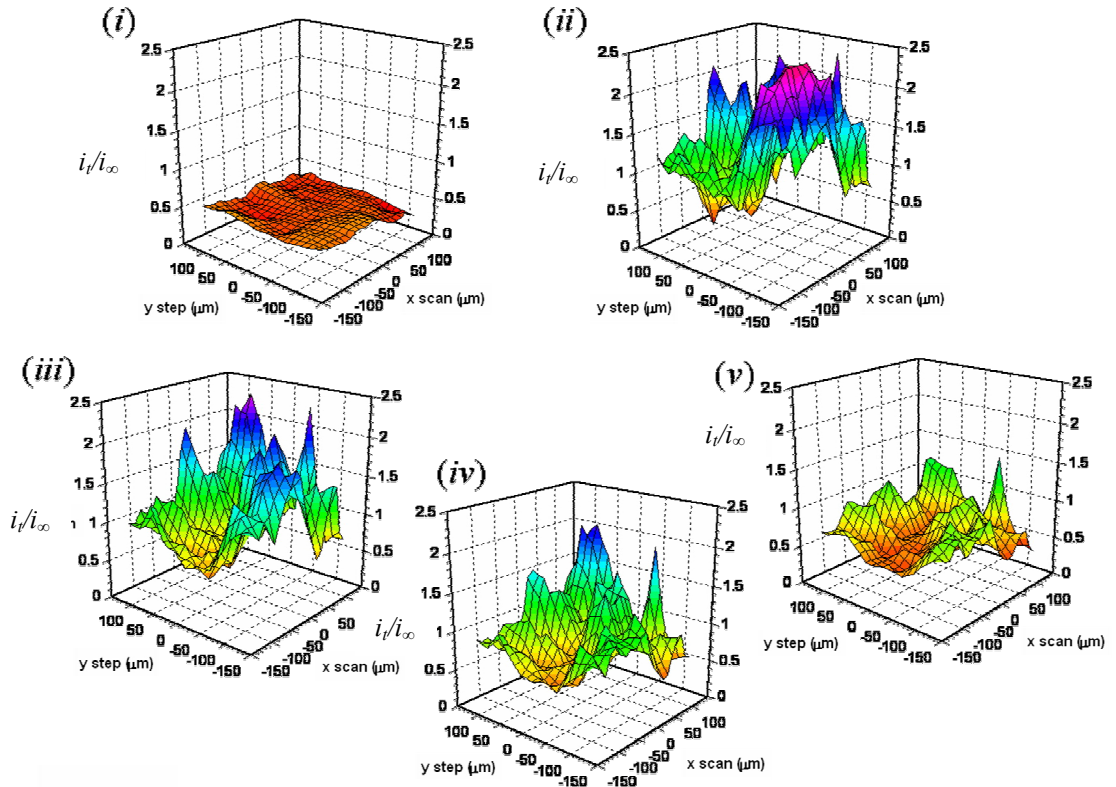
Figure 3.19: Series of SECM images showing i_t/i_∞ for: (*i*) a dentine sample with no applied pressure; (*ii*) the same sample after application of a pressure of 2 kPa using a gravity feed system; (*iii*), (*iv*) and (*v*) the same sample after 1, 2 and 3 applications, respectively, of a paste containing 3% alginate gel as a candidate active for dentinal hypersensitivity.

It is clear from (*i*) and (*ii*) that there was a significant increase in the current on application of a pressure of 2 kPa. After the first application of the paste, the current was seen to decrease, most notably in the areas of the dentine sample that were most active to flow. This decrease was made significantly more obvious with the second and third applications of the paste.

A negligible difference was seen between the results obtained at all three pH values, suggesting that the paste would behave in this manner in the mouth itself. This pH range was chosen as the pH of the mouth is likely to stay within these

values for the vast majority of the time[45] so it was important to probe the action of the alginate gel over this range.

3.6 Scanning Ion Conductance Microscopy (SICM)

SICM enables higher resolution imaging than SECM on rougher surfaces as it is easier to build in feedback control. Thus SICM was employed to further investigate the morphology of dentine.

3.6.1 Introduction

SICM was first developed in 1989 by Hansma and co-workers[46] and was introduced in Section 1.5. Here the technique will be discussed in more detail.

3.6.1.1 Operating Modes of the SICM

The simplest mode of operation of the SICM is constant height mode,[46] as briefly discussed in Section 1.5. Here the tip is scanned across the sample at a particular distance from the substrate, analogous to the constant height mode of SECM, as discussed in Chapter 3. There is a major drawback to this method, however. As with SECM, there is a fundamental risk of tip crash due to encounters with prominent features of the substrate. In SICM this risk is increased as the approach characteristics of the SICM tip are much more subtle than that of the SECM tip. Figure 3.20 shows a typical approach curve to a glass substrate for a 4 μm diameter SICM tip filled with 0.1 M NaCl. The reservoir was also filled with 0.1 M NaCl. Ag/AgCl electrodes served as the two reference electrodes located within the pipette and in the reservoir. This approach behaviour has important

consequences, both for constant height imaging and also for imaging using a constant current feedback loop.
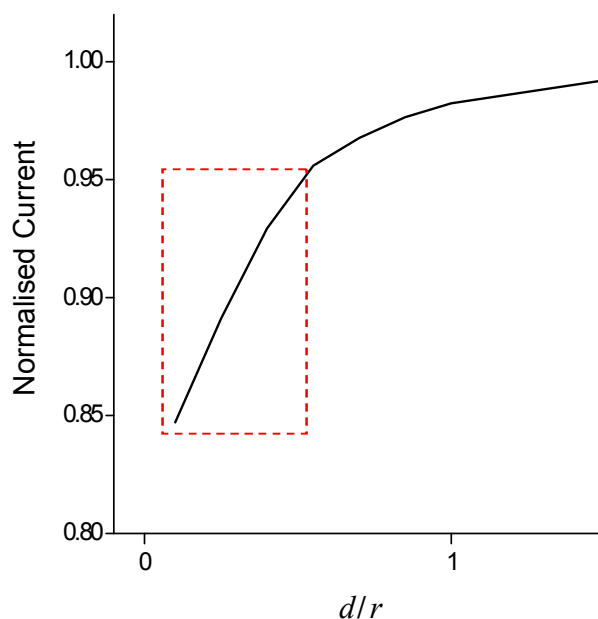
Figure 3.20: A typical SICM approach curve to a glass substrate for a 4 μm diameter micropipette, where the tip current is normalised with respect to the bulk current and plotted against the tip-substrate separation (*d*) expressed in tip radii (*r*). In this case *r*=2 μm. The micropipette and reservoir were both filled with 0.1 M NaCl. 2 Ag/AgCl electrodes served as the reference electrodes within the micropipette and in the reservoir.

It is clear that the majority of the change in current occurs over a very small distance when *d*/*r* is < 0.5. The red rectangle denotes the region of the curve in which there is a large change in current when there is a very small change in *d*. These approach characteristics present a challenge to the experimentalist when deciding on a value of *d* which would be suitable for imaging the substrate. It is obvious that maximum changes in the current with changing *d* are seen when within a tip radius of the sample; however imaging at such a close proximity in constant height mode clearly exacerbates the danger of tip crash. As such, this mode is not often utilised in SICM studies.

In the case of the constant current feedback mode,[46] there are two major considerations. Firstly, if the set-point for feedback is chosen in the steep area of the curve, where d is less than r, changes in the current will have the maximum effect on the vertical tip position. However, as with constant height imaging, the tip may encounter a prominent feature on the sample and become damaged. Conversely, if the set-point is chosen in the flatter region of the curve, where d is larger than r, then there is enough space for a "sensing sphere" to establish at the end of the tip, as shown in Figure 3.21.
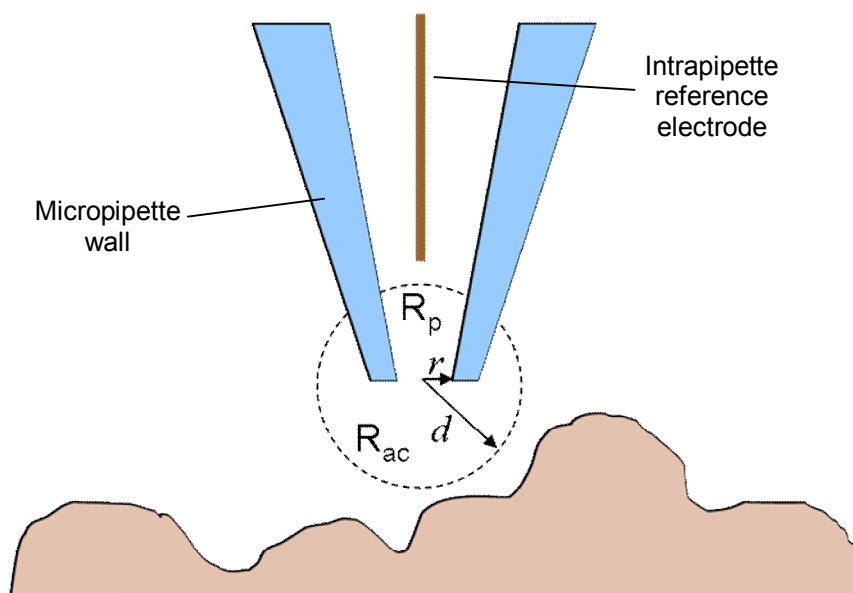
Figure 3.21: Schematic diagram representing the resistances associated with the micropipette, where R_p is the resistance due to the micropipette and R_{ac} is the access resistance of the micropipette aperture.

This "sphere" is capable of sensing lateral obstacles (within reason) and so allows the tip to scan at a particular value of d whilst reducing the probability of tip crash. The major problem with this mode of operation is the extremely steep current-distance gradient which results in a current ratio of 0.85 being attained

before the tip crashes into the surface. As such, Figure 3.20 represents the best achievable experimental approach curve; moving to the next position in the *z* direction would cause the tip to crash into the surface, even with a step size of only 100 nm. As such, the maximum achievable decrease in current is approximately 15%. This is not a particularly robust signal to lock into for feedback as it would involve trying to hold the current at a value close to bulk, and even a small amount of noise would disrupt this. The studies detailed in this thesis used a slightly different mode of operation; oscillating the micropipette tip and feeding back on the derivative of the DC current, calculated by measuring the amplitude (in this thesis the amplitude was measured peak-to-peak, abbreviated p2p) of the AC current induced by the oscillations of the tip. Figure 3.22 demonstrates the reasons behind using this signal to feed back on.
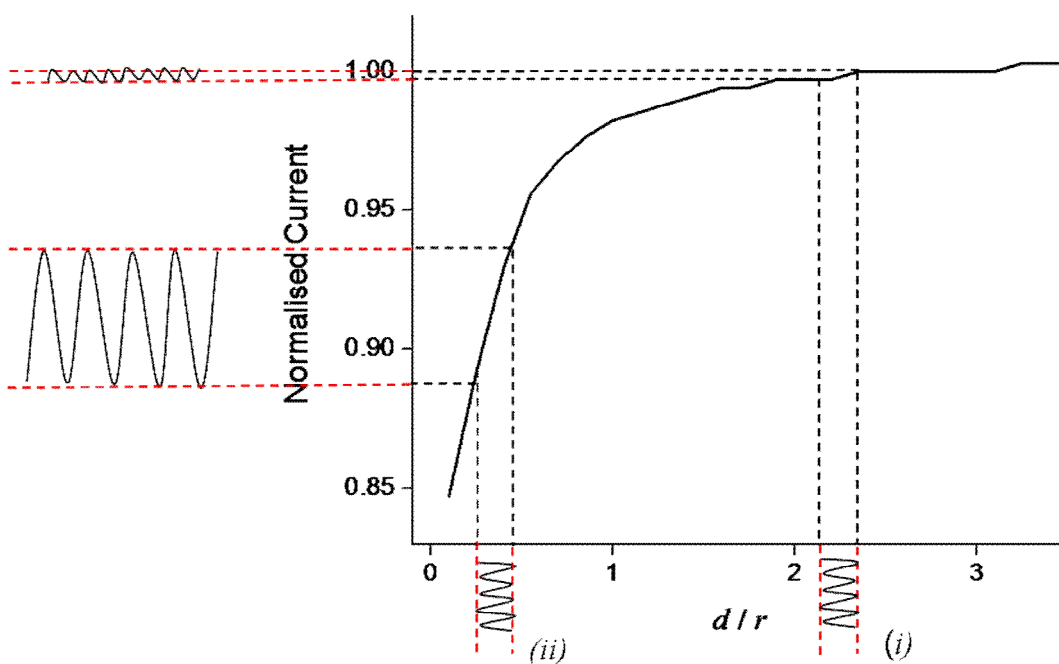
Figure 3.22: Schematic demonstrating the effect of tip oscillation on the tip current. (*i*) shows the effect of oscillating the tip when it is positioned far from the surface; (*ii*) exhibits the effect on tip current when the tip is close to the surface.

Figure 3.22 demonstrates two regimes. In both cases the tip is oscillated in the *z* direction (ie perpendicular to the surface) over the same set distance. In case (*i*) the tip is a great distance from the surface, and oscillating the tip causes trivial oscillations in the current. In case (*ii*), the tip is close to the surface and as such oscillating the tip causes a much larger oscillation in the current. Thus, the amplitude of the current increases greatly as the surface is approached. Figure 3.23 demonstrates the superior change in the AC current in comparison to the change in the DC mean current over the same approach distance.
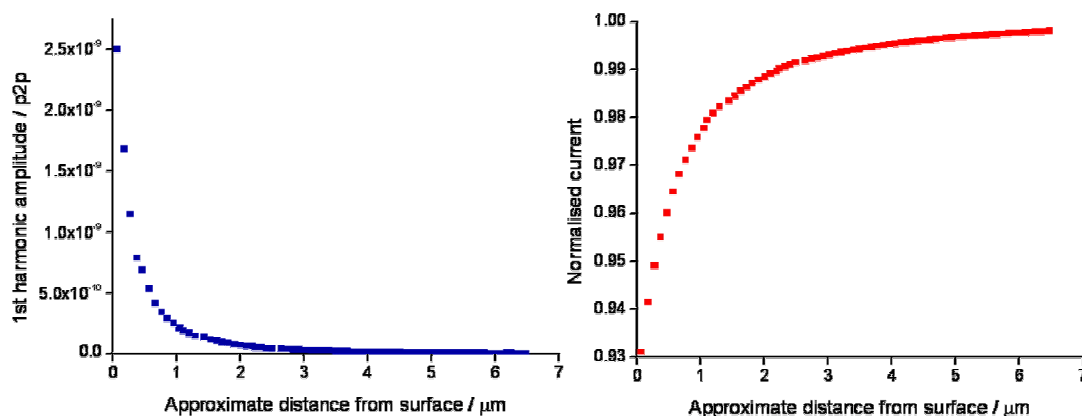
Figure 3.23: Figure to compare the response of the AC current (blue) and the DC current (red) for a 4 μm micropipette tip over the same approach distance (7 μm). The magnitude of the AC current (ie the first harmonic amplitude of the DC current) was measured from peak-to-peak (p2p).

This approach to SICM provides a robust signal to lock into (ie the 1st harmonic amplitude of the AC current) for *xy* imaging experiments.

3.6.2   Calibration of the SICM

The experimental set-up is described in Chapter 2.3.6. In order to calibrate the SICM, two model surfaces were considered. The first of these consisted of a

series of parallel bands which were 5 µm in width, separated by 20 µm and raised from the plane by 0.5 µm. These were fabricated using a mask aligner to define the pattern on a silcon wafer substrate coated in a photoresist (Microposit 1805, Shipley, USA). Images of this substrate, obtained using optical microscopy and SICM, are shown in Figure 3.24.
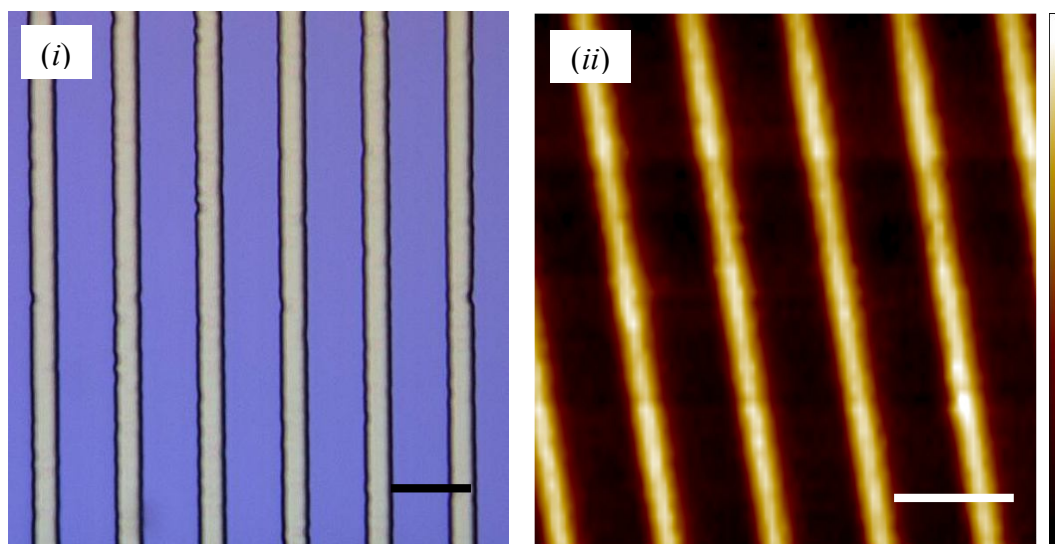
Figure 3.24: (i) Optical and (ii) SICM image (micropipette diameter 1 µm) showing a substrate consisting of bands 5 µm in width, separated by 20 µm, that are raised 0.5 µm from the plane. The *xy* scale bar in both images represents 25 µm; the *z* scale bar for the SICM image (*ii*) runs from 0 (black) to 0.5 (white) µm.

The SICM images were carried out using the AC feedback mode of the instrument, with a 3.5 µm diameter tip oscillating over 40 nm at a frequency of 80 Hz. An image 100 µm × 100 µm was recorded with a step size of 1 µm in the *y* axis and 1.25 µm in the *x* axis. The reservoir and micropipette solutions were both 0.1 M NaCl. The precise fabrication of the banded structure meant that the substrate was a good indicator that the SICM was functioning correctly. Figure 3.25 shows the effect that changing the set point for the feedback mechanism has on the resolution of the SICM images.
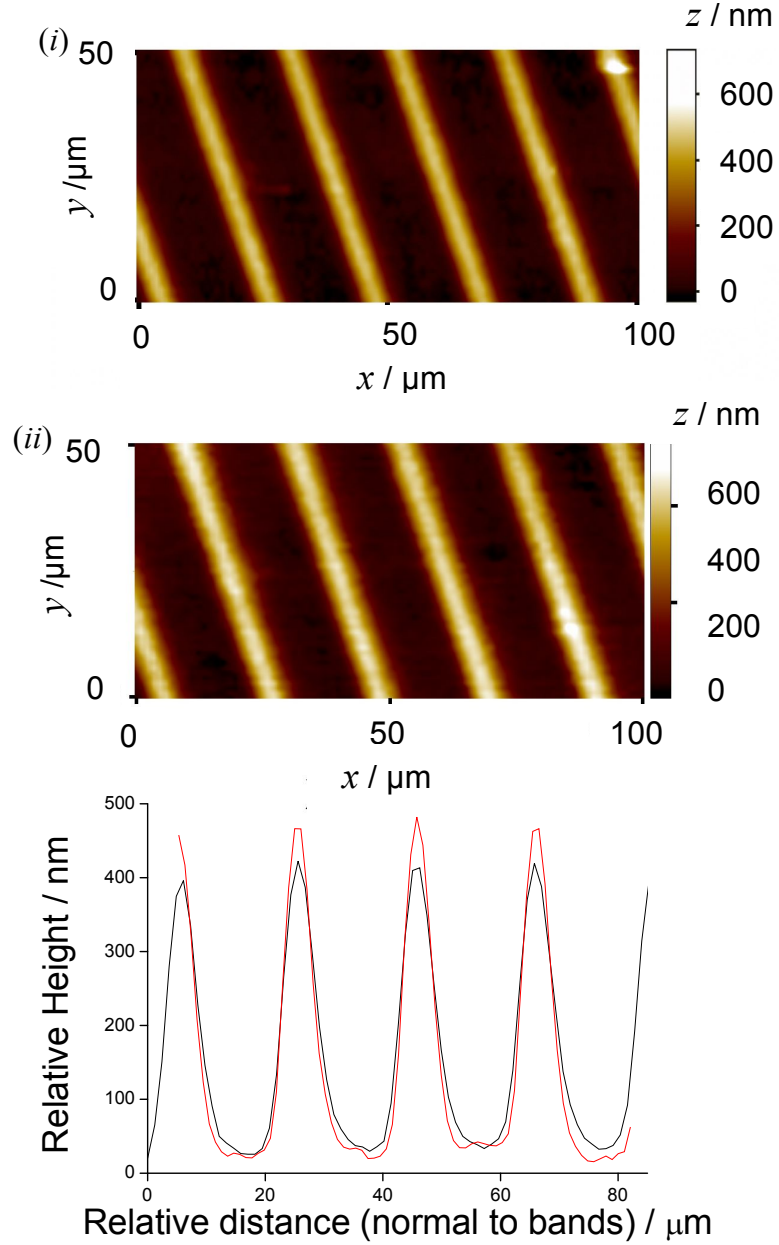
Figure 3.25: SICM images of the raised band structure on silicon wafer, recorded with a 3.5 μm diameter micropipette under feedback utilising the first harmonic, with two different set-points. The tip was oscillated over 40 nm at a frequency of 80 Hz. The substrate had band width 5 μm and band height 0.5 μm, with a 20 μm repeating pattern. (*i*) and (*ii*) are images recorded over the same 100 × 50 μm area, with the set point of (*i*) approximately 0.85 μm closer to the surface than the set-point for (*ii*). (*iii*) shows the average cross section in the direction normal to the bands for (*i*) black and (*ii*) red. Lines have been shifted so that the flat areas between bands match approximately.

The images in Figure 3.25 (*i*) and (*ii*) show that the closer the set point is to the surface, the better the resolution of the SICM image recorded. Figure 3.25 (*iii*) demonstrates this quantitatively; the height of the bands elucidated from image (*ii*), ie the image recorded with the set point closer to the surface, are *ca.* 450 nm, compared with *ca.* 400 nm for the image recorded with the set point further from the surface. The actual height of the bands was 500 nm.

To further calibrate the instrument, a standard AFM calibration grid was utilised. An SICM tip with diameter 1 μm was used for imaging. A typical image is shown in Figure 3.26.
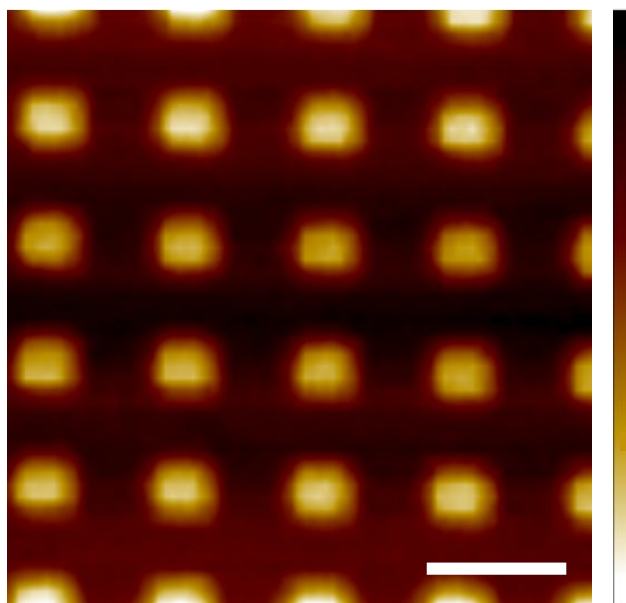
Figure 3.26: SICM image of a calibration grid consisting of 5 μm × 5 μm squares raised 180 nm from the plane. The image was recorded using a 1 μm diameter tip filled with 0.1 M NaCl. The reservoir was also filled with 0.1 M NaCl. The tip was oscillated over 40 nm at a frequency of 80 Hz. The *xy* scale bar represents 10 μm; the *z* scale bar runs from 0 (white) to 185 (black) nm.

The correlation between an AFM image and a SICM image of the calibration grid, together with cross-sections of each, is shown in Figure 3.27.
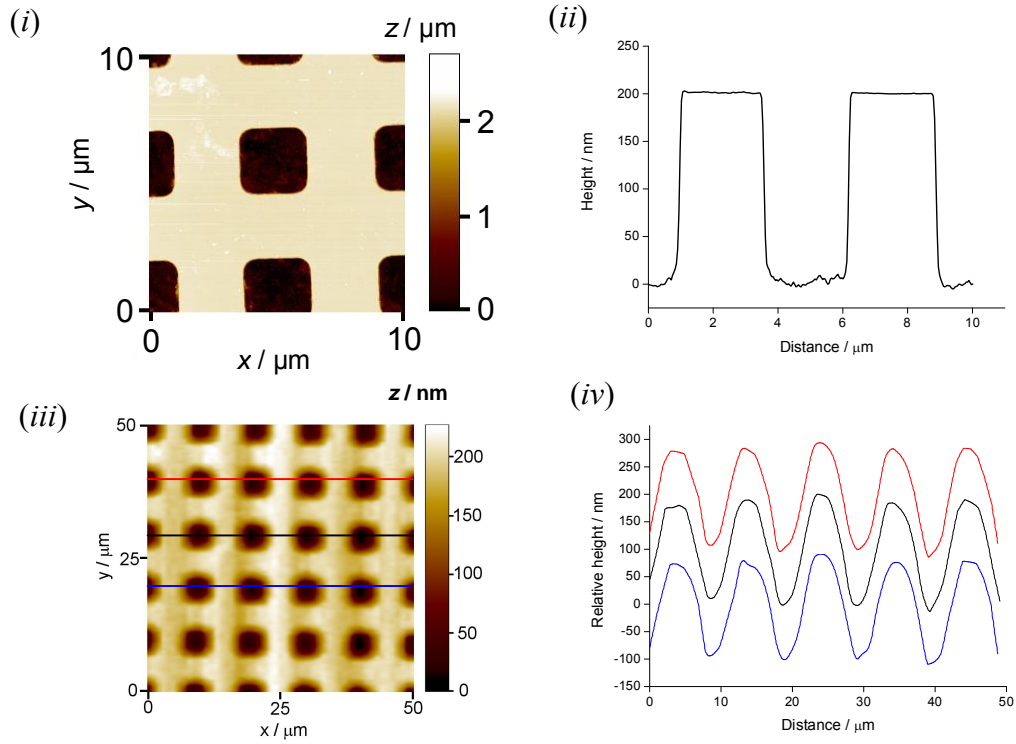
Figure 3.27: Images of a calibration grid, 10 μm pitch, 180 nm depth, recorded using contact-mode AFM (*i*) and (*ii*) or and SICM (1 μm diameter pipette) (*iii*) and (*iv*). (*ii*) and (*iv*) are cross-sections of the 2-dimensional images taken from (*i*) and (*iii*), respectively. Curves in (*iv*) have been offset from one another in the vertical direction to aid clarity.

It is clear that there is an artefact associated with the SICM technique. Figure 3.27 (*i*) and (*iii*) show the capability of the AFM to follow the topography of a substrate accurately. Note that the profile of the pits demonstrates how the AFM tip followed the vertical walls precisely. In contrast, the profile of the pits imaged using SICM (Figure 3.27 (*ii*) and (*iv*)) shows how the tip followed a slope into the pits. This resulted in slightly blurred edges in the SICM images. This effect is illustrated schematically in Figure 3.28.
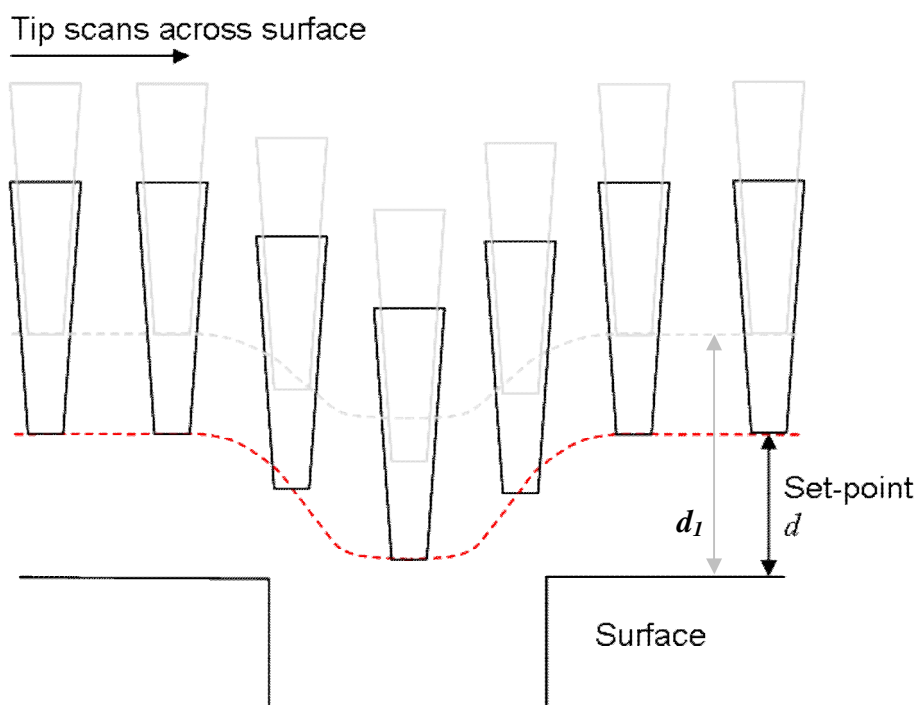
Figure 3.28: Schematic illustrating the path tracked by the SICM tip as it scans over a step at two different set points ($d_1 > d$).

It is noticeable that the step affects the tip position normal to the surface over relatively long lateral distances. Clearly the greater the set-point (ie the larger the tip –surface separation), the more blurred the feature appears in the SICM image. In order to understand the artefact, the ion paths accessible to the tip must be considered, and are illustrated schematically in Figure 3.29.
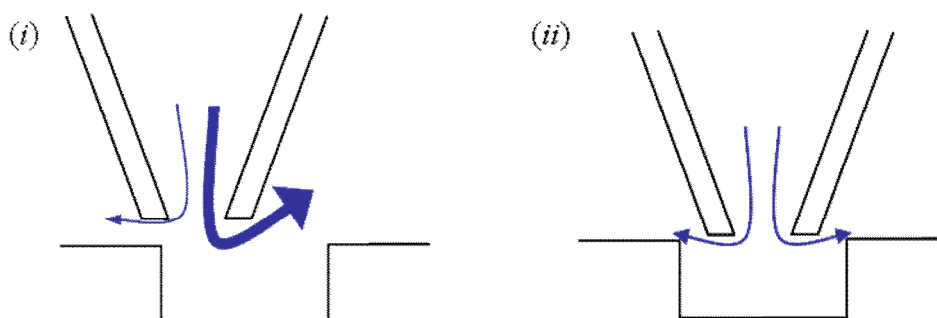
Figure 3.29: Schematic showing the path of ion flow as a pipette is positioned above a pit, either (*i*) offset or (*ii*) coaxially over a pit.. The weight of the arrow is demonstrative of the relative magnitude of the ion flux out of the pipette. NB: there will be a net flow equal and opposite to this to balance the charge.

As shown in Figure 3.29, as the pipette encounters a pore the ion flow increases for a certain region of the pipette, and so the current increases. Thus, the feedback mechanism causes the pipette to begin to move closer to the surface to counteract this. This explains the slope the tip follows as it encounters a pore. Once the pipette is positioned directly over the pore, the ion flow occurs at the same magnitude in all directions out of (and in to) the pipette and so the pipette remains at the same height.

3.6.3 SICM Imaging of Dentine

To further assess the imaging capabilities of the SICM, a slice of bovine dentine was imaged, as shown in Figure 3.30.
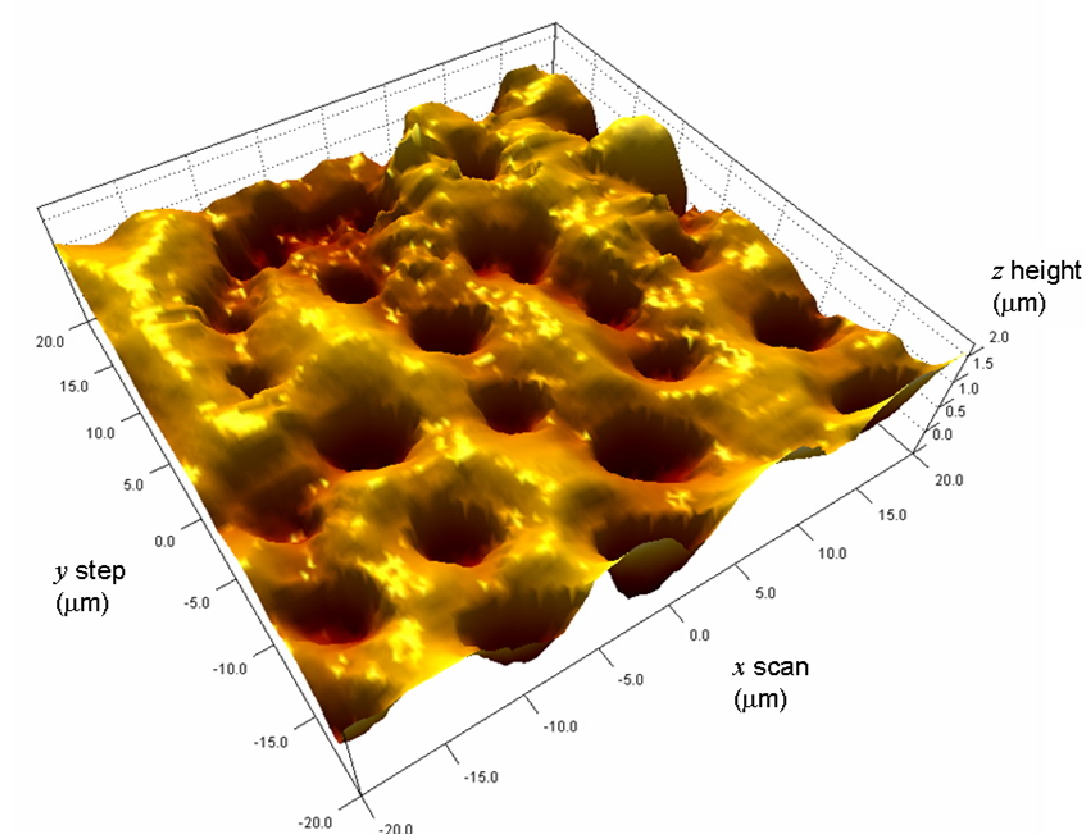
Figure 3.30: An SICM image of dentine recorded using a 3 μm diameter micropipette containing 0.1 M NaCl. The tip was oscillated over 40 nm at a frequency of 80 Hz.

A micropipette of diameter 3 µm was employed to record the high resolution image. The tubules in the dentine are clearly visible, as are features on the surface showing the roughness of the sample.

3.7   Conclusions

SECM and SICM have been shown to be powerful techniques for imaging dentine. SECM was utilised in order to investigate the effect of blocking agents on the flow of fluid, namely a redox mediator, through the dentine substrate. The results obtained using SECM suggest that alginate may be an effective active for the occlusion of dentinal tubules across a range of pH values.

SICM has been developed and calibrated using two substrates, and has allowed high resolution images of dentine to be obtained. There is much scope for further development of this technique and in future it may be applied to investigate the movement of ions across the dentine substrate.

3.8   References

(1)   P. Dowell, M. Addy *J. Clin. Periodont.* **1983**, *10*, 341.

(2)   L.P Gartner, J.L. Hiatt In *Color Atlas of Histology,* 4th ed.; Lippincott

Williams & Wilkins: Baltimore, MA, USA, 2006, pp 260.

(3)   D.Scott, T.R.Tempel *J. Dent. Res.* **1965**, *44*, 20.

(4)   M. Brännström *Archs. Oral Biol.* **1962**, *7*, 59.

(5)   D.J. Anderson, M.P. Curwen, L.V. Howard *J Dent. Res.* **1958**, *37*, 669.

(6)   M. Brännström, A. Åström *J Dent. Res.* **1964**, *43*, 619.

(7)   M.R. Byers *Archs. Oral Biol.* **1994**, *39 (S)*, S13.

(8)   A. Gysi *J. Dent. Sci.* **1900**, *43*, 865.

(9)   M. Brännström In *Sensory Mechanisms in Dentine*; Anderson, D. J., Ed.;

Pergamon Press: Oxford, 1962, pp 73-79.

(10)   N. Vongsavan, B. Matthews *Archs. Oral Biol.* **1992**, *37*, 175.

(11)   I.A. Mjör, I. Nordahl *Archs. Oral Biol.* **1996**, *41*, 401.

(12)   D.H. Pashley, H.J. Andringa, G.D. Derkson, S.R. Kalathoor *Archs. Oral

Biol.* **1987**, *32*, 519.

(13)   B. Ciucchi, S. Bouillaguet, J. Holz, D. Pashley *J. Endodont.* **1995**, *21*,

191.

(14)   J. Camps, V. Santin, R. Rieu, J. Fuseri, J.C. Franquin *Archs. Oral Biol.*

1996, *41*, 837.

(15)   O.W. Reeder, R.E. Walton, M.J. Livingston, D.H. Pashley *J. Dent. Res.*

1978, *57*, 187.

(16)   E.R. Van der Graaf, J.J. Ten Bosch *Archs. Oral Biol.* **1988**, *33*, 375.

(17)   A.R. Özok, M.-K. Wu, P.R. Wesselink *J. Dent.* **2002**, *30*, 107.

(18)   W.C. Outhwaite, D.M. McKenzie, D.H. Pashley *J. Dent. Res.* **1974**, *53*, 1503.

(19)   D.H. Pashley, W.G. Matthews, Y. Zhang, M. Johnson *Archs. Oral Biol.* **1996**, *41*, 1065.

(20)   D.H. Pashley, W.G. Matthews *Archs. Oral Biol.* **1993**, *38*, 577.

(21)   N. Vongsavan, B. Matthews *Archs. Oral Biol.* **1991**, *36*, 641.

(22)   D.H. Pashley, R. Nelson, E.L. Pashley *Archs. Oral Biol.* **1981**, *26*, 707.

(23)   D.H. Pashley *Dental Clinics of North America* **1990**, *34*, 449-473.

(24)   H. Griffiths, G. Morgan, K. Williams, M. Addy *J. Periodont. Res.* **1993**, *28*, 60.

(25)   F. Greenwood, H. Horiuchi, B. Matthews *Archs. Oral Biol.* **1972**, *17*, 701.

(26)   E.R. Scott, H.S. White, J.B. Phipps *Anal. Chem.* **1993**, *65*, 1537.

(27)   J.V. Macpherson, D. O'Hare, P.R. Unwin, C.P. Winlove *Biophys. J.* **1997**, *73*, 2771.

(28)   S. Nugues, G. Denuault *J. Electroanal. Chem.* **1996**, *408*, 125.

(29)   J.V. Macpherson, M.A Beeston, P.R. Unwin, N.P. Hughes, D. Littlewood *J. Chem. Soc., Faraday Trans.* **1995**, *91*, 1407.

(30)   J.V. Macpherson, M.A. Beeston, P.R. Unwin, N.P. Hughes *Langmuir* **1995**, *11*, 3959.

(31)   J.V. Macpherson, P.R. Unwin *Electroanalysis* **2005**, *17*, 197-204.

(32)   A.M. Cherng, L.C. Chow, S. Takagi *Archs. Oral Biol.* **2004**, *49*, 91.

(33)   D.H. Pashley, J.G. Leibach, J.A. Hornert *J. Periodont.* **1987**, *58*, 19.

(34)   K. Markowitz, K. Bilotto, M.-T. Lui, Y.-T. Jou, S. Kim *Archs. Oral Biol.* **1991**, *36*, 1.

(35)   K. Markowitz, S. Kim *Proc. Finn. Dent. Soc.* **1992**, *88*, (supp 1) 39.

(36)   M. Kagayama, Y. Sasano, H. Sato, S. Kamakura, K. Motegi, I. Mizoguchi *Anat. Embryol.* **1999**, *199*, 233.

(37)   N. Silikas, D.C. Watts, K.E.R. England, K.D. Jandt *J. Dent.* **1999**, *27*, 137.

(38)   M. Yoshiyama, Y. N., K. Ozaki, A. Uchida, Y. Ishikawa, H. Ishida *J. Dent. Res.* **1990**, *69*, 1293.

(39)   H.F. Thomas, R.C. Payne *J. Dent. Res.* **1983**, *62*, 532.

(40)   R. Schilke, J.A. Lisson, O. Bauß, W. Geurtsen *Archs. Oral Biol.* **2000**, *45*, 355.

(41)   J. Liu *Materials Characterization*, *44*, 353-363.

(42)   J.F. Llopis, F. Colom In *Encyclopedia of Electrochemistry of the Elements*; Bard, A. J., Ed.; Marcel Dekker: New York, 1976; Vol. 6, pp 224-226.

(43)   J. Kwak, A. Bard *Anal. Chem.* **1989**, *61*, 1221.

(44)   D.H. Pashley *J. Endodont.* **1986**, *12*, 465.

(45)   A.J. Preston, W.M. Edgar *J. Dent.* **2005**, *33*, 209-222.

(46)   P.K. Hansma, B. Drake, O. Marti, S.A.C. Gould, C.B. Prater *Science* **1989**, *243*, 641-643.

Chapter 4

Laser Scanning Confocal Microscopy (LSCM) Studies of the Permeation of Dentine by Rhodamine B

In this chapter, laser scanning confocal microscopy (LSCM) is introduced as a new complementary approach for imaging flow across porous materials, supported by a simple method for measuring hydraulic permeability.

4.1   Introduction

The transport of chemical species across synthetic and biological membranes is of importance in many areas. These include: medically-related processes, such as the transport of water and solutes through cartilage[1-3] and transdermal drug delivery;[4, 5] basic processes pertinent to cellular processes, such as transport across lipid monolayers[6-8] and bilayers[9-13]; and applications in fuel cell technology.[14-16]

In this chapter the use of laser scanning confocal microscopy (LSCM), coupled with constant volume flow rate-pressure measurements, is described as a new approach for visualising and quantifying the nature of fluid flow across porous materials. The methodology is general, but is illustrated with studies of flow across the porous material, dentine. Quantitative measurements of fluid flow rates across dentine are particularly important in the development and assessment of treatments for dentinal hypersensitivity which is a common problem in the

adult population. Dentine contains tubules, usually 1-2 μm in diameter at a density of *ca.* 1 x 10^6 – 1 x 10^7 cm^{-2},[17] which run between the pulp and enamel in the tooth structure. When the enamel erodes or gums recede, the tubules become exposed, providing pathways between the oral cavity and nerve fibres in the pulp. It has been shown *in-vivo* that a pressure gradient exists across dentine, which causes the outward flow of fluid.[18] This fluid flow increases in response to tactile, thermal and osmotic stimuli,[19] which is thought to result in a mechano-receptor response in the nerve fibres of the pulp, which is detected as pain.[20] Significantly, this outward fluid flow may result in a barrier to the inward diffusion of desensitising actives which are targeted at pulpal nerves.[21] Clearly, this has implications for the strategies used to treat dentinal hypersensitivity.

A number of techniques have been employed for the measurement of dentinal fluid flow rates *in-vitro*, on feline,[22] canine,[23] bovine[24] and human[25, 26] teeth. However, these techniques are limited to the determination of permeability across bulk dentine by either hydraulic conductance methods or bulk radiation measurements, which can only provide the mean flow rate for the entire sample studied. More recently, scanning electrochemical microscopy (SECM) has been employed to image the rate of fluid flow through porous solids,[27, 28] with a resolution governed by the size of the probe electrode used (typically in the range 2 – 25 μm). In optimal circumstances, SECM is thus capable of resolving flow through a single tubule.

As described in Chapter 3, in the SECM approach, local fluid flow rates and the topography of dentine slices have been sequentially mapped *in-situ* by

monitoring the transport-limited current for the electrolysis of a target mediator at an ultramicroelectrode (UME) probe, as a function of position in the plane above the surface. These measurements employ a two-compartment cell, with each side separated by a slice of dentine and containing a target analyte at the same concentration. In the absence of an applied fluid pressure, the current response depends only on the tip-substrate separation, thereby revealing topographical information. By re-imaging the same area with an applied pressure, local regions of fluid flow are identified as an enhancement in the tip current due to convective flow through the membrane. With permeability maps obtained in this way, studies can then be extended to examine the effect of fluid flow blocking agents.[29] A key outcome of the prior SECM studies was the acknowledged importance of making high spatial resolution measurements, in line with other work[30, 31] which has demonstrated that tubules in dentine show a range of structures, and hence, by implication, may be characterised by different fluid flow rates and different responses to treatment.

Although SECM is a powerful technique, the general lack of feedback control to accurately regulate the distance between the tip and the substrate means the area imaged and electrode sizes employed are limited in order to avoid tip crash. Moreover, there are strict demands on the flatness of the sample studied. Most importantly, SECM is characterised by rather lengthy imaging times, severely limiting the time-resolution of the technique in imaging applications,[32] although this can be improved through the use of multi-electrode probes.[33]

In this chapter laser scanning confocal microscopy (LSCM) is introduced as a new complementary approach for imaging flow across porous materials, supported by a simple method for measuring hydraulic permeability. In LSCM, a laser provides a point source of illumination and fluorescent light emitted from this spot is focused to a point and passed through a pinhole for detection at a photomultiplier. In this way the pinhole rejects light that would obscure the image, *i.e.* light reflected by areas of the sample above and below the plane of interest. By scanning the light position, it is possible to build up a three dimensional fluorescence image of the substrate of interest. The spatial resolution of the technique is ultimately governed by the wavelength of laser used, and is thus comparable to the best achievable with SECM.[34] As a rule of thumb, images typically take only a few seconds to acquire, in contrast to SECM which takes tens of minutes, although this obviously depends upon the number of pixels recorded in the image, and the signal-to-noise requirements.

In this chapter it is shown that LSCM can be used to identify and assess heterogeneities in fluid flow through dentine, *in-vitro*, through the use of an experimental set up that is generally applicable to imaging of transport across membranes. We are unaware of any previous studies aimed at quantitatively visualising flow, although the use of LSCM for the fluorescence imaging of static porous structures has been reported previously. For example, the morphologies of microporous membranes have been elucidated, without the need for staining.[35] Fluorescent labelling of sieve elements and liposomes, respectively, has been utilised in order to visualise transport processes through sieve tubes and skin.[36, 37] Microcrack networks in granite have also been explored

using fluorescent resin impregnation.[38] Penetration of an antibiotic into a biofilm has been compared to its transport across a transwell using LSCM.[39] The structure of monolithic silica columns used for chromatography has been visualised,[40] and the mixing efficiency of macroporous polymer plugs in microfluidic devices has been investigated.[41] The studies described herein develop these approaches to the dynamic visualisation of fluid flow, together with a simple hydraulic permeability measurement which allows quantification of the flow process.

4.2   Experimental Details

Preparation of the dentine sample is described in section 2.1.2. For initial *z*-stack imaging experiments, the dentine disc was dipped into a solution containing either Fluorescein or Rhodamine B at a concentration of 10 µM prior to imaging. The excess solution was removed from the surface with a tissue, and the dentine sample placed onto a glass microscope slide ready for imaging. The experimental setup employed for LSCM experiments involving fluid flow is detailed in section 2.3.5. The procedure for time series imaging of Rhodamine B flow through dentine, and the effect of treatments on this flow, was as follows: LSCM images were acquired for five groups of four dentine samples. Each group was treated in one of five ways: (1) untreated dentine; (2) dentine brushed with a wet brush (KerrHawe) to simulate standard brushing without any additive; (3) dentine with a commercial varnish applied (Cervitec®, Ivoclar-Vivadent); (4) dentine brushed with a placebo toothpaste; and (5) dentine brushed with a toothpaste containing alginate gel as a candidate active for dentinal hypersensitivity. A fresh dentine sample was used for each type of experiment. In each case, the syringe pump

(KD Scientific 100) was switched on, at a flow rate of 3ml/hr, concomitantly with the image acquisition software. Visualisation was carried out in this way to ensure that regions of active flow could be identified clearly; excessive periods could result in a wash-out of the observed effects. The flow rate of 3ml/hr led to the development of trans-dentine pressure which encompassed that measured *in-vivo* and led to higher pressures to provide a challenge to the various treatments considered. Pressure-time data were measured simultaneously via a digital differential pressure sensor, built in-house.

4.3   Results and Discussion

The results of the LSCM experiments to investigate fluid flow are discussed herein.

4.3.1   Results and Discussion: *Z*-Stack Imaging of Dentinal Tubules

In order to obtain sub-surface information on tubule structure it was necessary to fill the tubules with a fluorescent probe. This was achieved by dipping the dentine disc into a solution of the fluorophore. Fluorescein was the first probe employed; however, this was found to be unsuitable as dentine autofluoresces at the same wavelength as λ_{ex} for fluorescein (488 nm). The second fluorophore trialled was Rhodamine B. Rhodamine B was found to be an effective fluorophore for imaging tubules as there was no autofluorescence of the dentine at 543 nm (λ_{ex} for Rhodamine B). Figure 4.01 shows images of dentine obtained using each of these dyes.
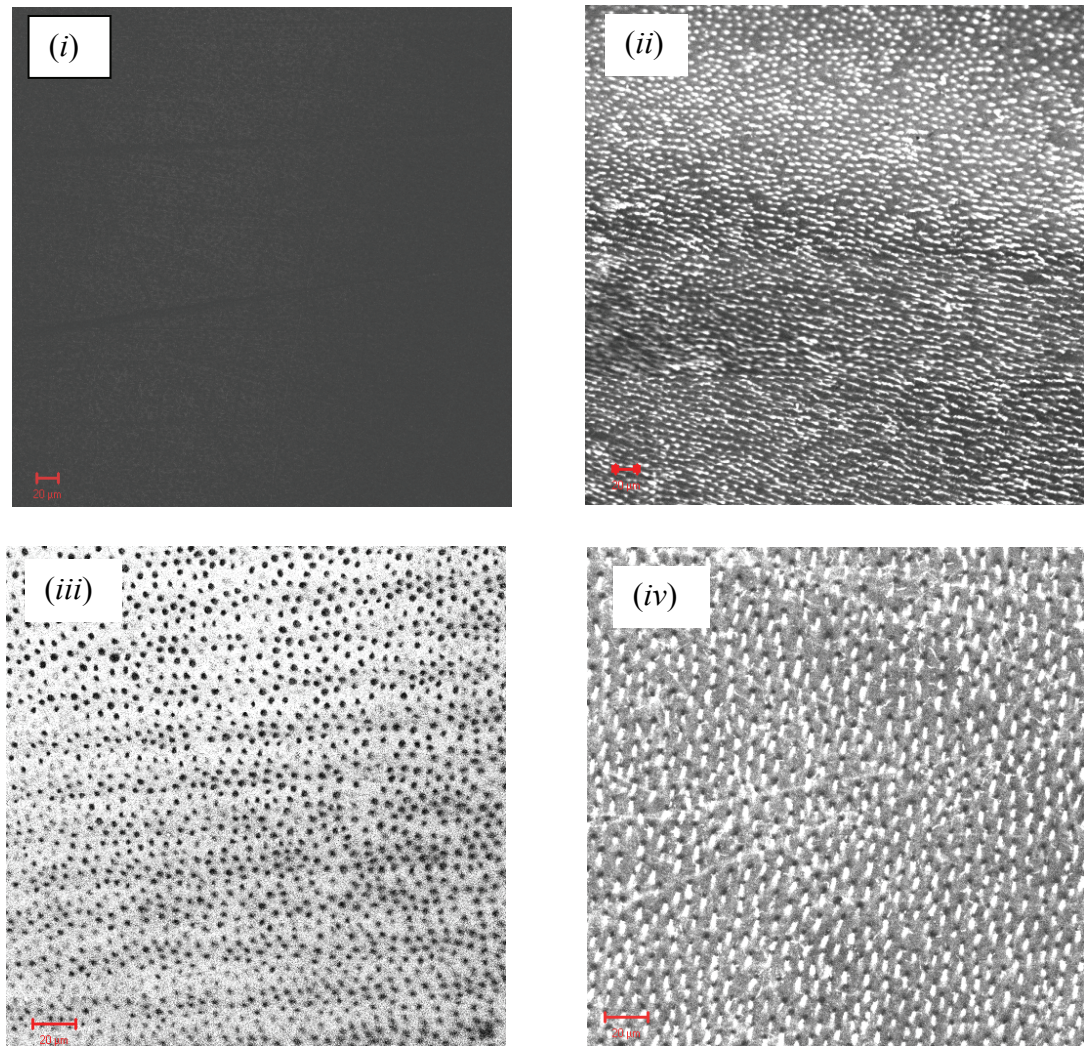
Figure 4.01: LSCM images of human dentine at (*i*) an excitation wavelength (λ_{ex}) of 543 nm. Note there is very little autofluorescence of dentine. (*ii*) On dipping the dentine into 10 μM Rhodamine B solution, the tubules become visible. (*iii*) At λ_{ex} = 488 nm (i.e. λ_{ex} for fluorescein), dentine was seen to autofluoresce. (*iv*) On dipping the dentine into 10 μM fluorescein solution, the tubules become less apparent as it becomes more difficult to differentiate between them and the dentine background. The scale bar represents 20 μm in all images.

As a result of these preliminary experiments, Rhodamine B was used in all subsequent LSCM experiments on dentine.

LSCM has the capacity to build up a 3D image of the sample, known as a *z*-stack. A series of images are taken through the sample in the *z* direction. The software then combines these images to form a three-dimensional image. At a wavelength of 543 nm it was possible to obtain a *z*-stack of the dentinal tubules, as shown in Figure 4.02. By taking an orthogonal section in the *x* axis the morphology of the dentinal tubules was revealed. They all appear to have similar diameters over the 20 μm *z*-stack. In Figure 4.02 the main image, outlined in blue, was taken in the *xy* plane. The two images outlined in red and green were sections in the *xz* and *yz* planes, respectively.
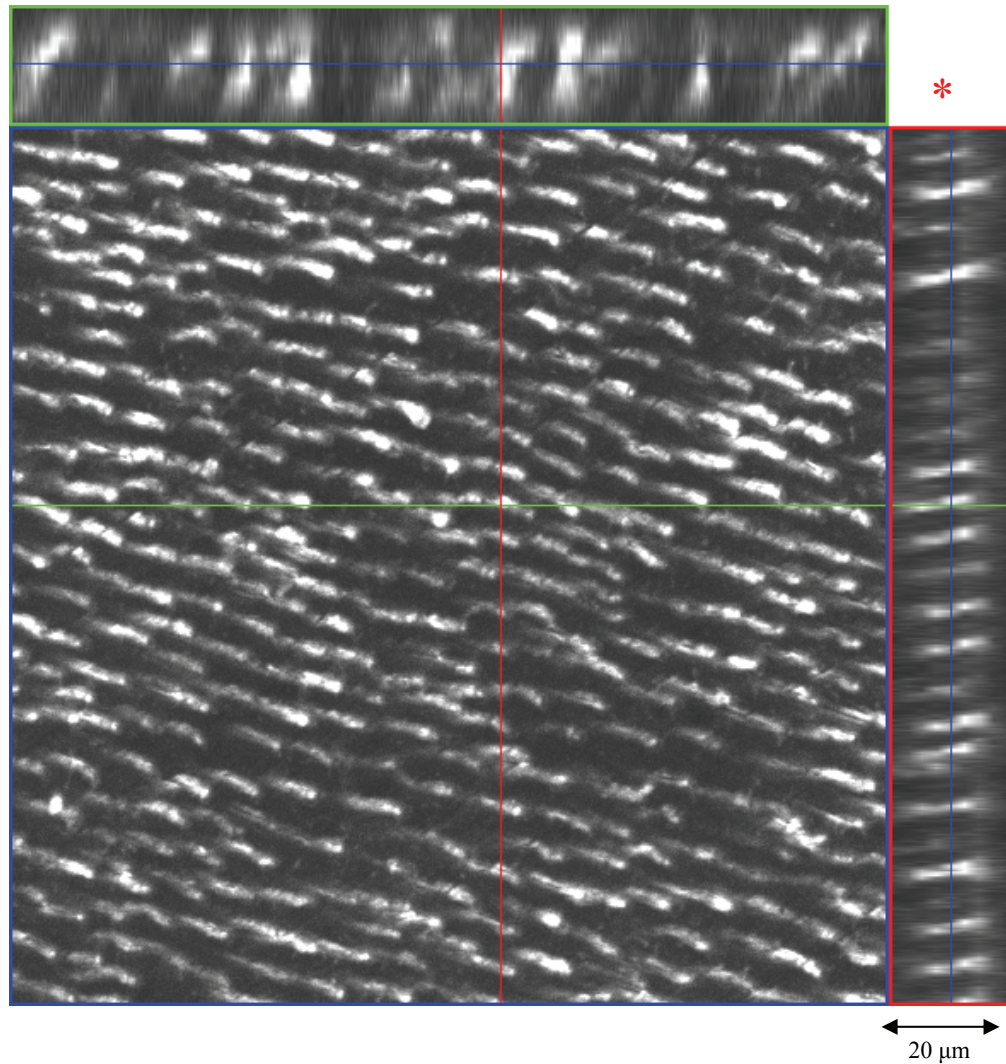
Figure 4.02: Z-stack at 543 nm of human dentine. A section in the x-axis (*) shows the tubules are all of a similar diameter over the 20 μm stack

114

The *xz* section, labelled with an asterisk, shows that the tubules were all of similar diameter across the 20 μm *z*-stack recorded. However, it is of note that the whole sample was 100 μm in thickness, and so the tubule diameters may not have been constant throughout the entire sample.

4.3.2 Results and Discussion: Time Series Imaging of the Flow of Rhodamine B through Dentine, and the Effect of Treatments on this Flow

Figure 4.03 shows a typical series of images, recorded just at the outer dentine surface, over a time series of 120 s for untreated, brushed dentine (procedure 2). The images were obtained just after flow commenced.
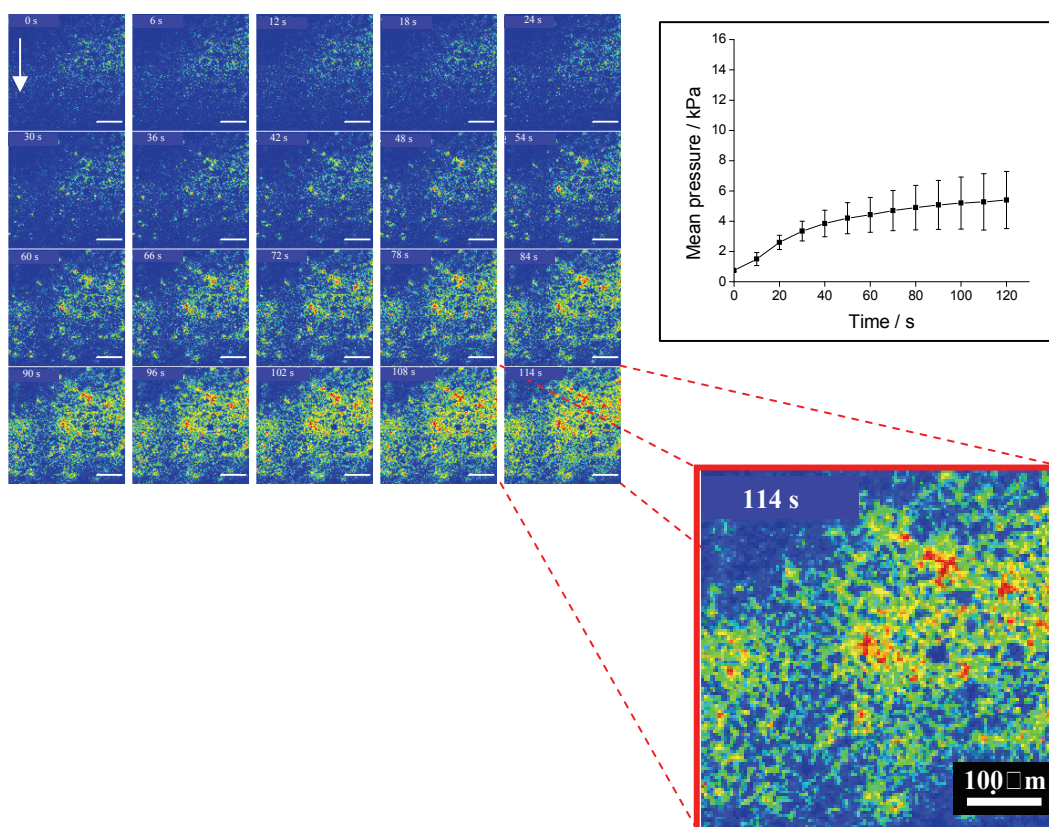
Figure 4.03: A selection of LSCM images marking the flow of rhodamine B through dentinal tubules for brushed dentine. Blue regions indicate low fluorescence; red regions represent high fluorescence. Image acquisition was started concurrently with the flow. The time indicated in the corner of each frame refers to the time at which that frame began to be recorded (~6 s image duration). The scan direction is indicated by the arrow. Images were recorded continuously in the plane parallel to, and just above, the substrate surface over a time period of 2 minutes. Each frame shows a region 460 μm x 460 μm, and the scale bar denotes 100 μm. Inset: Pressure-time data obtained during the imaging measurement (average of 4 runs).

With time, the extent of fluorescence increases, which is evidence that Rhodamine B is transported through the sample. However it is also evident that the transport process is spatially heterogeneous. Some areas of the sample are highly fluorescent and these areas increase in fluorescence, whereas other areas remain dark. The imaging technique is able to probe these heterogeneities in mass transport at the microscale. The pressure-time data shown as an inset to

116

Figure 4.03 shows that the pressure gradually increases with time, which is evidence that there is an impediment to flow at this volume flow rate. Thus the pressure-time measurement provides information which complements the visualisation.

The sensitivity of the pressure-time data in identifying the ease with which flow occurs can be seen clearly in Figure 4.04.
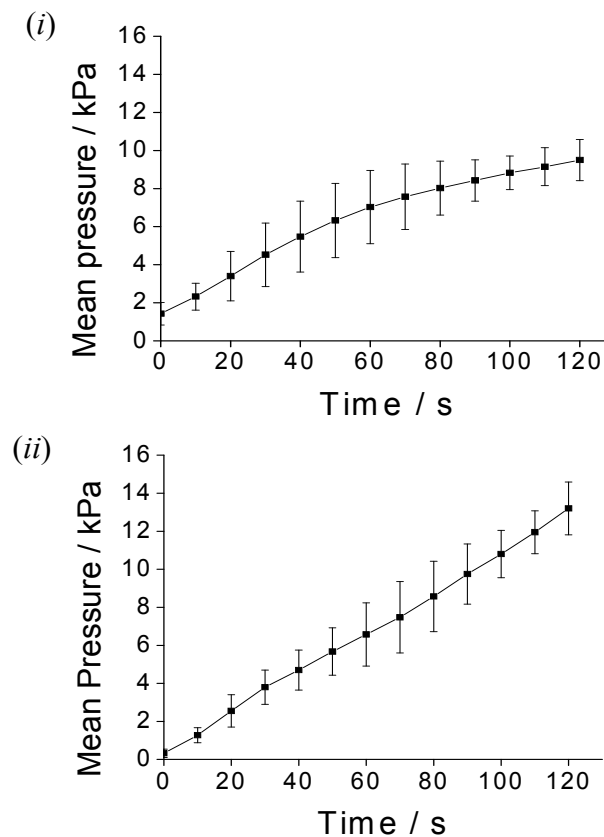
Figure 4.04: Pressure-time data obtained during fluid flow through human dentine, etched in 10% citric acid, after: (*i*) no further treatment; (*ii*) treatment with a commercial varnish (Cervitec®). Each plot shows the mean pressure observed for 4 fresh dentine samples.

This shows the measurements for (*i*) dentine after no treatment; and (*ii*) after treatment with a commercial varnish. It can be seen that the pressure rises steeply with time in the latter case which is because the varnish provides an effective

barrier to flow. This can be seen in Figure 4.05 which compares an optical image of an etched dentine sample (*i*) before and (*ii*) after treatment with the commercial varnish.
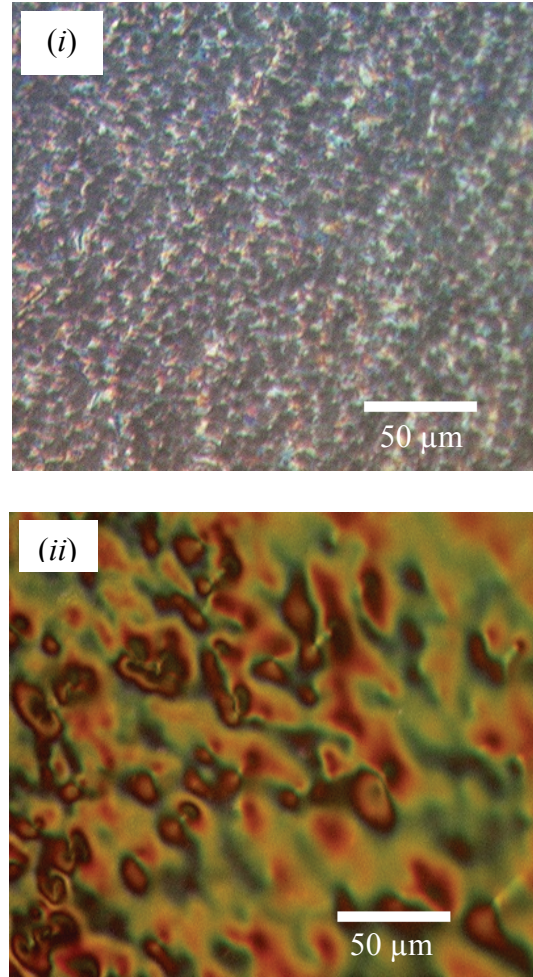
Figure 4.05: Optical DIC micrographs of: (*i*) untreated dentine; and (*ii*) dentine treated with a commercial varnish (Cervitec®) at a magnification of x200.

It is apparent that the varnish grossly covers the dentine surface after treatment, occluding the tubules which are visible in (*i*). Thus, as the syringe in the pump compresses the system, the pressure rises steeply. Interestingly, the pressure increase for dentine after no treatment (Figure 4.04(*i*)) is larger than for brushing with no paste (inset to Figure 4.03) which suggests that brushing removes some

debris and clears some tubules which are (partially) blocked after the preparation stage.

A significant aspect of these experiments was to assess a new active for dentinal tubules which can be included in a paste. To this end, dentine samples were then treated with an alginate paste. As introduced in Chapter 1.1.4, alginate is a naturally occurring polysaccharide which reacts in the presence of divalent cations, especially Ca^{2+}, to form a robust gel.[42] Thus, it was expected that a gel would form in the presence of the 1 mM $CaCl_2$ which was included in both the donor and receptor solutions and is typical of the Ca^{2+} levels found in saliva.[43] Figure 4.06 shows fluorescence images recorded over the final 66 s of a 120 s time period for brushed dentine treated with the alginate paste.
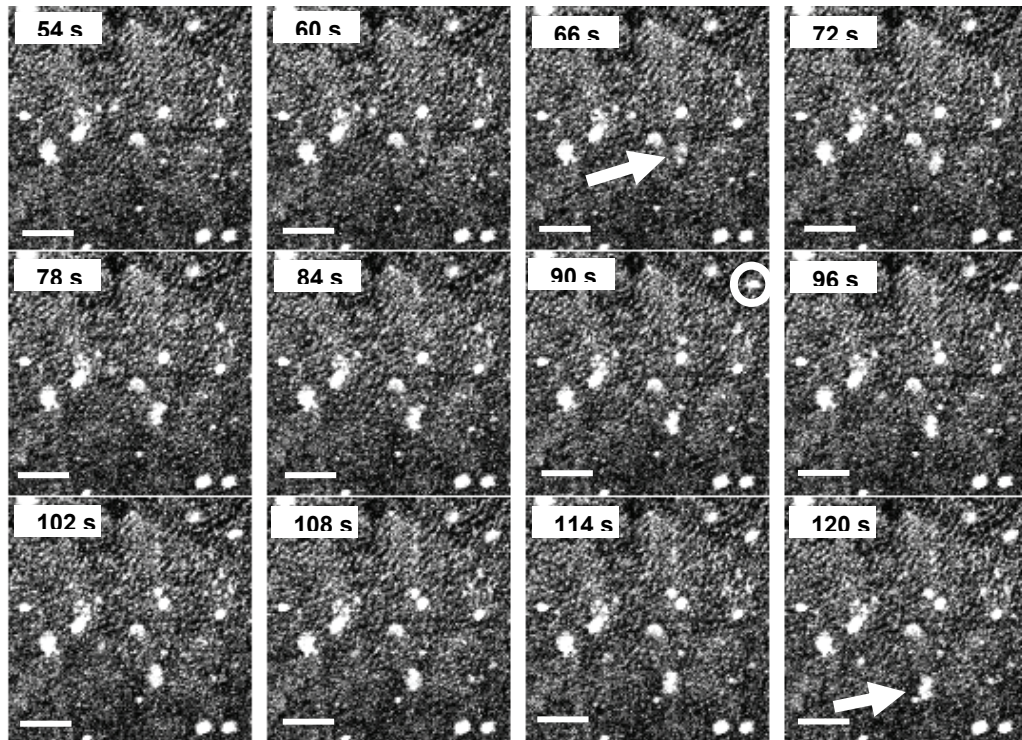
Figure 4.06: A selection of LSCM images showing the flow of rhodamine B through dentinal tubules for dentine treated with alginate paste. Black regions indicate low fluorescence; white regions represent high fluorescence. The scan was started concurrently with the flow. The time indicated in the corner of each frame refers to the time at which that frame began to be recorded. The scan direction is the same as for Fig. 2. Images were continuously recorded in the plane parallel to the substrate surface over a time period of 2 min. Each frame shows a region 460 × 460 μm. Scale bar: 100 μm. See text for description of processes occurring.

Figure 4.06 shows fluorescence images over the final 66 s of this period for brushed dentine treated with the alginate paste. From Fig. 4.07, the pressure–time data over 120 s for dentine brushed with alginate paste, it can be seen that the mean pressure increases significantly above the value for brushed dentine (inset, Fig. 4.03), clearly showing that treatment with the paste impeded the flow process across the sample.
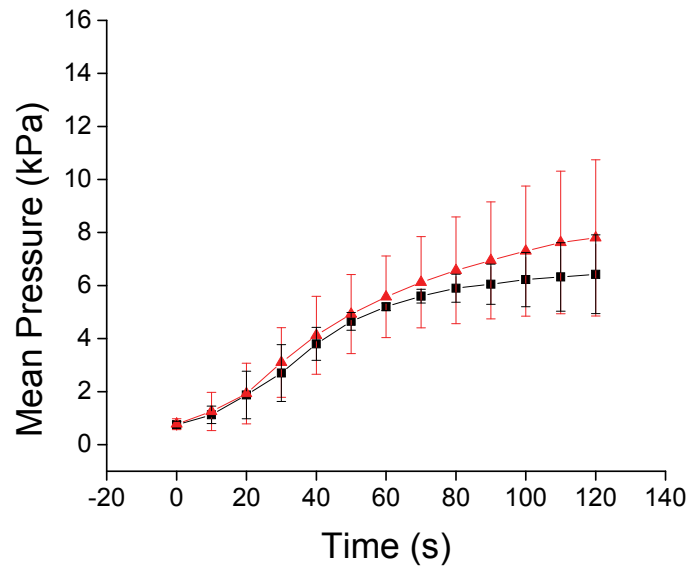
Figure 4.07: Black squares: Pressure–time data obtained during fluid flow through human

dentine, etched in 10% citric acid, after brushing with a placebo paste. The plot shows the mean

pressure observed for 4 fresh human dentine samples. Red triangles: Pressure–time data for fluid

flow through human dentine, etched in 10% citric acid, and then brushed with alginate paste

average of 4 data sets). The error bars for the alginate data are larger.

The mechanism by which this occurs can be seen in the time series images (Fig.

4.06). The treatment leads to partial occlusion of the surface by deposited

particles, most likely silica, which fluoresce and appear bright. These have

dimensions of *ca.* 30 – 40 µm. There is an increase in the spatially heterogeneous

fluorescence, which is attributed to the transport of Rhodamine B across the

sample, but this is clearly impeded by the blocking method. Occasionally the

flow is such that a particle can be dislodged. For example, a particle (indicated

by the arrow in the third frame (t = 66 s)) appeared in the frame after apparently

being expelled from tubules. It then travelled across the frame (see for example

the new arrow position in frame 12 (t = 120 s)). Another fragment appeared in

the frame halfway through this series of images, and is indicated within the

circle. This particle sat on the surface of the dentine throughout the remainder of the time series. The pressure–time data obtained for the placebo paste (procedure 4), which did not contain alginate, are also shown in Fig. 4.07. The pressure increases significantly compared to simple brushing (inset to Fig. 4.03), indicating that the paste occludes tubules, but the rise in pressure is not as great as for the alginate paste. Thus, the alginate paste acts to provide a more robust blocking effect.

The measurements at constant volume flow rate allowed the hydraulic permeability of the dentine, L_p, to be calculated: [44]

$$L_p = \frac{V_f}{SP} \tag{4.01}$$

where V_f is the volume flow rate (μl min^{-1}), S is the area of the sample (cm^2) and P is the driving pressure across the dentine (cm H_2O). For untreated, unbrushed dentine, the pressure increases with time and quickly reaches a steady state value of 9.5 kPa (95 cm H_2O). The corresponding L_p value is 10.64 μl min^{-1} cm^{-2} cm H_2O. For brushed dentine, the L_p value is calculated to be 18.71 μl min^{-1} cm^{-2} cm H_2O. For the alginate and placebo treatments, the L_p values are 12.96 and 15.67 μl min^{-1} cm^{-2} cm H_2O respectively. In the case of the commercial varnish, the pressure does not reach a steady state and the pressure increases linearly with time. In this case a hydraulic permeability cannot be calculated because the sample is essentially impermeable to flow.

4.4   Conclusions

LSCM has been shown to be a sensitive means of visualising fluid flow through dentine over relatively large areas, and for evaluating the effect of surface treatments on flow. The capacity of the technique for capturing time series is of particular use for observing the dynamic action of certain treatments. By combining the fluorescence data with pressure–time data, it is possible to elucidate further information about the system in question. This enhanced understanding of the nature of fluid flow and of the effect of occlusion agents on this flow will be valuable in the development of more effective treatments for dentinal hypersensitivity. The new technique is versatile and has the capacity to be applied to other areas concerned with the flow of fluid through a substrate or membrane. The studies herein have shown that brushing the dentine caused higher levels of fluorescence over the time period of the experiment, hence it may be concluded that brushing the dentine allows more facile flow, by opening up tubules that may have remained occluded after acid etching. The pressure–time data obtained lends further support: there was a much smaller increase in pressure for brushed dentine than for unbrushed dentine over a 120 s experimental period. In contrast, the commercial varnish (Cervitec®) occluded the vast majority of the tubules, as evidenced by the fluorescence data (which showed no flow) and pressure–time data recorded for these samples. The placebo paste and alginate paste both occluded the tubules to a certain extent, but under pressures in excess of 6 kPa, material deposited on the surface to occlude flow was expelled from the dentine into the receptor solution. It should be noted that the natural pressure across dentine in the oral cavity is estimated to be *ca.* 2 kPa19 and so these pastes are likely to withstand this. The alginate paste resulted

in a larger increase in pressure than the placebo paste, and thus alginate appears

to be a successful candidate for the treatment of dentinal hypersensitivity.

4.5　References

(1)　M. Gonsalves, J.V. Macpherson, D. O'Hare, C.P. WInlove *Biochim. Biophys. Acta - Gen. Subj.* **2000**, *1524*, 66.

(2)　M. Gonsalves, A.L. Barker, J.V. Macpherson, P.R. Unwin, D. O'Hare, C.P. Winlove *Biophys. J.* **2000**, *78*, 1578.

(3)　J.V. Macpherson, D. O'Hare, P.R. Unwin, C.P. Winlove *Biophys. J.* **1997**, *73*, 2771.

(4)　E.R. Scott, A.I. Laplaze, H.S. White, J.B. Phipps *Pharm. Res.* **1993**, *10*, 1699.

(5)　B.D. Bath, R.D. Lee, H.S. White, E.R. Scott *Anal. Chem.* **1998**, *70*, 1047.

(6)　I. Ciani, D.P. Burt, S. Daniele, P.R. Unwin *J. Phys. Chem. B* **2004**, *108*, 3801.

(7)　J. Zhang, C.J. Slevin, C. Morton, P. Scott, D.J. Walton, P.R. Unwin *J. Phys. Chem. B* **2001**, *105*, 11120.

(8)　C.J. Slevin, S. Ryley, D.J. Walton, P.R. Unwin *Langmuir* **1998**, *14*, 5331.

(9)　M. Tsionsky, J. Zhou, S. Amemiya, F-R F. Fan, A.J. Bard, R.A.W. Dryfe *Anal. Chem.* **1999**, *71*, 4300.

(10)　M.A. Edwards, S. Martin, A.L. Whitworth, J.V. Macpherson, P.R. Unwin *Physiol. Meas.* **2006**, *27*, R63.

(11)　T. Matsue, H. Shiku, H. Yamada, I. Uchida *J. Phys. Chem.* **1994**, *98*, 11001.

(12)　V. Yu. Evtodienko, O.N. Kovbasnjuk, Y.N. Antonenko, L.U. Yaguzhinsky *Biochim. Biophys. Acta* **1996**, *1281*, 245.

(13)　H. Yamada, H. Shiku, T. Matsue, I. Uchida *J. Phys. Chem.* **1993**, *97*, 9547.

(14)   T. Kallio, C. Slevin, G. Sundholm, P. Holmlund, K. Kontturi
Electrochem. Comm. **2003**, *5*, 561.

(15)   T. Okada, N. Nakamura, M. Yuasa, I. Sekine *J. Electrochem. Soc.* **1997**, *144*, 2744.

(16)   J.R.P. Jayakody, S.H. Cheung, L. Durantino, H. Zhang, L. Xiao, B.C. Benicewicz, S.G. Greenbaum *J. Electrochem. Soc.* **2007**, *154*, B242.

(17)   J.V. Macpherson, P.R. Unwin *Electroanalysis* **2005**, *17*, 197-204.

(18)   B. Ciucchi, S. Bouillaguet, J. Holz, D. Pashley *J. Endodont.* **1995**, *21*, 191.

(19)   D. Pashley *Archs. Oral Biol.* **1994**, *39 (supp.)*, 73S.

(20)   M. Addy, G. Embery, W.M. Edgar, R. Orchardson In *Tooth Wear and Sensitivity: Clinical Advances in Restorative Dentistry*; Taylor & Francis: London, 2000, pp 239.

(21)   D.H. Pashley, W.G. Matthews *Archs. Oral Biol.* **1993**, *38*, 577.

(22)   N. Vongsavan, B. Matthews *Archs. Oral Biol.* **1991**, *36*, 641.

(23)   D.H. Pashley, T. Kehl, E. Pashley, P. Palmer *J. Dent. Res.* **1981**, *60*, 763.

(24)   J. Tagami, L. Tao, D.H. Pashley, J.A. Horner *Archs. Oral Biol.* **1989**, *34*, 773.

(25)   D.H. Pashley, H.J. Andringa, G.D. Derkson, S.R. Kalathoor *Archs. Oral Biol.* **1987**, *32*, 519.

(26)   D.H. Pashley, W.G. Matthews, Y. Zhang, M. Johnson *Archs. Oral Biol.* **1997**, *41*, 1065.

(27)   J.V. Macpherson, M.A Beeston, P.R. Unwin, N.P. Hughes, D. Littlewood *J. Chem. Soc., Faraday Trans.* **1995**, *91*, 1407.

(28)   S. Nugues, G. Denuault *J. Electroanal. Chem.* **1996**, *408*, 125.

(29) J.V. Macpherson, M.A. Beeston, P.R. Unwin, N.P. Hughes *Langmuir* **1995**, *11*, 3959.

(30) G. R. Holland *J. Membr. Sci.* **1997**, *39 (supp)*, 3S.

(31) R. Schilke, J.A. Lisson, O. Bauß, W. Geurtsen *Archs. Oral Biol.* **2000**, *45*, 355.

(32) A.L.Colley, C.G. Williams, U. D'Haenens Johansson, M.E Newton, P.R.Unwin, N.R. Wilson, J.V. Macpherson *Anal. Chem.* **2006**, *78*, 2539.

(33) A.L. Barker, P.R. Unwin, J.W. Gardner, H. Reiley *Electrochem. Comm.* **2004**, *6*, 91.

(34) C.J.R. Sheppard, D.M. Shotton *Confocal Laser Scanning Microscopy*; Bios Scientific Publishers: Oxford, 1997.

(35) C. Charcosset, J.C. Bernengo *J. Membr. Sci.* **2000**, *168*, 53.

(36) M. Knoblauch, A.J.E. van Bel *The Plant Cell* **1998**, *10*, 35.

(37) D.D. Verma, S. Verma, G. Blume, A. Fahr *Int. J. Pharm.* **2003**, *258*, 141.

(38) C.T. Onishi, I. Shimizu *J. Struct. Geol.* **2005**, *27*, 2268.

(39) K.K. Jefferson, D.A. Goldmann, G.B. Pier *Antimicrob. Agents Chemother.* **2005**, *49*, 2467.

(40) M. Motokawaa, H. Kobayashia, N. Ishizukab, H. Minakuchib, K. Nakanshic, H. Jinnaia, K. Hosoyaa, T. Ikegamia, N. Tanaka *J. Chromatog. A* **2002**, *961*, 53.

(41) H.M. Simms, C.M. Brotherton, B.T. Good, R.H. Davis, K.S. Anseth, C.N. Bowman *Lab Chip* **2005**, *5*, 151.

(42) I. Braccini, S. Pérez *Biomacromolecules* **2001**, *2*, 1089.

(43) J.J. Vogel, R. Naujoks, F. Brudevold *Archs. Oral Biol.* **1965**, *10*, 523.

(44) A.R. Özok, M.-K. Wu, P.R. Wesselink *J. Dent.* **2002**, *30*, 107.

Chapter 5

Localised Dissolution of Enamel

To complement the studies into dentinal hypersensitivity, microscopic dissolution of bovine enamel was investigated. This chapter describes a novel approach, based on SECM, to promote the localised dissolution of bovine enamel, effected by the application of a proton flux to the enamel surface from a UME positioned within 5 μm of the surface, in aqueous solution. The approach results in a well-defined "acid challenge" yielding well-defined etch pits that were characterised using light microscopy and white light interferometry. The effect of etching in the presence of lactate was considered, as was the effect of treating the enamel samples with sodium fluoride prior to etching. The approach described is amenable to mass transport modelling, allowing quantitative interpretation of etch features.

5.1   Introduction

The 20th century brought many advances in dentistry and oral healthcare. As a result, people now retain their teeth for a longer period of time. Consequently, a new problem has arisen; these longer-lasting, healthier teeth now show increased wear over time. This is generally considered to be due to acid erosion, which is strongly linked to the consumption of acidic food and drinks. Contact with acid temporarily softens the enamel. This is usually countered by the action of saliva, which contains calcium and thus remineralises the enamel. However, if a further

acid challenge is then presented to the enamel, there is not sufficient time for this remineralisation to occur. This compromised enamel is then likely to suffer wear due to the abrasive effect of brushing. If left untreated, tooth wear can lead to the loss of tooth shape and colour, and to dentinal hypersensitivity.

Much research has been carried out to investigate the acid erosion of dental enamel.[1-9] Typically, these studies have involved subjecting slices of enamel to a collection of acid challenges, ranging in pH from 2.3 to 6.3. Many subsequent studies have considered the effect of inhibitory substances and treatments on the dissolution of enamel.[10-15] Most relevant to this thesis are those which investigated the role of fluoride in inhibiting the dissolution of dental enamel.[16-22] Fluoride is thought to incorporate into the enamel and increase the hardness and resistance to erosion of the material. This incorporation may involve loosely or firmly bound fluoride, and the extent to which the fluoride penetrates the enamel is a subject of much discussion.[23-26] The action of fluoride against enamel dissolution is due to the shift in the dissolution equilibrium in its presence.[4] It is important to note that much of the past work described has involved acid challenges where mass transport is not particularly well-defined. This makes the quantitative analysis of etch features rather difficult. In contrast, the work described herein is underpinned by well-defined mass transport models making quantitative analysis possible.

5.2 Experimental

In order to carry out the localised dissolution experiments, the electrochemical cell was set up in a similar manner to that described in Chapter 2.1.2. However,

there was no hole in the base of the PTFE cell, and the enamel sample was secured to this base using double-sided sticky tape. The enamel samples were first polished flat using 600 grit Carbimet polishing paper (Buehler, Coventry, UK), followed by 4000 grit silicon carbide paper (Buehler) before attaching to the cell base. The cell was filled with a 0.2 M solution of KNO_3, with pH 6.3. A 25 μm diameter Pt UME, fabricated as described in Chapter 2, was initially positioned approximately 5 mm above the enamel surface. A silver wire coated with AgCl was utilised as the reference electrode. A CV was run between 0.0 V and -1.0 V in order to cause the reduction of oxygen, as described in Equation 5.01:

$$O_2 + 2H_2O + 4e^- \rightarrow 4OH^-$$
5.01

The bulk limiting current, i_∞, was observed at a potential of approximately -0.8 V. The electrode was held at this potential and an SECM approach curve (hindered diffusion characteristic) was measured as described in Chapter 3. This allowed the UME to be positioned at a defined distance of 10 μm from the enamel surface, using the piezeoelectric positioner.

In order to facilitate localised dissolution of the enamel substrate, a current of 50 nA was applied galvanostatically to the working electrode for between 5 minutes and 40 minutes. This caused the oxidation of water, thus producing a proton flux from the electrode to the enamel surface, which induced the dissolution of the substrate. Previous work using laser scanning confocal microscopy has shown that this process is well-defined and quantitative, such that the current is directly

proportional to the flux of protons produced.[27] A schematic of the process used here is shown in Figure 5.01. Between etchings, the UME was translated laterally by 250 μm.
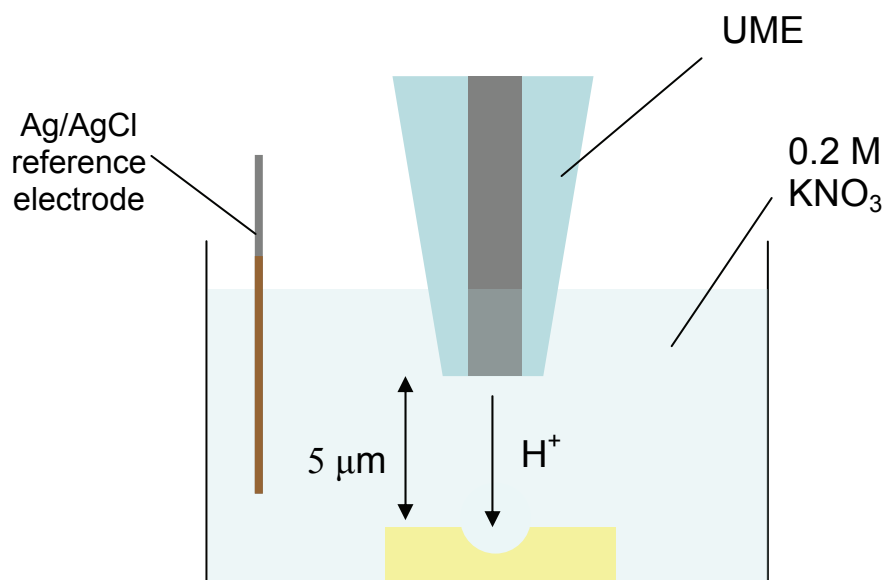
Figure 5.01: A schematic showing the localised dissolution process.

The etched enamel samples were coated in a thin layer of gold (in the order of 1 nm) prior to white light interferometry (WLI) measurements being carried out. This increased the reflectance of the surface to allow the optimum WLI measurements to be obtained.

5.3   Results and Discussion: Analysis of the Etch Pits

The etch pits created in the local dissolution experiments were analysed using optical microscopy, white light interferometry (Wyko NT-2000) and AFM. A typical set of pits visualised by optical microscopy is shown in Figure 5.02.
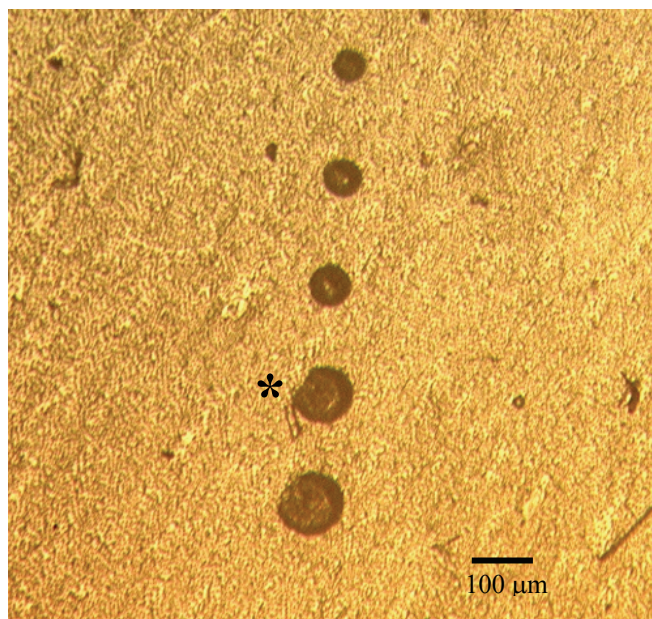
Figure 5.02: An optical micrograph showing a series of etch pits separated by 250 μm centre-to-centre. Scale bar represents 100 μm.

The etch pits shown in Figure 5.02 were clearly seen to increase in diameter as the etch times increased. The pit that formed after etching for 30 minutes (marked with an asterisk in Figure 5.02) was not perfectly circular. This may have been due to either debris or a scratch on the surface that altered the dissolution kinetics of that region of the enamel.

The images obtained using WLI allowed the diameter and depth of the pits to be elucidated with high precision. A typical WLI image is shown in Figure 5.03, along with analysis of an *x*-cross section of one pit and *y*-cross sections of two pits.

132
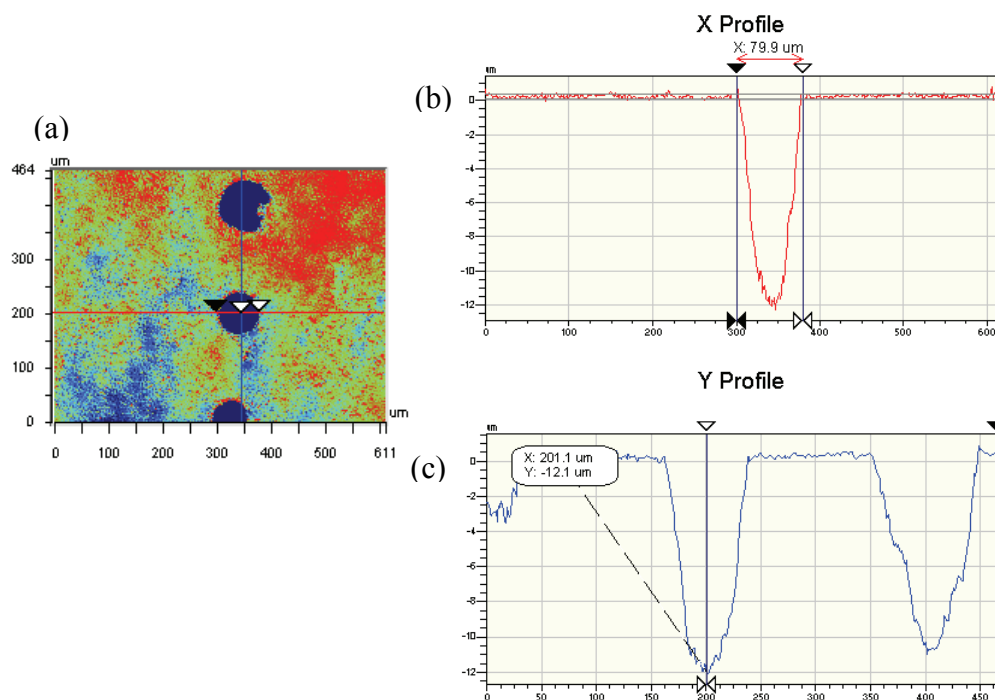
Figure 5.03: A typical set of interferometry images showing (a) a 2D view of the surface, (b) the diameter of the pit, and (c) the depth of the pit.

The etch pits were easily identifiable in the WLI image. The etch pits increased in depth and diameter as the etch time increased. With the exception of the pit metioned previously, all etch pits were found to have a circular opening, and were all approximately conical. This approximation was used to provide an acceptable estimate of the pit volume, using the pit diameter and depth. In order to determine the quantity of material lost during the dissolution process, the volume of the pit (ie the volume of material lost during dissolution) was calculated and multiplied by the density of the bovine enamel (2.9×10^{-6} g cm^{-3}) to give a mass (or number of moles) of material lost. The assumption is made that hydroxyapatite is the overwhelming component of enamel.

The etch pit diameter was seen to increase with increasing experiment time, as shown in Figure 5.04.
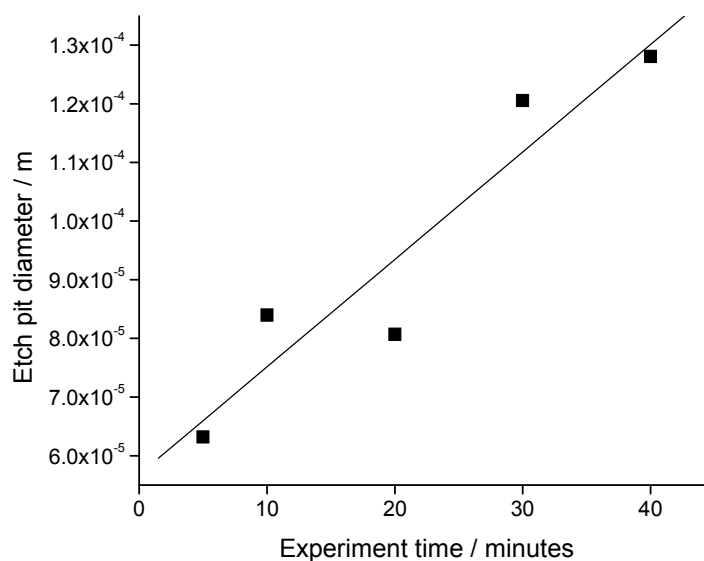
Figure 5.04: Plot showing the change in etch pit diameter with increasing experiment time. The etch solution contained 0.1 M KNO_3 only. Etching was achieved by applying a constant current of 50 nA.

It is clear that there is a reasonable linear fit to the data, with a correlation coefficient of 0.8928. A plot of the etch pit depth with etching time shows an increase in pit depth although the correlation coefficient is poor (0.6516), as shown in Figure 5.05. Note that the data for the etch pit formed after 20 minutes was disregarded as an outlier.
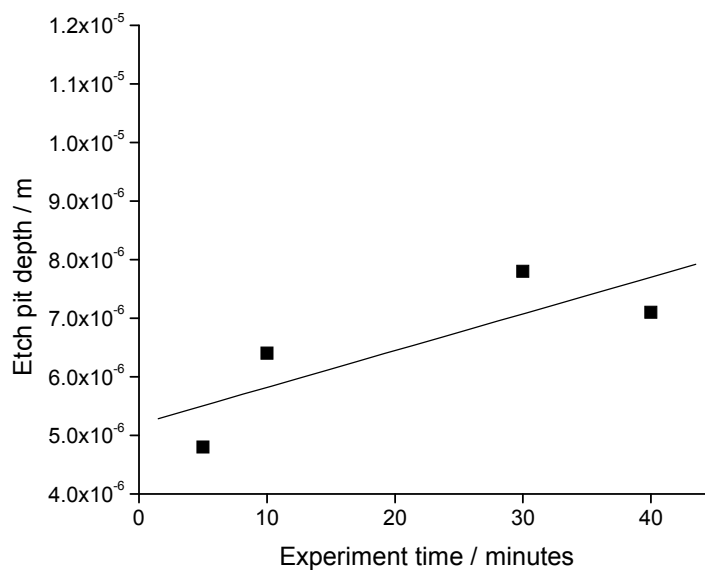
Figure 5.05: Plot of the etch pit depth with etching time. The etch solution contained 0.1 M

KNO$_3$ only. Etching was achieved by applying a constant current of 50 nA.

However, if the pit volume, which relates to the amount of material lost, is calculated and plotted, a much more linear fit is seen with increasing etching time, as shown in Figure 5.06.
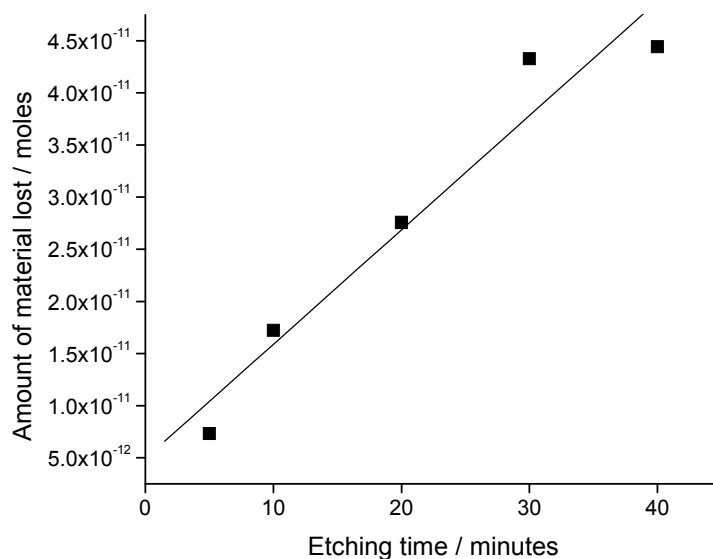
Figure 5.06: Plot showing the amount of material lost with increasing experiment time. The etch solution contained 0.1 M KNO_3 only. Etching was achieved by applying a constant current of 50 nA.

To further investigate the dissolution process, 50 mM sodium L-lactate was added into the solution in the cell. The effect of adding this is shown schematically in Figure 5.07. In short, the lactate acts as a buffer in the solution, sequestering a certain amount of the protons produced at the UME to form lactic acid.[28] The pKa value of lactic acid is 3.86 at 298 K and so it buffers at a pH of approximately this value.
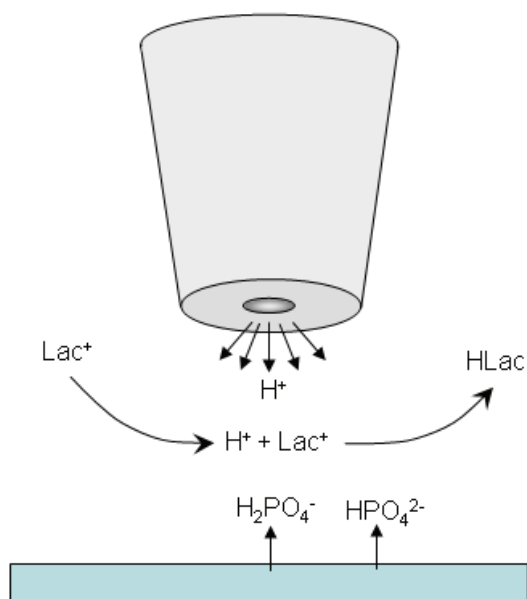
Figure 5.07: Schematic of the main processes arising from a localised proton challenge to the

enamel surface in the presence of sodium L-lactate at a concentration of 50 mM.

Figure 5.08 compares the pit volume characteristic for a current of 50 nA in the

presence and absence of sodium L-lactate at a concentration of 50 mM in the

etch solution.
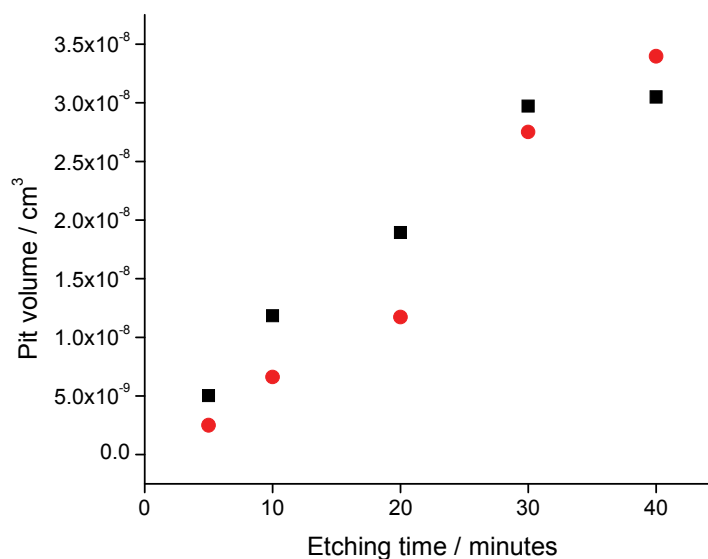
Figure 5.08: Plot showing the increase in pit volume with increasing etching time, in the absence (black squares) and presence (red circles) of 50 mM sodium L-lactate.

This plot reveals that the etch pits that developed in the presence of sodium lactate had a smaller volume (except for the pits that formed after 40 minutes, where the trend is reversed). This was as expected, as some of the protons formed at the UME were lost to the lactate to form lactic acid.

As discussed in the introduction to this chapter, fluoride has long been touted as an effective inhibitor of acid erosion, and as such the effect of treating the enamel with 1000 ppm NaF prior to etching was investigated. This was achieved by immersing the enamel sample in the NaF solution for 5 minutes and then rinsing thoroughly with deionised water. Figure 5.09 shows the effect of the NaF treatment on the formation of the etch pit volumes for an acid challenge generated by applying a constant current of 50 nA.
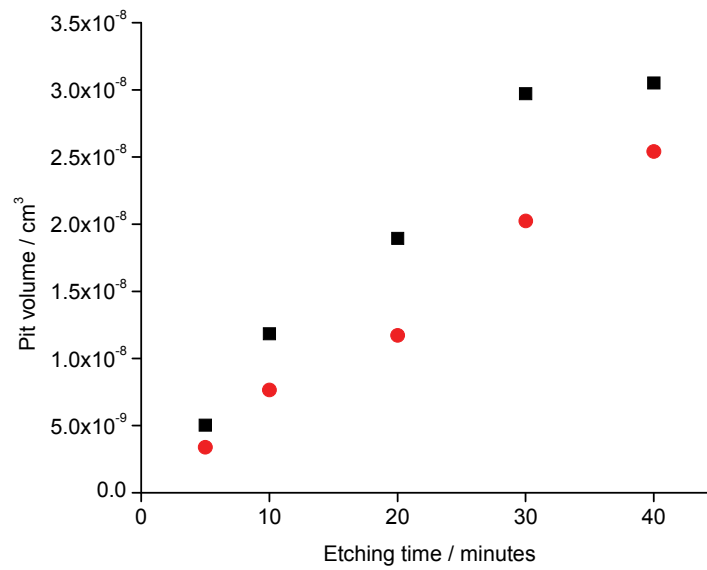
Figure 5.09: The effect of NaF treatment on etch pit development, as a function of etch time. The black squares represent the volume of the pits formed in the absence of NaF, while the red circles show the volumes for a surface treated with NaF.

It is clear from the plot that treating the enamel surface with sodium fluoride resulted in a smaller pit volume compared to the etch pits formed without sodium fluoride enamel surface treatment. Upon further inspection of the data, it was found that the pit diameters formed on fluoride-treated enamel were smaller than those formed on untreated enamel. This was true at all experimental timescales, except at etch times > 30 minutes, where pits were of similar depth on treated and untreated enamel. This may be because fluoride incorporated into the enamel during the treatment process is released at these longer timescales.

5.4   Simulations

Some preliminary work was carried out using the finite element method to simulate the formation of localised etch pits. The simulation domain is shown in Figure 5.10. The boundary conditions are listed in Table 5.01.
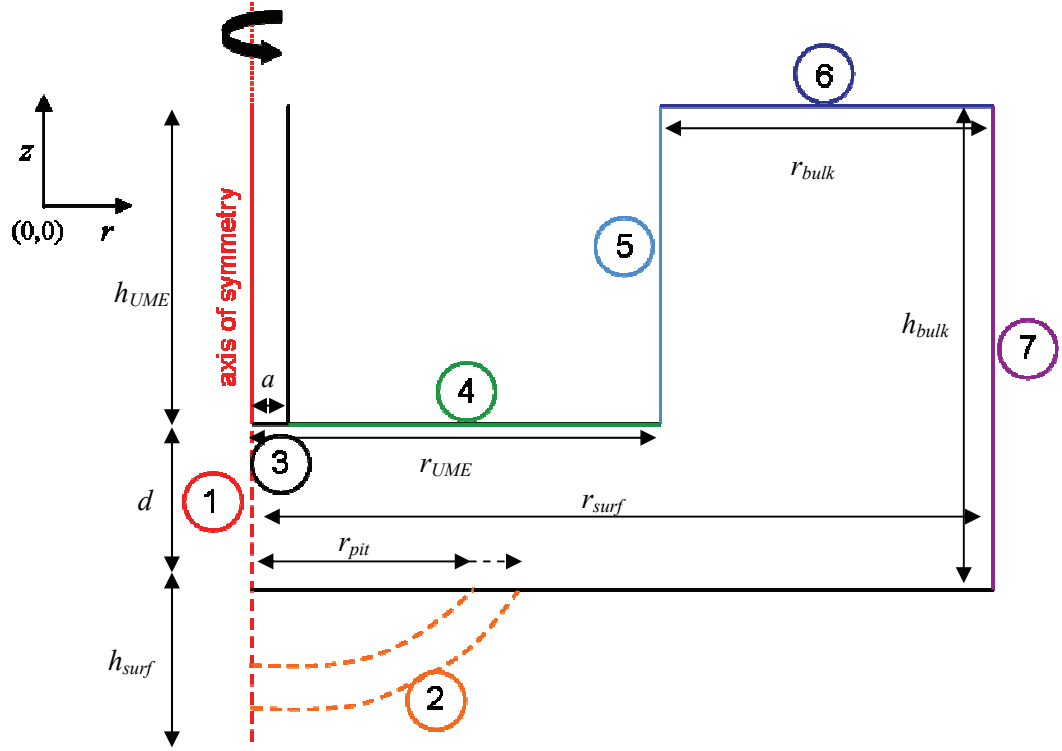
Figure 5.10: Simulation domain for the axisymmetric cylindrical geometry used to model the

formation of etch pits in dental enamel.

The equation solved on the interior of the domain illustrated in Figure 3 is the

time-dependent reaction diffusion equation cast in axisymmetric coordinates (eq

5.01):

$$\frac{\partial C_i}{\partial t} = D_i \nabla^2 C_i + R_i \qquad 5.01$$

Where i is the species under consideration (H^+, $H_nPO_4^{3-n}$), and R is the net

production of species i via equilibrium reactions (ie amount of i produced –

amount of i used up).

Boundary Description	Number in Figure 5.10	Coordinates	Equation
Axis of symmetry (fixed in r but free in z)	1	$r=0$ $(h_{surf}+d+h_{UME})>z>0$	$0 = \nabla C \cdot \underline{n}$
Solution/enamel interface (moving)	2	$r = r_{pit}$ $z = h_{surf}$	**For H$^+$:** $kC_{H^+} = D_{H^+}\nabla C_{H^+} \cdot \underline{n}$ **For H$_2$PO$_4$$^-$:** $k\frac{6}{8}C_{H^+} = -D_{H_2PO_4^-}\nabla C_{H_2PO_4}$ **For HPO$_4$$^{2-}$ and H$_3$PO$_4$:** $0 = \nabla C \cdot \underline{n}$
Solution/active electrode interface (fixed)	3	$r=a$ $z = h_{surf} + d$	**For H$^+$:** $D_{H^+}\frac{\partial C_{H^+}}{\partial z} = \frac{i}{F \cdot area}$ **For H$_n$PO$_4$$^{3-n}$:** $0 = \nabla C_i \cdot \underline{n}$
Solution/insulator interface (fixed)	4 & 5	$r = r_{UME}$ **For 4**: $z = h_{surf} + d$ **For 5**: $z = h_{surf} + d + h_{UME}$	$0 = \nabla C_i \cdot \underline{n}$
Bulk solution (fixed)	6	$r = r_{surf}$ $z = h_{surf} + d + h_{UME}$	**For H$^+$:** $C^{H+} = 10^{-pHbulk}$ **For H$_n$PO$_4$$^{3-n}$:** $C_i = 0$
Bulk solution (fixed in r but free in z)	7	$r = r_{surf}$ $z = h_{surf} + d + h_{UME}$	**For H$^+$:** $C^{H+} = 10^{-pHbulk}$ **For H$_n$PO$_4$$^{3-n}$:** $C_i = 0$

Table 5.01: Boundary conditions for finite element modelling.

In Table 5.01, the geometric quantities h_{surf}, d, h_{UME}, r_{UME}, a, r_{pit}, and r_{surf} represent the height of the surface, the UME-surface separation, the height of the UME, the radius of the active UME microwire, the radius of the etch pit and the radius of the surface respectively. Boundaries 6 and 7 were set at a sufficient distance form the region of interest so as to obtain a good solution.

Figure 5.11 shows a typical plot of experimental data obtained in the absence of sodium lactate and sodium fluoride, alongside simulated data. A high rate constant of 0.3 cm s^{-1} was found to fit the data which is close to the diffusion-controlled limit under the conditions of these experiments. Thus the etching process is characterised by rapid surface kinetics.
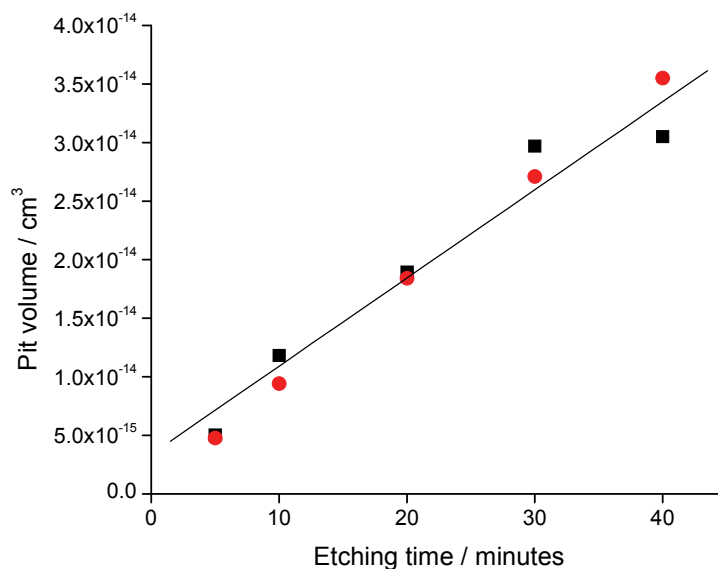
Figure 5.11: Plot showing experimental (black squares) and simulated (red circles) pit volumes in an etching solution containing only 0.1 M KNO$_3$. A rate constant of 0.3 cm s^{-1} was applied in the simulations.

A close fit is seen between the simulated and experimental data. This is promising for future experiments in this field. A more complete treatment of the

data would include an analysis of pit shape morphology and this might reveal anisotropic rates in the dissolution process.

5.5   Conclusions

Localised dissolution of dental enamel has been achieved by the application of a proton flux to the enamel surface from a UME positioned in close proximity to the enamel, in aqueous solution. The etch pits characteristic of this approach may be analysed using optical microscopy, white light interferometry and other techniques. Measurements can give information on the nature of the dissolution of the enamel, and the effect of inhibitors, such as fluoride, on this dissolution. It has been shown that fluoride causes changes in the morphology of the etch pits that form. Preliminary simulations reveal that the etching process in a solution of 0.1 M KNO_3 occurs at a diffusion-limited rate.

5.6   References

(1)   M.E. Barbour, D.M. Parker, G.C. Allen, K.D. Jandt *Eur. J. Oral Sci.* **2003**, *111*, 428.

(2)   M.E. Barbour, D.M. Parker, K.D. Jandt *J. Colloid and Interfacial Sci.* **2003**, *265*, 9.

(3)   M.E. Barbour, D.M. Parker, G.C. Allen, K.D. Jandt *Eur. J. Oral Sci.* **2003**, *111*, 258.

(4)   M. Finke, K.D. Jandt, D.M. Parker *J. Colloid and Interfacial Sci.* **2000**, *232*, 156.

(5)   J.L. Fox, W.I. Higuchi, M. Fawzi, R.C. Hwu, J.J. Hefferren *J. Dent. Res.* **1974**, *53*, 939.

(6)   R.P. Shellis *Archs. Oral Biol.* **1996**, *41*, 473.

(7)   L. Wang, R. Tang, T. Bonstein, C.A. Orme, P.J. Bush, G.H. Nancollas *J. Phys. Chem. B* **2005**, *109*, 999.

(8)   W. White, G.H. Nancollas *J. Dent. Res.* **1977**, *56*, 524.

(9)   W.D. White, G.H. Nancollas *J. Dent. Res.* **1980**, *59*, 1180.

(10)   T. Attin, K. Meyer, E. Hellwig, W. Buchalla, A.M. Lennon *Archs. Oral Biol.* **2003**, *48*, 753.

(11)   M.G. Dedhiya, F. Young, W.I. Higuchi *J. Dent. Res.* **1973**, *52*.

(12)   M.S. Putt, C.J. Kleber *J. Dent. Res.* **1985**, *64*, 437.

(13)   L.K.A. Rodrigues, M. Nobre dos Santos, J.D.B. Featherstone *J. Dent. Res.* **2006**, *85*, 617.

(14)   T.J. Roseman, W.I. Higuchi, B. Hodes, J.J. Hefferren *J. Dent. Res.* **1969**, 509.

(15) A.Z. Abdullah, S.M. Strafford, S.J. Brooked, M.S. Duggal *J. Dent. Res.* **2006**, *85*, 1011.

(16) R.A.M. Exterkate, J.M. ten Cate *Eur. J. Oral Sci.* **2007**, *115*, 143.

(17) A. Kawasaki, T. Suge, K. Ishikawa, K. Ozaki, T. Matsuo, S. Ebisu *J. Mat. Sci.: Mat. In Med.* **2005**, *16*, 461.

(18) H. Luoma, P. Alakuijala, A. Korhonen, E. Savolainen, J. Räisänen *Archs. Oral Biol.* **1994**, *39*, 177.

(19) S.A. Mundorff, M.F. Little, B.G. Bibby *J. Dent. Res.* **1972**, *51*, 1567.

(20) B.M. Shrestha, S.A. Mundorff, B.G. Bibby *J. Dent. Res.* **1972**, 1561.

(21) H. van Rijkom, J. Ruben, A. Vieira, M.C. Huysmans, G.-J. Truin, J. Mulder *Eur. J. Oral Sci.* **2003**, *111*, 253.

(22) H. Yamazaki, A. Litman, H.C. Margolis *Archs. Oral Biol.* **2007**, *52*, 110.

(23) T. Attin, R. Grieme, F. Paque, C. Hannig, W. Buchalla, R. Attin *Archs. Oral Biol.* **2005**, *50*, 317.

(24) H. Duschner, H. Götz, B. Øgaard *Eur. J. Oral Sci.* **1997**, *105*, 466.

(25) M. Tanaka, E.C. Moreno, H.C. Margolis *Archs. Oral Biol.* **1993**, *38*, 863.

(26) J.M. ten Cate *Acta Odontol. Scand.* **1999**, *57*, 325.

(27) N.C. Rudd, S. Cannan, E. Bitziou, I. Ciani, A.L. Whitworth, P.R. Unwin *Anal. Chem.* **2005**, *77*, 6205.

(28) M.E. Barbour, R.P. Shellis *Phys. Med. Biol.* **2007**, *52*, 899.

Chapter 6

Carbon as an Electrode Material

In this chapter, the techniques developed throughout the thesis are applied to the investigation of two types of carbon electrodes: boron-doped diamond (BDD) and highly ordered pyrolytic graphite (HOPG). Heterogeneities in the electroactivity of these substrates are explored.

6.1   Introduction

The role of carbon in electrochemistry began in the nineteenth century, when carbon electrodes were first used in batteries. Artificial graphite was first produced by Acheson in 1896 and led to rapid growth in industrial electrochemical processes.[1] The use of carbon as an electrode material has flourished ever since, both in research and industry.

Carbon has many attributes that make it a desirable electrode material. It exhibits good thermal and electrical conductivities, low thermal expansion and high purity. Carbon electrodes exist in a large variety of forms, and each of these has its own unique characteristics. In the studies detailed herein, boron-doped diamond (BDD) and highly ordered pyrolytic graphite (HOPG) have been investigated. In this chapter each material is introduced in detail and results on each are presented.

146

6.2   **Boron-Doped Diamond (BDD)**

Boron-doped diamond (BDD) was first introduced as an electrode material by Pleskov in 1987.[2] A general introduction to the material may be found in section 1.6.1. Diamond has long been known to possess some of the most extreme physical properties known to man. It is the hardest known material and so has many applications in industry for grinding and polishing. However, the scarcity and cost of the natural material has limited its application in this field, thus a method of producing artificial diamond was sought. The first process to yield artificial diamond was the high-pressure high-temperature (HPHT) technique, which mimics the conditions under which natural diamond formed. The single crystal diamonds which are formed have found widespread application in industry; however their use is limited by their size (usually ranging from nanometres to millimetres). Chemical vapour deposition (CVD) methods, including microwave CVD, hot filament CVD, and plasma torch CVD, have been developed which allow controlled growth of diamond films and doping of the diamond. It is possible to grow two kinds of diamond via CVD methods; single-crystal and polycrystalline. Single-crystal diamond has a number of advantages over the polycrystalline form; it has no grain boundaries and thus no sp^2 carbon impurities, and also forms a nearly perfect flat surface.[3] However single-crystal diamond is notoriously difficult to grow and as such is highly expensive. Thus polycrystalline diamond is most commonly encountered, and is the topic of the experiments described herein. Polycrystalline diamond arises due to the manner of the growth process. In the CVD technique, diamond growth begins when carbon atoms nucleate onto the surface of the growth substrate in such an arrangement as to initiate an sp^3 tetrahedral lattice. Once this has

occurred, growth proceeds in three dimensions until the individual diamond crystals coalesce, forming a continuous diamond film. After this point, the only direction in which growth may proceed is upwards, causing the film to thicken. This resulting film is polycrystalline with many grain boundaries and defects.[4] It exhibits a columnar structure which extends perpendicularly from the substrate. As the film grows and becomes thicker, the grain sizes increase and consequently the number of grain boundaries decreases.

One of the characteristics of intrinsic diamond is its superlative resistivity, greater than 2×10^{15} Ω cm. Clearly this is a barrier to the use of intrinsic diamond in electronic or electrochemical applications. However, doping with boron reduces its resistivity to less than 0.1 Ω cm. This opens up the opportunity to use diamond as an electrode material. Doping is easily achievable by introducing a boron-containing gas into the CVD process gas mixture. In the experiments detailed in this chapter, spatial variations in the electrical and electrochemical behaviour of BDD microarray electrodes were investigated. A variety of methods have been reported for the fabrication of BDD microelectrode arrays, including (i) BDD disc electrodes insulated with a thin layer of silicon nitride, the thickness of which defines the depth of the resulting recessed electrodes; (ii) pillars of silicon which were covered first with a layer of BDD, followed by insulating polyimide, and then polished to reveal the BDD electrode; and (iii) recessed, rectangular BDD electrodes formed by the growth of BDD within silicon oxide pits on a silicon surface. The most recent development has seen the fabrication of all-diamond arrays comprising disc-shaped BDD electrodes (10 – 50 μm in diameter) within an insulating diamond matrix.[5, 6]

There are two significant advantages of this type of microarray. Firstly, the BDD electrodes are coplanar with the surrounding insulating matrix, this removing any recess considerations. Secondly, these arrays may be repeatedly cleaned using mechanical polishing techniques without affecting the structural integrity of the device. This greatly extends the lifetime of the electrodes.

The array in the experiments described herein were comprised of ~50 µm diameter BDD discs spaced by 250 µm, centre-to-centre, in an insulating intrinsic diamond support. The BDD discs were coplanar with the intrinsic diamond. Each BDD microdisc electrode was polycrystalline and thus consisted of a variety of grains. It has been well reported that boron uptake in diamond is dependent on the crystallographic growth surface, as well as on a number of growth reactor parameters.[7, 8] It is known that boron is more readily incorporated into (111) growth sectors than (100) sectors.[7-9] This was likely to have important consequences for the electrical and electrochemical behaviour of the electrodes and so a variety of techniques were employed to examine the microarrays.

6.3 BDD Microdisc Array: Experimental

This section describes the preparation processes and instrumentation used in studies of the BDD microdisc array.

6.3.1 Fabrication of the BDD Microdisc Array

The microdisc array was fabricated and supplied by Element Six Ltd. (Ascot, UK).[10] In brief, a highly boron-doped polycrystalline chemical vapour deposition (CVD) diamond layer was grown to a thickness greater than 500 µm in a

microwave plasma reactor by adding diborane to the methane and hydrogen source gases. The resultant sample had a bulk electrical resistance of ~0.75 Ω m. The growth side of the diamond was polished to a mirror finish. A mask was used to define the array pattern, and UV laser light was focused on the polished face of the BDD plate, ablating the diamond in all regions except those shielded by the mask. This resulted in an array of conical BDD pillars. The diamond was then cleaned in boiling sulphuric acid, rinsed in deionised water and dried in an oven. It was then placed back into the microwave CVD reactor and a layer of non-conducting diamond was grown over the BDD array. This was then polished back to expose the tops of the BDD pillars. This created a planar surface (roughness $\pm \leq 10$ nm) with a well-defined array comprising disc UMEs *ca.* 53 μm in diameter (for the sample studied in these experiments). These were separated centre-to-centre by a distance of 250 μm. The thickness of the array was 500 μm. A schematic of the fabrication process is shown in Figure 6.01.
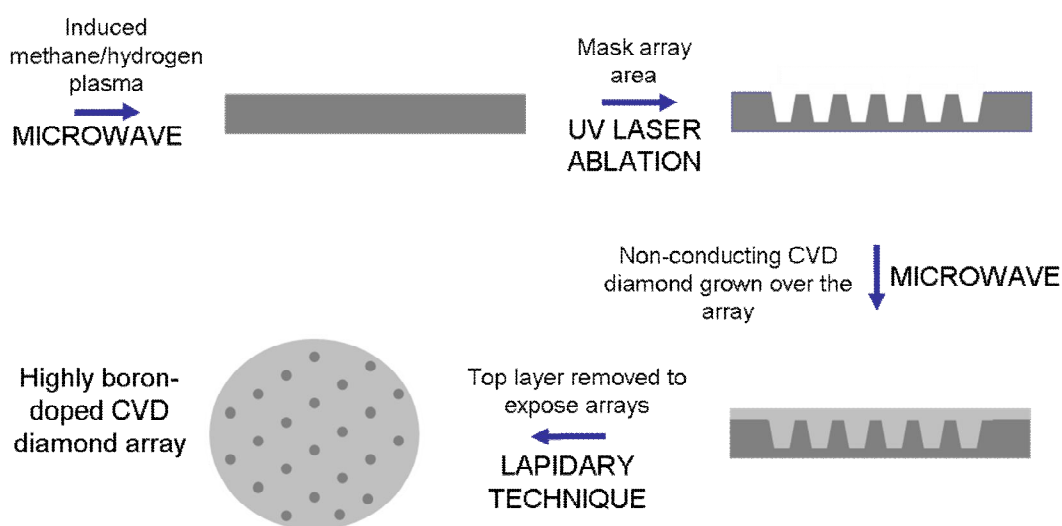
Figure 6.01: Schematic showing the fabrication process for the BDD microdisc array.

6.3.2 Acid Cleaning

Prior to experiments being carried out, the BDD microdisc array was acid cleaned in hot sulphuric acid that had been supersaturated with KNO_3. The solution was heated until just boiling and the KNO_3 had been exhausted (indicated by the fumes turning from brown to white). The solution was allowed to cool and the microdisc array was removed. It was then rinsed repeatedly with water before being immersed in concentrated sulphuric acid that had been heated until just boiling. This ensured that the diamond surface was oxygen terminated. After cooling, the sample was removed and again rinsed with water.

6.3.3 Electrical connection to the BDD Microdisc Array

A poor electrical connection to the BDD microdisc array may give misleading results. A reliable and robust ohmic connection was therefore required. This was achieved by using a sputtered Ti/Au contact (10 nm Ti/ 1 μm Au). Ti has the ability to form a carbide layer, and upon annealing it forms a carbide-based tunnelling contact.[11, 12] Electronic defect states are generated in the extremely thin TiC layer and also at the BDD/TiC interface, and this allows tunnelling of charge carriers through the contact. This lowers the contact resistance to less than 1 Ω cm. The thick Au layer acts as a highly conductive antioxidation layer. A glass disc was also sputtered with Ti/Au (in the same thicknesses as quoted above). The coated side of the BDD microdisc array was placed on the coated side of the glass disc and the whole assembly was placed in a tube furnace at 475 °C for 4 hours in order to anneal the contacts and carburise the Ti. Electrical wire was contacted to the Au coated disc using silver dag. Finally, the Au disc and

sides of the BDD microdisc array were electrically insulated using Araldite to allow use of the sample as a working electrode in electrochemical studies.

6.3.4 Conducting Atomic Force Microscopy (C-AFM)

The C-AFM experiments were carried out using a Veeco Multimode AFM with a Nanoscope IIIa controller and a Nanoscope E AFM equipped with a 120 μm x 120 μm J scanner (Digital Instruments, Santa Barbara, CA).The C-AFM probes utilised were fabricated by hand using platinum wire, as described previously[13] (note that in this case the probes were not insulated). These solid metal tips were used because conventional metal-coated AFM probes proved unsuitable; the extreme hardness of the diamond substrate caused the metal coating to wear away. The contact radius of the hand fabricated platinum probe used was 300 nm, elucidated using FE-SEM after C-AFM imaging, and thus represented a maximum value. During imaging, a bias voltage was applied to the tip from the AFM controller. The sample was connected to an external virtual earth current preamplifier. The output was fed into the AFM controller via a signal access module. A current-limiting resistor (10 or 100 MΩ) was placed in series with the sample. This protected the tip and sample from high currents. Current-voltage curves were recorded using a separate DAQ card (DT3016, Data Translations, for both analogue output and input) and software. The AFM was placed in a Faraday cage to reduce electrical noise.

6.3.5 Silver deposition

The BDD microdisc array was electroplated with silver to allow optical imaging of the individual array UMEs and to highlight spatial variations in the

electroactivity of the BDD UMEs. Deposition was achieved by applying a potential of -0.2 V (vs Ag/AgCl) from open circuit in a solution of 1 mM $AgNO_3$ and 0.2 M KNO_3. The array was held at this potential for periods of 2, 10 or 60 seconds and then rinsed with Milli-Q water before being imaged with the optical microscope or FE-SEM. The microdisc array was cleaned between depositions by holding at 0 V for *ca.* 1 minute to remove electrodeposited silver by anodic dissolution, and subsequent mechanical polishing with alumina on a moist pad.

6.3.6   Electrochemical Measurements

All electrochemical measurements were made at 22 ± 0.5 °C in a temperature-controlled room. Solutions were thoroughly deaerated with nitrogen before measurements were made. Solution composition for each experiment is described in section 6.4.

CV measurements on the BDD microdisc array were carried out using a three-electrode setup (CHI730A potentiostat, CH Instruments Inc.) controlled by a laptop computer. A platinum gause counter electrode was employed, with an Ag/AgCl reference electrode.

Initial SECM experiments were carried out using a 25 μm diameter Pt disc UME (fabrication described in section 2.2; RG = 10) as the tip. This allowed ready imaging of large areas with a reasonable tip-substrate separation while minimising the risk of tip crash. The SECM instrumentation is described in section 2.3.2. It was typically operated in substrate generation-tip collection (SG-TC) mode at a rate of 20 μm s^{-1} in a series of unidirectional linescans (line

separation 20 µm) with a scan size of 500 µm x 500 µm and a tip-substrate separation of *ca*. 10 µm. This distance was set by recording approach curves over an insulating region of the array and utilising the negative feedback response to determine the absolute tip-substrate separation.

High-resolution SG-TC SECM experiments were carried out using a 5 µm diameter Pt disc UME (RG = 35). The tip UME was scanned at fixed heights in the range *ca*. 0.5 – 1 µm above the surface. The height was determined by running an approach curve as described above. The larger RG value of the UME tip was accounted for by using the Comsol modelling program to simulate the negative feedback response. SG-TC was employed to map the (spatially heterogeneous) activity of individual electrodes in the BDD microdisc array. The tip was held at a potential to allow the diffusion –controlled detection of $Ru(NH_3)_6^{2+}$ (0.0 V vs Ag/AgCl), produced at the substrate, while the substrate potential was varied between apparent diffusion-controlled generation of $Ru(NH_3)_6^{2+}$ (-0.4 V vs Ag/AgCl) and a potential where there was minimal generation of $Ru(NH_3)_6^{2+}$ (-0.2 V vs Ag/AgCl). The UME tip was typically scanned at a rate of 5 µm s^{-1} in a series of unidirectional linescans (line separation 2 µm) with a scan size of 100 µm x 100 µm.

6.3.7 Fluorescence Laser Scanning Confocal Microscopy (LSCM)

Combined electrochemical-LSCM measurements were carried out in a solution containing 10 µM fluorescein with 0.2 M KNO_3 as the supporting electrolyte. The initial pH was adjusted to *ca* 4.7 by the addition of 0.1 M hydrochloric acid. Measurements were made in a cell comprising a PTFE base and glass cell body

which was positioned on the confocal microscope as described for the dentine setup in section 2.3.5. The BDD microdisc array substrate was secured flat in the base of the cell and the fluorescein solution added so that the substrate was fully immersed. All images were obtained using a water immersion objective lens (Seiss Achroplan 20×/0.50 W) with a 10 × tube lens. An argon laser (λ= 488 nm) was used in conjunction with a long-pass filter (λ = 505 nm). Images were typically acquired by scanning an area of 650 μm x 650 μm in the *xy* plane (parallel to the diamond surface) at particular intervals over a set time period to produce a time series. For LSCM imaging experiments, a potential of -1.4 V, with respect to the reference electrode, was applied to the BDD microdisc array in order to electrogenerate OH^-. This raised the pH locally and caused the fluorescein to fluoresce.

6.3.8   Photoluminescence Mapping

A DiamondView[14] deep-ultraviolet imaging instrument was used to record the visible photoluminescence maps of the BDD microdisc array. The substrate was held at room temperature, the luminescence excited by above band gap UV excitation, and the emitted light image recorded with a video camera. The luminescence from the high-purity intrinsic diamond originates primarily from dislocations. No visible luminescence was detected from the BDD UMEs.

6.4   BDD Microdisc Array: Results and Discussion

A photoluminescence (PL) map of the BDD microdisk array was recorded, as shown in Figure 6.02(*i*). The colour was inverted (compared to conventional PL images) using image analysis software. The BDD discs were clearly identifiable,

arranged in a hexagonal formation. It was also apparent that there were streaked regions of BDD toward the bottom left of the image. These resulted from the incomplete removal of BDD between the conical pillars during the laser ablation process (see Figure 6.01). If the final polish of the intrinsic diamond is not precisely parallel to the underlying structure, then these structures are revealed. This was an unusual processing error.
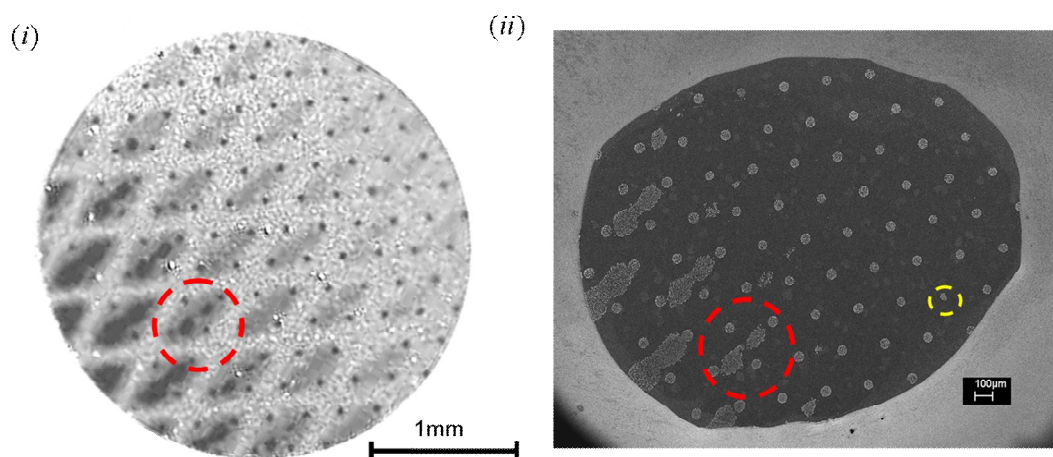
Figure 6.02: (*i*) is a photoluminescence (PL) image showing approximately 78 BDD microdisc electrodes. (*ii*) is a FE-SEM image of the same microdisc array after electrodeposition of silver from a solution containing 1 mM $AgNO_3$ in 0.2 M KNO_3. A deposition potential of -0.2 V (vs Ag/AgCl) was applied for 60 s.

In order to assess the electroactivity of the BDD microdisc array in a qualitative manner, silver was electrodeposited from a solution containing 1 mM $AgNO_3$ and 0.2 M KNO_3. The potential of the microdisc array was stepped from open circuit to -0.2 V vs Ag/AgCl. A FE-SEM image of a 60 second electrodeposition on the array is shown in Figure 6.02(*ii*). It was observed that electrodeposition had occurred on all the microdisc electrodes, and also on the streaked regions of BDD. The red circles in Figure 6.02 represent the same area of the sample. It can

be seen that approximately 78 microdisc electrodes are revealed. Only one of these is non-circular (as indicated in Figure 6.02(*ii*) with a small yellow circle), as demonstrated by the silver deposition experiments. The exposed area of the top surface of the sample is smaller in Figure 6.02(*ii*) than (*i*) due to the presence of the Araldite layer, added to insulate the sides and edges of the array device for all electrochemical experiments.

Cyclic voltammograms were recorded for the reduction of 10 mM $Ru(NH_3)_6^{3+}$ (in 0.1 M KCl) at the BDD microdisc array. Typical CVs are shown in Figure 6.03, at scan rates of 5, 10, 20, 50, and 100 mV s^{-1}. The CVs exhibited peaks at ~ -0.30 V on the forward scan and ~ -0.18 V on the reverse scan. These peaks were accentuated at faster scan rates.
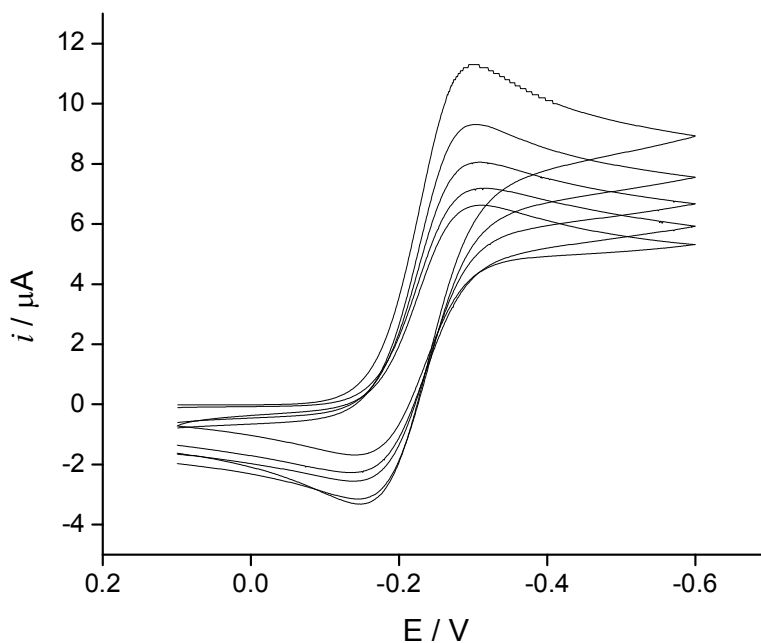
Figure 6.03: Cyclic voltammograms for the reduction of 10 mM $Ru(NH_3)_6^{3+}$ (in 0.1 M KCl) at the BDD microdisc array at scan rates of 5 (lowest peak current), 10, 20, 50 and 100 (highest peak current) mV s^{-1}.

Figure 6.04 shows CVs recorded at a lower concentration (0.1 mM). A similar response was observed, although at this lower concentration the effect of residual oxygen in the solution (even after thorough degassing) was more pronounced than for the 10 mM solution. The behaviour observed at both concentrations was as expected for the individual microdisc radii, centre-to-centre separations of the microdiscs, and the diffusional time scales probed.
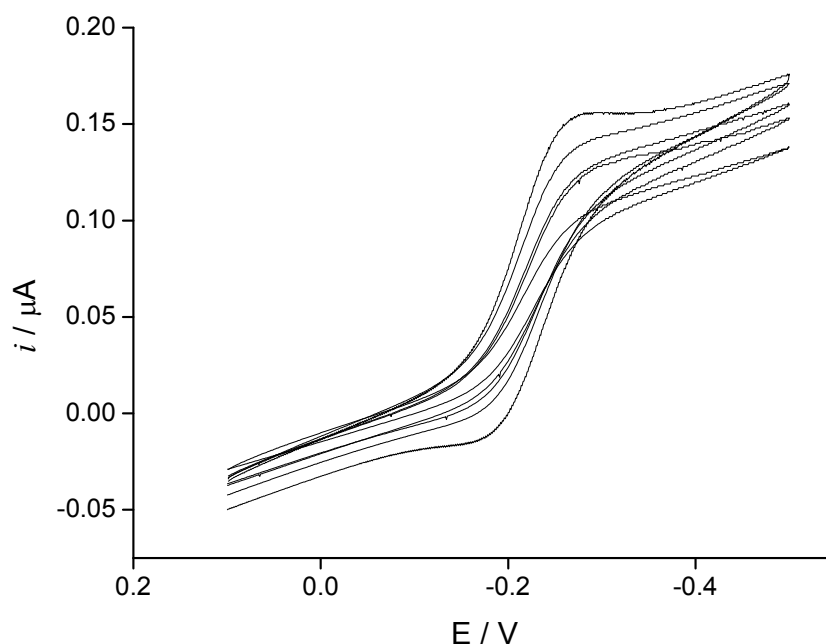
Figure 6.04: Cyclic voltammograms for the reduction of 0.1 mM $Ru(NH_3)_6^{3+}$ (in 0.1 M KCl) at the BDD microdisc array at scan rates of 5 (lowest peak current), 10, 20, 50 and 100 (highest peak current) mV s^{-1}.

A previous study of a similar BDD microdisc array fabricated by Element Six[6] showed that CVs demonstrated a scan rate dependence. This was ascribed to a degree of diffusional overlap between adjacent electrodes in the array. This was important for the studies detailed in this thesis; the defect regions present in Figure 6.02(*ii*) would also contribute to the electrochemical response.

The extent to which the BDD discs may be treated as uniformly active, metallic-like electrodes was of high importance. Applying equation 6.01, it was found that the steady-state diffusion-limited current that would flow at a 50 μm diameter metal electrode in a solution containing 10 mM $Ru(NH_3)_6^{3+}$ in 0.1 M KCl, assuming the diffusion coefficient for $Ru(NH_3)_6^{3+}$ is 8.8×10^{-6} cm^2 s^{-1},[15] is ~87 nA.

$$i_\infty = 4naFDC^*$$ (6.01)

It may be seen from Figure 6.03 that at the lowest scan rate, a limiting current of ~ 6.6 μA was measured. As mentioned above, it is an oversimplification of the mass transport situation to assume that the BDD discs are non-interacting. However, if this assumption is indeed made, the limiting current observed suggests 75 active electrodes. Note that this does not take the defect regions into account. This perhaps suggests that the BDD microdiscs (or regions within them) were sufficiently highly doped to be degenerate, i.e. to exhibit metallic-like characteristics. However, it is known that boron uptake is dependent on the crystal orientation of individual grains, and so it would be unwise to rely on bulk measurements such as CVs to prove this hypothesis. Thus, high-resolution imaging techniques were employed to elucidate spatial information on the electrical and electrochemical behaviour of individual BDD electrodes within the array.

Conducting Atomic Force Microscopy (C-AFM) was employed to probe the local electrical characteristics of the BDD microdisc array. A constant potential

was applied between the tip and substrate, and the current generated was measured with respect to the tip position. Thus detailed maps of the topography and conductivity of the substrate may be recorded. The lateral resolution of the technique was limited by the tip-surface contact area. Once regions of interest were identified, it was possible to position the tip in these areas and record *i-V* curves. This allowed the current-potential characteristics of individual grains in the BDD electrodes to be elucidated.

Figure 6.05 shows 80 µm × 80 µm C-AFM height, (*i*), and conductivity, (*ii*), images of a typical BDD electrode in the microdisc array. A potential of -2.5 V was applied to the tip, with a 10 MΩ current limiting resistor in series.
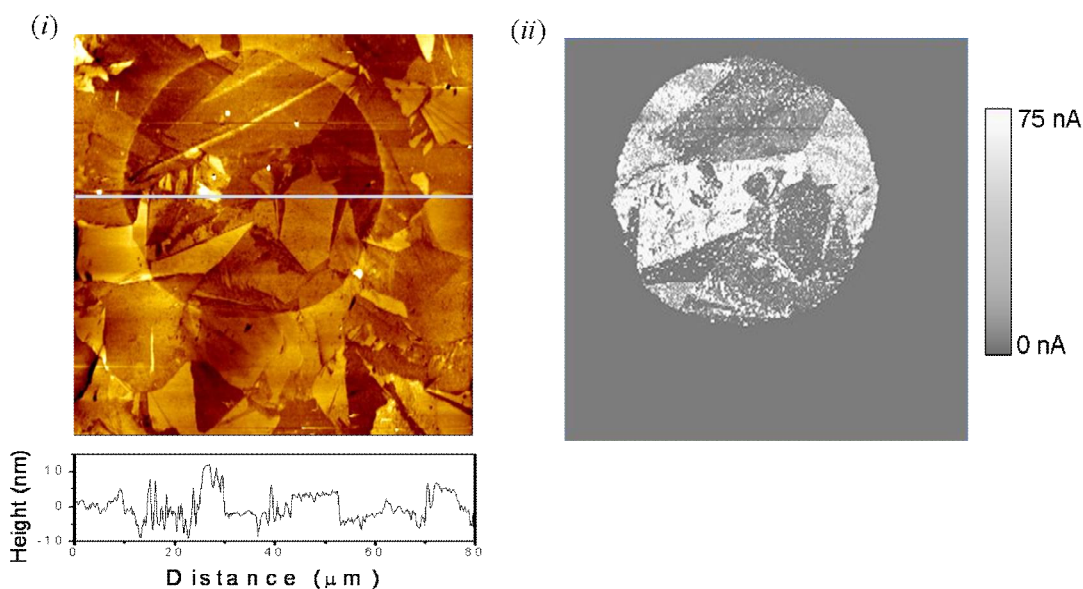
Figure 6.05: Simultaneously recorded C-AFM (*i*) height and (*ii*) conductivity images, recorded at a tip potential of -2.5 V with a 10 MΩ current limiting resistor in series, of a typical BDD microdisc electrode in the array.

The height image demonstrated the remarkably low surface roughness after the final polish, with height differences of only ± 10 nm across the whole area

scanned. The boundary between the BDD electrode and the surrounding intrinsic diamond matrix was clear; however there was only a negligible recess of the electrode with respect to the matrix. Also obvious were the different grains, with sizes between 5 and 20 μm, within the electrode. Figure 6.05 (*ii*) exhibited clear heterogeneities in the conductivity of this BDD electrode, and these were seen to correlate with the location of different grains in the height image (Figure (*i*)). At the tip potential applied, the currents obtained at individual grains were seen to vary by *ca*. one order of magnitude across the sample. Zero current was recorded in the intrinsic diamond regions, as would be expected. Note that the tip current was determined by both the concentration of charge carriers at the BDD and the intrinsic resistance of the sample. It was also of note that no evidence was seen of enhanced conductivity at the grain boundaries. This has been proposed as a predominant active site on other polycrystalline BDD samples.[16]

As mentioned above, *i-V* curves were measured in specific regions of the sample. Figure 6.06 shows *i-V* curves recorded in (*i*) a high-current region and (*ii*) a low-current region of the sample. These measurements were made without a current-limiting resistor. Repeat measurements were carried out in the same position, and these are represented by solid and dashed lines in (*i*) and (*ii*).
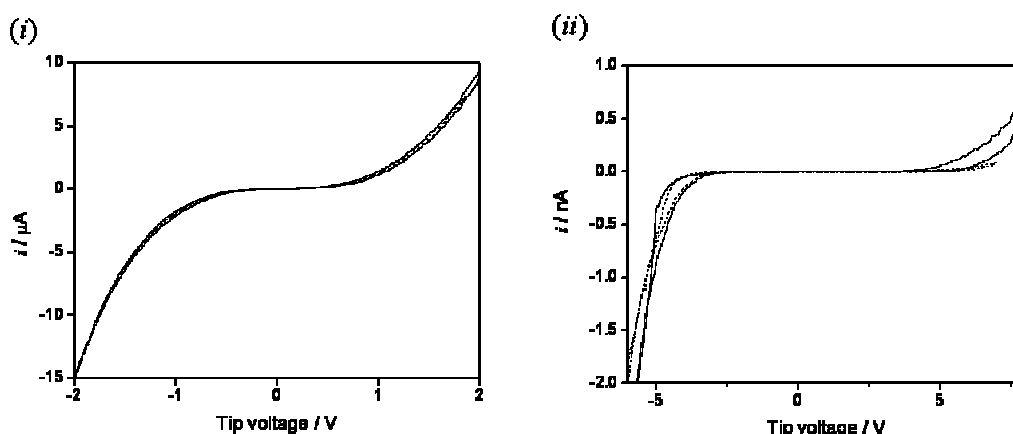
Figure 6.06: Current – voltage curves recorded with the C-AFM tip held stationary in (*i*) a high

conductivity region, and (*ii*) a low conductivity region of the BDD microelectrode shown in

Figure 6.05. The solid and dashed lines represent repeat measurements recorded in the same

zone. Note that no current limiting resistor was present during these measurements.

It was evident that, at both positions, higher currents were recorded at negative

tip potentials, i.e. when the substrate was positively biased. This highlights the *p*-

type semiconducting properties of the material. It was also seen that at a tip

potential of +5 V, those grains which demonstrated low conductivity at -5 V

appeared insulating. In contrast, the most conductive grains showed comparably

high current values in both the negative and positive directions at ±5 V. This

behaviour was true of all BDD electrodes studied within the array.

The significant differences in conductivity demonstrated using C-AFM merited

further investigation, thus SECM was employed to examine the electrochemical

activity of the BDD microdisc electrodes. Note that all electrochemical

measurements were made in regions far from the defect zones of the microdisc

array. Initial, large-scale scans utilised a 25 μm diameter Pt UME as the tip.

Areas of 500 μm × 500 μm were scanned in order to visualise as many BDD

electrodes as possible within one image. Substrate generation-tip collection (SG-TC) mode was used, with the substrate (the BDD microdisc array) biased at a potential to generate $Ru(NH_3)_6^{2+}$ from $Ru(NH_3)_6^{3+}$ in solution. The tip was biased at a potential to collect this electrogenerated $Ru(NH_3)_6^{2+}$ at a diffusion-controlled rate. In this way, the tip provided a map of the electroactivity of the BDD microdisc array. The spatial resolution was determined by the size of the tip.

For all the experiments described herein, the tip current was likely to contain a significant contribution from diffusional feedback between the tip and the BDD array. This was due to the close tip-substrate imaging separations used.[17] SG-TC was used because it allowed variation of the substrate electrode potential over a wide range, thus allowing the visualisation of differences in the electron-transfer rate over a range of driving forces.

Figure 6.07 shows a typical 500 µm × 500 µm image recorded using the SG-TC technique. The 25 µm diameter Pt UME was large in comparison to the grain sizes of the BDD, and as such the tip current, i_t, measured the response of many grains within a single BDD electrode simultaneously. The potential of the BDD microdisc array was maintained at -0.4 V, which was apparently in the diffusion limit (as shown in Figure 6.03), while the tip potential was held at 0.0 V. The tip-substrate separation was held at ~ 10 µm. The tip collection currents have been normalised with respect to the steady–state diffusion-limited current, i_∞, measured for the reduction of $Ru(NH_3)_6^{3+}$ at the tip when positioned in the bulk solution (*i.e.* far from the substrate).
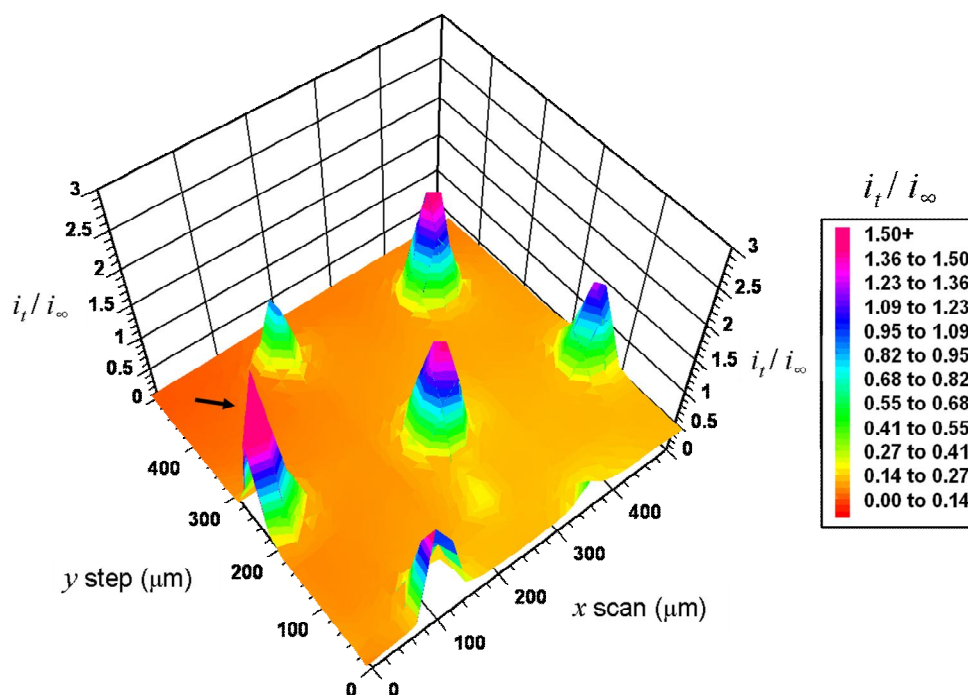
Figure 6.07: 500 μm × 500 μm SG-TC SECM image recorded for the collection of Ru(NH$_3$)$_6$$^{2+}$ electrogenerated from 5 mM Ru(NH$_3$)$_6$$^{3+}$ (in 0.2 M KNO$_3$) at the surface of the BDD microdisc array. The substrate potential was maintained at -0.4 V, whilst the 25 μm diameter Pt UME tip was maintained at 0.0 V. A tip-substrate separation of *ca.* 10 μm was employed during imaging.

The hexagonal arrangement of the BDD electrodes in the array is evident from Figure 6.07. A small downward slope on the sample was apparent in the direction shown by the arrow in Figure 6.07. This was found to result in a change of tip height of ~ 2 μm over the 500 μm × 500 μm region imaged. This was ascertained by recording negative feedback approach curves at the corners of the scan, over the intrinsic (*i.e.* insulating) diamond. It is interesting to note that the electrogeneration of Ru(NH$_3$)$_6$$^{2+}$ appeared to occur to a somewhat different extent at some of the electrodes within the array. These variations in tip current could not be accounted for by the small change in tip-substrate separation; the changes in tip current did not follow the slope of the sample. In order to further

164

investigate these possible heterogeneities in the electroactivity of the BDD microdisc array, high-resolution SECM measurements were carried out using a 5 μm diameter Pt UME as the imaging tip. In this case, the tip-substrate separation was in the range 0.5 – 1 μm.

Figure 6.08 shows a series of three 100 μm × 100 μm images of a single BDD electrode in the array biased at substrate potentials of (*i*) -0.4 V, corresponding to the apparent limiting current for the reduction of $Ru(NH_3)_6^{3+}$ at the array, (*ii*) -0.3 V, and (*iii*) -0.2 V, in order to systematically reduce the driving force for $Ru(NH_3)^{3+}$ reduction at the array. The tip potential was kept constant at 0.0 V, again enabling collection of surface-generated $Ru(NH_3)^{2+}$ at a diffusion-controlled rate.
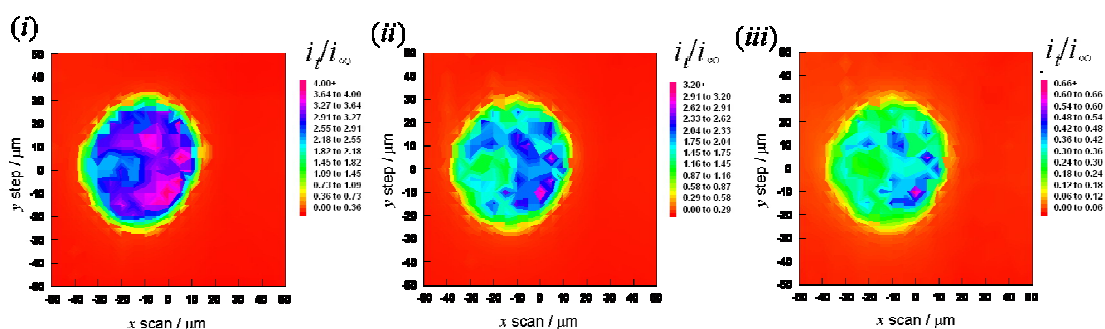
Figure 6.08: 100μm × 100 μm SG-TC SECM images of an individual BDD microdisc in the array at substrate potentials of: (*i*) -0.4 V; (*ii*) -0.3 V; and (*iii*) -0.2 V. The 5 μm diameter Pt UME tip was held at a constant bias of 0.0 V, thus enabling collection of surface-generated of $Ru(NH_3)_6^{2+}$ from 5 mM $Ru(NH_3)_6^{3+}$ (in 0.2 KNO_3) at a diffusion-controlled rate. A tip-substrate separation of *ca.* 0.6 μm was employed.

In Figure 6.08(*i*), the substrate was apparently in the diffusion-limited region for $Ru(NH_3)_6^{3+}$ reduction, yet there were clear variations in the normalised tip current over the BDD electrode surface. Only part of the electrode exhibited

metallic behaviour, as shown by the magnitude of the i_t/i_∞ values. These variations in electroactivity were most likely to be linked to the differences in the conductivity of individual grains within the BDD electrodes, as evidenced by C-AFM measurements (Figure 6.05). The sizes of the domains over which the tip current varied were consistent with the dimensions of the grains as measured using AFM. These variations in current were emphasised further when the driving force for $Ru(NH_3)_6^{3+}$ reduction was decreased from -0.4 V to -0.3 V (Figure 6.08(*ii*)) and then -0.2 V (Figure 6.08(*iii*)).

It was seen that not all electrodes in the array displayed the same degree of tip current variation at -0.4 V as was observed in Figure 6.08. For example, Figure 6.09 shows an individual BDD electrode which exhibits essentially uniform activity with a response similar to a metal disc UME for the tip-substrate separation employed (~1 μm). However, it is interesting to note that as the substrate potential was decreased to -0.3 V and -0.2 V (Figures 6.09 (*ii*) and (*iii*) respectively), different zones of the electrode were seen to have different electroactivity. There appeared to be a very active site in the centre of the BDD electrode. The regions of higher current were likely to be due to those grains which were more conducting.
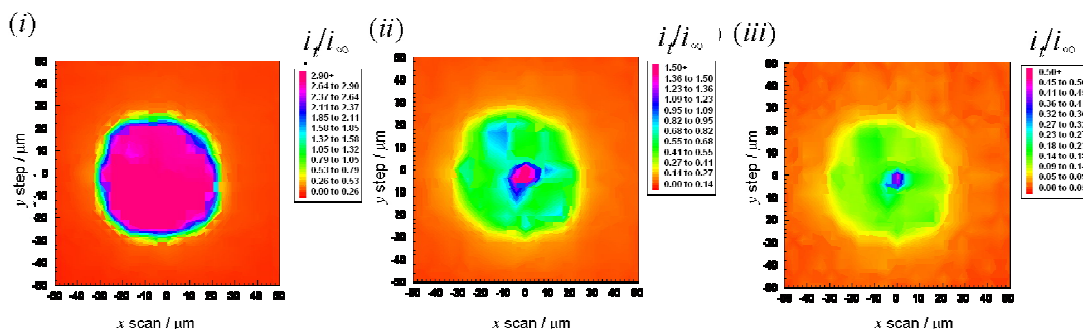
Figure 6.09: SG-TC images of a second individual BDD microdisc electrode in the array at substrate potentials of: (*i*) -0.4 V; (*ii*) -0.3 V and (*iii*) -0.2 V. The experimental conditions were as for Figure 6.08, except that a tip-substrate separation of *ca*. 1 μm was employed.

Feedback approach curves, shown in Figure 6.10, were recorded in the zones of high activity for each BDD microdisc investigated. For all measurements, the tip was held at a potential of -0.4 V, while the substrate was maintained at 0.0 V. The RG of the tip was taken into account and a theoretical approach curve was simulated. It may be seen that, in all three cases, there was a close fit between the simulated data and the experimental current-distance response. These results again suggested the presence of metal-like regions within the BDD microdisc UMEs, which were likely to be linked to grain areas of high conductivity.
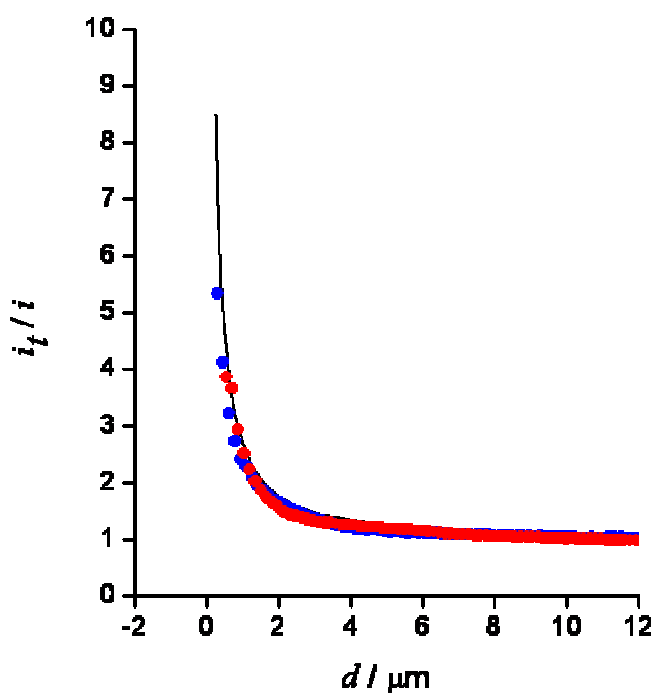
Figure 6.10: Feedback approach curves recorded in the zones of high activity for the two BDD

microdisc electrodes shown in Figure 6.09 (●) and 6.10(●). For all measurements, the tip was

held at -0.4 V and the substrate was maintained at 0.0 V in a solution containing 5 mM

$Ru(NH_3)_6^{3+}$ in 0.2 M KNO_3. the solid line is the theoretical current response for positive

feedback.[18]

To further investigate the spatial variations in the electroactivity of the BDD

microdisc electrodes, high resolution images of silver electrodeposition on the

electrodes were obtained using FE-SEM. Silver was deposited from a solution

containing 1 mM $AgNO_3$ at a potential of -0.2 V for 60 s. FE-SEM images of

two different BDD UMEs within the array are shown in Figure 6.11. Two FE-

SEM detectors were used: (a) the conventional SE2 detector and (b) a high-

efficiency in-lens detector. The latter allowed simultaneous imaging of the grain

structure and silver particle morphology (Figure 6.11 (*ii*) and (*iv*)), whereas the

SE2 detector only imaged the silver particles (Figure 6.11 (*i*) and (*iii*)). In the

latter case, the image contrast was reversed to highlight the positions of the Ag particles.
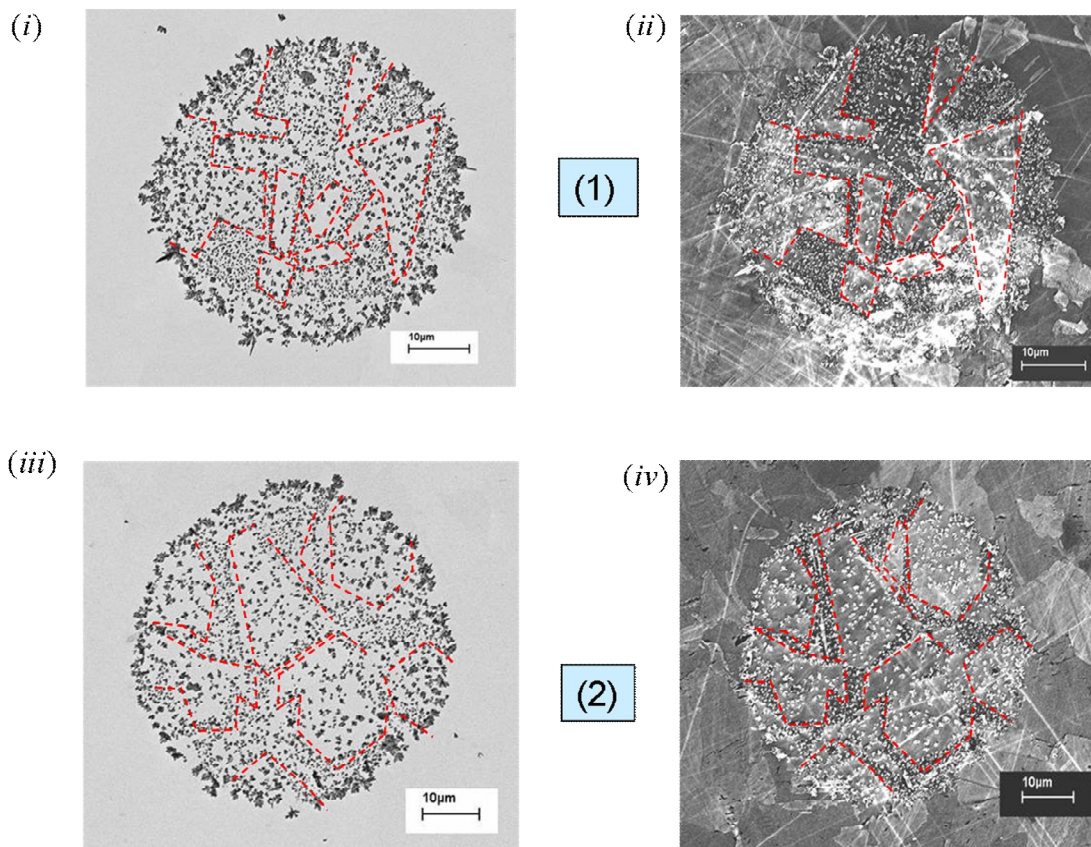
Figure 6.11: FE-SEM images of two different electrodes within the microdisc array (electrode 1: images (*i*) and (*ii*); electrode 2: images (*iii*) and (*iv*)) after electrodeposition of Ag (60 s electrodeposition time from a solution containing 1 mM $AgNO_3$ in 0.2 M KNO_3). Two detectors were used: (1) a conventional SE2 detector; and (2) a high efficiency in-lens detector. The former allowed location of the Ag particles, (*i*) and (*iii*), whereas the latter allowed simultaneous imaging of the grain structure and Ag particle morphology, (*ii*) and (*iv*).

Comparison of the images provided an insight into the variation in conductivity between the grains. The grains that appeared lighter in Figure 6.11 (*ii*) and (*iv*) did so due to a greater degree of charging, and so it may be surmised that they were less conductive. Significantly, it was seen in Figures 6.11 (*i*) and (*iii*) that

silver deposited on both the low and high conductivity grains, suggesting that the former were able to support electron transfer at the applied potentials. However, the nature of silver deposition was obviously different on individual grains; on the less conductive grains, silver formed in larger clumps with a fairly disperse coverage ($\sim 0.8 \pm 0.2$ Ag particles/μm^2), while in the darkest regions, corresponding to the more conductive grains, the silver particles formed a more uniform coverage over the grain surface ($\sim 1.6 \pm 0.3$ Ag particles/μm^2) with no large clusters forming. The red dashed lines in the figure indicate the outline of various grains in the surface. The electrodeposition showed no preference for grain boundaries, which was in agreement with the C-AFM images which showed no enhancement in conductance at these boundaries. Nucleation of silver around the edge of the entire BDD UME was most noticeable, due to higher rates of diffusion.[6] Importantly, the deposition away from the edge of the UME was still significant, indicating that both the edge and the centre of the electrode play important roles in determining the overall current through the UME.

LSCM has been employed to image the development of pH gradients at individual UMEs.[19, 20] The technique was applied in these studies to image the development of pH gradients at the BDD microdisc array under time-dependent conditions. Oxygen reduction occurs at more negative potentials on BDD than for conventional electrode materials, such as Pt.[21] A sufficiently negative potential (-1.4 V) was applied to the array in order to reduce oxygen (and water) present in a solution containing 0.2 M KNO_3 and 10 μM fluorescein. The initial pH was adjusted to 4.7.

The associated local pH changes accompanying the process were imaged using a trace amount of fluorescein, which has a pH-dependent fluorescent signal, from low to high as the pH changes from 5.5 to 7.[20] Images were continuously recorded in the *xy* plane over a time period of 28 s. A selection of these images (each comprising 581 lines) is shown in Figure 6.12. These represent a plane just above (a few micrometres) the array surface. The direction of the LSCM scan was from top to bottom as indicated by the arrow in the first frame.
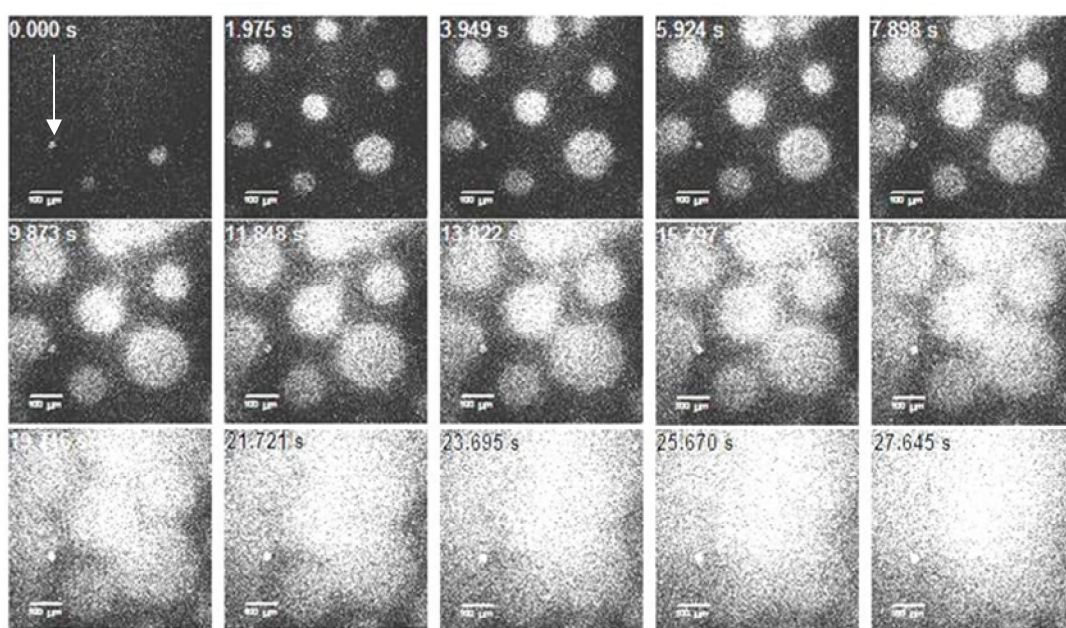
Figure 6.12: A selection of LSCM images of the pH-dependent fluorescence profile of fluorescein at the BDD microdisc array after application of a potential of -1.4 V in a solution containing 0.2 KNO_3 and 10 μM fluorescein, resulting in the local increase of the pH due to reduction of oxygenated water. The scan was started immediately after stepping the potential. The scan direction is indicated in the figure by the white arrow. Images were continuously recorded in the plane parallel to the microdisc array surface over a time period of 28 s. The scale bar in the frame represents 100 μm.

The fluorescence profiles arising from individual UMEs in the array may be clearly seen in the images at the shortest times. Notably, there appeared to be

variation in the activity of the BDD microdisc electrodes within the array, as indicated by the sizes of the fluorescence profiles within individual frames. These observations could not solely be due to temporal factors; for example, the bottom UME in the frame was scanned last, but its fluorescence profile was small compared to the others. After 16 s the fluorescence fields of the individual UMEs began to merge and overlap.

6.5   Highly Ordered Pyrolytic Graphite (HOPG)

6.5.1   Introduction

Another form of carbon which plays an important role in electrochemistry is graphite. Graphite electrodes come in a variety of types; in the studies detailed herein highly ordered pyrolytic graphite (HOPG) was investigated. The surface of HOPG consists of atomically flat, parallel, basal plane graphite sheets separated by steps of 0.335 nm.[22] This sheet structure, illustrated in Figure 6.13, makes HOPG an extremely good electrical conductor. This, coupled with its high chemical stability, makes HOPG an attractive electrode material.[23]
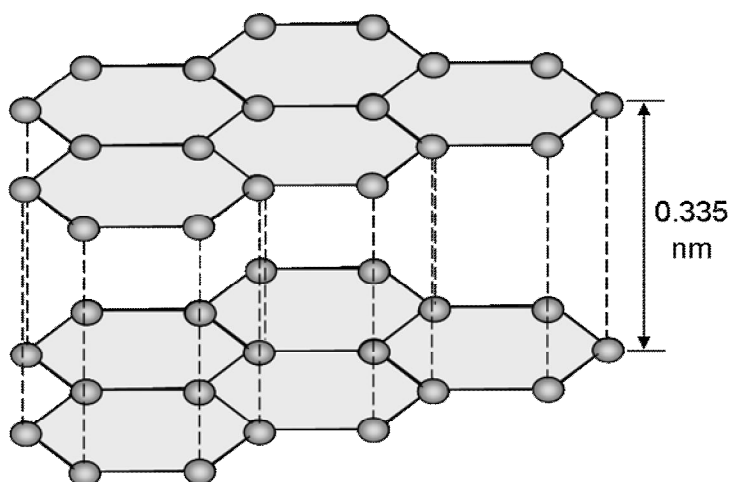
Figure 6.13: Schematic showing the crystal structure of HOPG.

6.5.2   Scanning Micropipette Contact Method (SMCM)

High resolution chemically-sensitive microscopy techniques have proven powerful in elucidating the properties and reactivity of a wide variety of interfaces and interfacial processes, particularly in probing the spatially heterogeneous activity of electrode surfaces.[20, 24-31] This type of experimental technique has led to an understanding of how characteristic active sites on electrode surfaces may dominate the overall electrochemical response,[20, 27-31] providing insights that cannot be obtained by classical voltammetric methods alone.

Among electrochemical mapping techniques, scanning electrochemical microscopy (SECM)[27-33] is particularly popular and now well-established for imaging both surface topography[32, 34] and the reactivity of electrode substrates.[16, 27-31, 35-44] SECM utilizes an ultramicroelectrode (UME) as a mobile tip, the response of which provides information on the physicochemical properties of an underlying substrate. There is a growing family of SECM operation modes,[27, 28, 31, 45, 46] among which the feedback mode[30, 34, 47] and generation/collection[48, 49] modes are used most in the investigation of electrode surfaces and related interfaces. In the feedback mode, the tip is used to generate a redox species from a precursor in solution, which may be regenerated at the substrate, thereby enhancing the tip current. In the generation-collection modes, one working electrode (tip or substrate) generates a species which is then collected by the second electrode (substrate or tip).

The spatial region probed by SECM is greater than the dimensions of the active part of the UME probe,[50] and is sensitive to the tip-substrate separation, the surface kinetics and the detection mode employed.[50] While probe electrodes with characteristic dimensions of less than 1 µm have been fabricated,[50-53] they have proved generally difficult to reproduce, characterize and deploy as imaging probes, as evidenced by a relatively sparse number of reports and limited applications.[54-57] Furthermore, edge diffusion to the tip electrode in all SECM modes and the overlap of diffusion fields of neighboring active sites on the substrate, for tip collection measurements, results in a loss of lateral resolution.

Microcapillary-based techniques have previously been employed to probe the electrochemistry of small areas of macroscopic electrode surfaces. [58-62] This approach has been used to examine the electrochemical properties of defined areas on metal surfaces. For example, the technique has been used to study pit initiation on stainless steels[58, 59]. Tip diameters between 1 and 1000 µm were employed, with a solution-filled capillary attached to the lens of a microscope, to allow easy positioning over the site of interest. The substrate generally served as a working electrode and the reference electrode was connected externally to a microcapillary via an electrolytic bridge. This technique was subsequently adapted[63] to incorporate a flow-through capillary system to allow use in applications with large current densities (> 100 A/cm^2).

Initially, the microcapillary technique only allowed individual measurements to be made at specific surface locations, but was subsequently developed[64] to facilitate surface imaging. To date, these experiments have tended to focus on

surface electrochemical processes intrinsic to corrosion and passivation,[60, 61] but there is clearly scope for investigating electrochemical processes involving solution redox couples, which is the focus of the studies herein. Such applications require a detailed description of mass transport within the micropipet and this aspect is addressed in this paper. For completeness, it should also be mentioned that micropipets have been used as the imaging probes in both scanning ion conductance microscopy (SICM)[65-74] and SECM.[75-77] In these cases the tip does not usually make intimate contact with the surface, although SICM has been used in this format to carry out nanowriting on surfaces.[78, 79]

In this chapter the use of a scanning micropipet contact method (SMCM) is reported which allows electrochemical reactions of solution species to be carried out on an electrode surface in a highly localized manner, exemplified by two systems. First, we consider carbon electrodes, where localised electroactivity measurements are especially topical in the light of recent reports which have suggested that specific sites (e.g. step edges or defects) appear to play a significant role in the electrochemistry of highly ordered pyrolytic graphite (HOPG) and carbon nanotube electrodes.[80] In particular, it has been suggested that the electron transfer (ET) rate at basal plane HOPG is vanishingly small[23, 81] and that a sparse density of step edges dictates the overall response of conventional voltammetric studies. It has recently been proposed that the standard rate constant for ferrocyanide oxidation at basal plane HOPG is less than 10^{-9} cm s^{-1}.[80, 82] Much of the previous work on HOPG[80, 83-89] has focused on conventional cyclic voltammetric (CV) studies, but this represents the response of the entire surface. In contrast the micropipette method offers the opportunity

to focus measurements on a small area of an electrode surface, which in the case

of HOPG is smaller than the typical inter-step spacing on the basal plane.

6.6 SMCM Studies of HOPG: Experimental

This section describes the preparation processes and instrumentation used in

studies of HOPG.

6.6.1 Materials

All aqueous solutions were prepared using Milli-Q reagent grade water with a

resistivity *ca.*18.2 MΩ cm at 25 °C. Solutions contained 0.1 M NaCl or KNO_3 as

the supporting electrolyte. NaCl (AR grade), potassium ferrocyanide (II) (99%)

and potassium ferricyanide (III) (99%+) were purchased from Sigma-Aldrich,

and used as received. Trimethylammoniomethylferrocene hexafluorophosphate,

$(FA^+PF_6^-)$, was obtained by metathesis of trimethylammonioferrocene iodide

(FA^+I^-) with $AgPF_6$ following a procedure reported elsewhere.[90] HOPG was the

highest grade obtainable (ZYA grade) 12 mm x 12 mm x 2 mm (SPI Supplies,

West Chester, PA, USA).

6.6.2 Electrical Contact to HOPG

HOPG was adhered onto a square section of printed circuit board (PCB), with an

underlying electrical contact, using double sided adhesive tape (Agar Scientific).

Silver dag was gently applied to the edge of the HOPG and the PCB so that a

continuous electrical connection was made. Tinned copper wire was soldered to

the PCB in order to make an external electrical contact. Before undertaking each

experiment, a freshly prepared HOPG surface was obtained by cleaving using adhesive tape.[91]

6.6.3 Electrochemical Setup

Micropipettes with internal diameters of ~ 1 μm were pulled from standard borosilicate capillaries (Harvard Apparatus, UK) of dimensions (o.d. x i.d.) 1.0 x 0.58 mm, respectively, using a laser puller (P-2000, Sutter Instruments, USA). Voltammetric measurements were carried out using a two-electrode set-up with the substrate of interest serving as the working electrode. A potential was applied with respect to a Ag/AgCl reference electrode present within the micropipette. The micropipette acted as a vessel for the redox mediator in electrochemical experiments, with the electrochemical processes occurring when the meniscus came into contact with the surface, as shown in Figure 6.14.
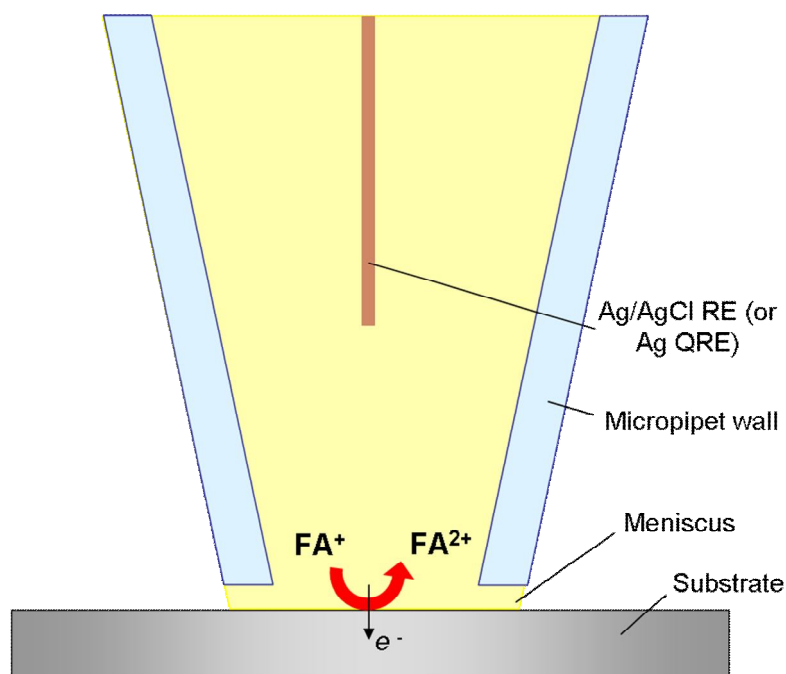
Figure 6.14: Schematic showing the principle behind the Scanning Micropipette Contact Method (SMCM).

177

For initial CV experiments on HOPG, a micropipette with initial tip diameter ~ 580 nm was employed. The position of the tip with respect to the substrate was controlled using a Nanocube piezo block (Physik Instrumente, Germany), allowing movement of the tip in the *x*, *y* and *z* directions over 100 µm with 1 nm resolution. Initial coarse tip movements were made using a micrometer (Newport, NJ, USA). A camera (PixeLINK, Edmund Optics) was utilised to monitor the proximity of tip and substrate. A typical image of a micropipette approaching a surface is shown in Figure 6.15.

Figure 6.15: Optical image showing a 300 nm diameter micropipette approaching the HOPG surface. Scale bar represents 500 µm.

Software, written in-house using LabVIEW (National Instruments), facilitated the approach of the tip to the HOPG in the *z* direction, typically with a 10 nm step size. A potential of 1 V was applied to the HOPG in order that an easily distinguishable current would be generated upon meniscus contact with the

HOPG surface (due to the oxidation of either trimethylammonioferrocene, FA^+, or potassium ferrocyanide (II), $Fe(CN)_6^{4+}$). On fulfillment of this condition, the z approach program automatically paused, holding the meniscus in contact with the surface and allowing further electrochemical measurements to be carried out. CVs were run using additional LabVIEW software, also written in-house.

For extended electrochemical experiments on HOPG, which involved scanning the probe micropipette over the sample in the x and y directions, a further LabVIEW program was used. This ensured that the tip was not pulled across the sample whilst in contact; rather it approached the surface, paused on contact whilst either the steady-state current generated at that point, or current-voltage curve, was recorded. The tip then retracted back from the surface a defined distance in the z direction (typically 5 μm) before moving in the x and/or y direction and repeating the process. A tip with initial diameter ~ 580 nm was employed for experiments on HOPG. Several line scans were acquired with a 100 nm separation between points and between each line.

6.6.4   Finite element modeling

All numerical simulations were performed on a Viglen Intel Core 2 Duo 2.4 GHz computer equipped with 4 GB of RAM and running Windows XP 64 bit edition. Modelling was performed using the commercial finite element modelling package Comsol Multiphysics 3.3a (Comsol AB, Sweden), using the Matlab interface (Release 2006b) (The MathWorks, Cambridge, UK). Simulations were typically carried out with 15000 triangular mesh elements. Mesh resolution was defined to be greatest in regions where the concentration gradients were steepest.

Simulations with finer meshes were carried out (not shown) to confirm the mesh was fine enough to not adversely affect the accuracy of the solution.

6.7 SMCM: Experimental Results

The micropipette contact method was first used to record cyclic voltammograms (CVs) on HOPG. ZYA grade basal plane HOPG was employed as the substrate. This material exhibits the ultimate HOPG order currently available[92] and as such offers the widest step spacing. Exhaustive atomic force microscopy (AFM) studies have been undertaken to approximate the average step spacing in ZYA grade HOPG. Typical images are shown in Figure 6.16. The step density was found to vary between 0.2 and 0.7 $\mu m\ \mu m^{-2}$ with a mean of $0.5 \pm 0.1\ \mu m\ \mu m^{-2}$. This suggested an average step spacing of 2 μm.
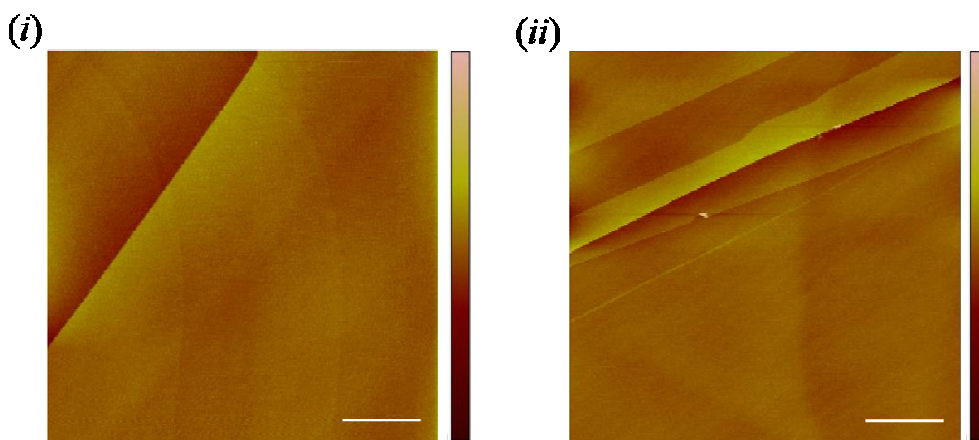
Figure 6.16: Typical tapping mode atomic force microscopy (AFM) images of ZYA grade HOPG. Scale bar 1 μm, height range 0 - 5 nm. (*i*) shows a region with a step density of 0.2 $\mu m/\mu m^2$; (*ii*) shows a region with a step density of 0.7 $\mu m/\mu m^2$.

The micropipettes used in the SMCM studies had a maximum diameter of 1 μm and thus it would be expected that they would only ever cross a maximum of one step edge. The laser puller employed produces highly reproducible micropipettes,

and thus they were pulled in batches, and some retained for FE-SEM imaging. Figure 6.17 shows a CV recorded at 100 mVs^{-1} plotted in tandem with a simulated CV. On comparing experimental results to those obtained by simulation, there is a clear fit to Nernstian kinetics. The simulations for Butler-Volmer kinetics with $k_0 = 0.01$ cm s^{-1} illustrate the poor fit for this regime in contrast to the Nernstian case. This suggests that in fact the basal plane contributes to the overall electrochemistry to a greater degree than has previously been reported. The simulated results revealed that the currents obtained correlated to a micropipette with a tip diameter of approximately 550 nm.
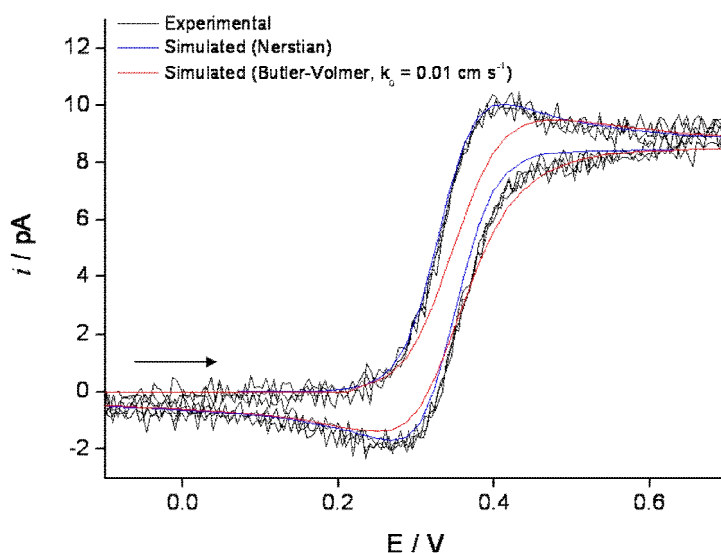
Figure 6.17: Plot to show the fit between experimental (black) and simulated (blue and red) cyclic voltammograms for a micropipette with $r_p = 225$ nm. The solution was FA$^+$ (2 mM) with 0.1 M NaCl. The arrow indicates the direction of the scan. A clear fit is seen to Nernstian kinetics.

The scanning aspect of the technique was first introduced as a short series of linescans across the sample. Figure 6.18 shows a series of three linescans carried out with a 550 nm micropipette using two redox mediators, (*a*) FA$^+$, and (*b*)

$Fe(CN)_6^{4-}$, at a concentration of 2 mM. Rather than apply a potential corresponding to the limiting current, the half-wave potential was applied so that the current would reveal information on any variations in electrode activity. Any significant decrease in local electrode activity could cause a significant decrease in the activity of the electrode surface, certainly with the values of k_0 claimed for basal plane graphite.[83] No significant variation in current across the scan was apparent. This suggests that the basal plane is evidently uniformly active at the length scale considered in these studies.
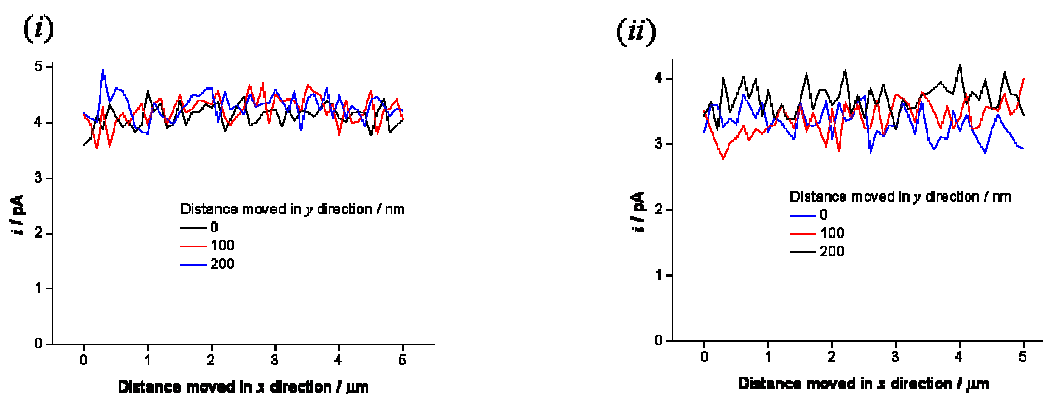
Figure 6.18: Linescans to show the current generated when the half-wave potential was applied at a series of points across the HOPG surface, using (*i*) FA^+ or (*ii*) $Fe(CN)_6^{4-}$ as the redox mediator.

With measurements made over this range, in further experiments, CVs were also recorded at a number of points across the HOPG surface using a 550 nm tip containing 2 mM FA^+, as shown in Figure 6.19. These again indicate that the surface exhibits fundamentally uniform electroactivity, as the quasi-peak current is almost identical across the series of CVs.
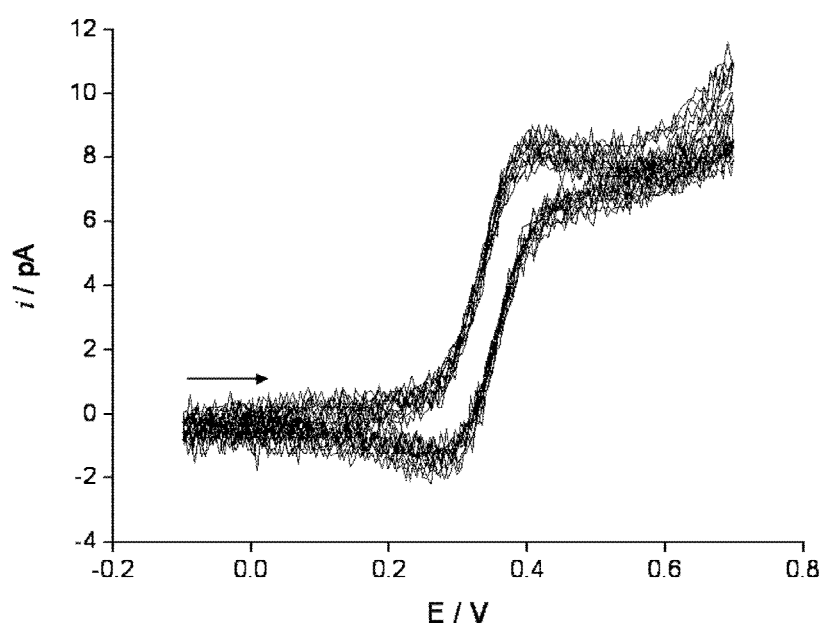
Figure 6.19: Plot showing a series of cyclic voltammograms recorded at consecutive points on the HOPG surface for a 550 nm diameter micropipette. Three CVs were recorded at each position. The scan rate was 150 mV s^{-1}. The arrow indicates the direction of the scan.

These studies highlight that on a micron scale basal plane HOPG is uniformly and highly active towards redox reactions of iron complexes, as evident from studies of $Fe(CN_6)^{4/3-}$ and $FA^{+/2+}$. It is important to highlight that the basal plane itself contains defects. It is impossible to determine the density of defect sites on the basal plane of HOPG. Therefore, it would be unwise to assume that the basal plane is uniformly atomically flat and that step edges are the only regions where edge plan graphite is exposed and thus able to exert an effect on the electrochemistry of the substrate. The cleaving process has the capacity to impart defects on the HOPG surface, and these defects are likely to be randomly spaced and distributed across the HOPG surface. They will have a comprehensive effect on the electrochemical response. On the length scale considered in this investigation, *i.e.* hundreds of nanometres, the basal plane appears uniformly

active. However, the hypothesised surface defects on this plane may only be nanometres in length, and so many may be addressed by the scanning micropipette at any one time. Thus, it may be ill-advised to categorise different regions of HOPG as "basal plane" and "edge plane" when in fact the former is highly likely to contain elements of the latter.

6.8   SMCM: Simulation Results

In order to support the SMCM experiments, the finite element method[93] was used to simulate cyclic voltammograms generated using SMCM. The equation solved on the interior of the domain illustrated in Figure 6.20 is the time-dependent diffusion equation cast in axisymmetric coordinates (eq 6.02).

$$\frac{\partial c}{\partial t} = D\left(\frac{\partial^2 c}{\partial z^2} + \frac{1}{r}\frac{\partial c}{\partial r} + \frac{\partial^2 c}{\partial r^2}\right) \tag{6.02}$$

where z and r are the axial and radial coordinates respectively. We take the diffusion coefficient of both forms of the redox couple, D, to be identical in order to reduce the problem to the consideration of one species. The concentration of FA^+ is represented by c.
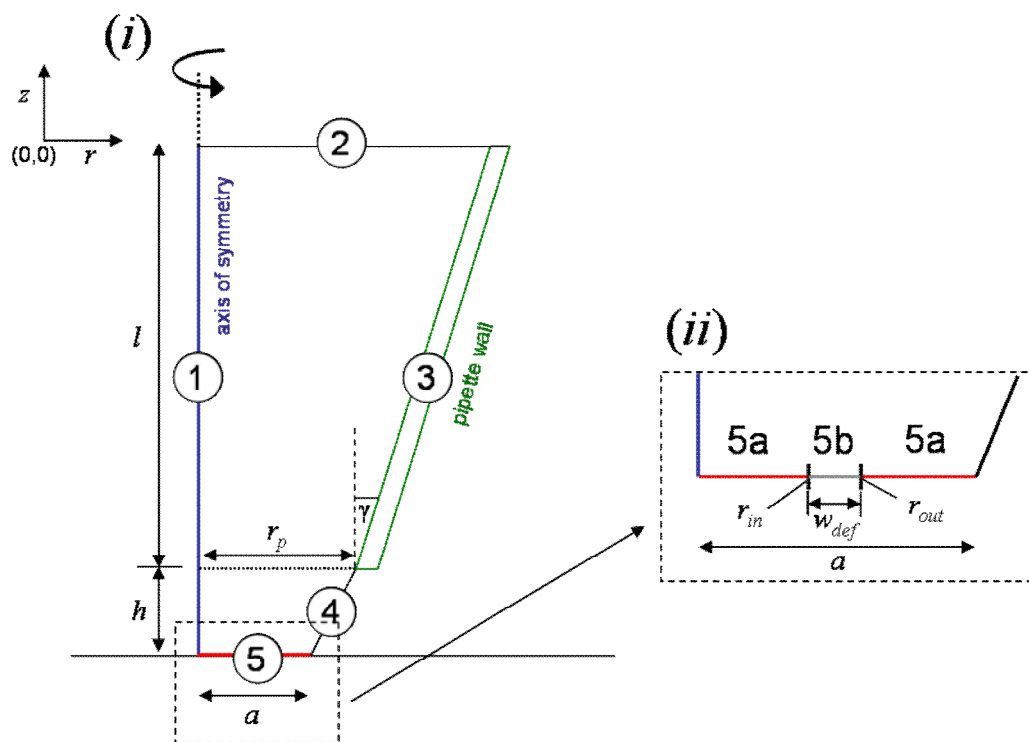
Figure 6.20: Simulation domain for the axisymmetric cylindrical geometry used to model the micropipet system: (*i*) the full geometry for a uniformly active surface; and (*ii*) the modification when the substrate is partially active.

Table 6.01 shows the boundary conditions for the simulation of the voltammetric response of a micropipette in the contact method. In Table 1, the geometric quantities r_p, a, l, and h represent the pipette radius, the contact radius with the substrate, the length of the pipette considered in order to obtain a good solution and the height of the meniscus, respectively (as depicted in Figure 6.20). The pipette semi-angle is denoted by γ, $\underline{n}$ represents the inward pointing unit normal vector and c^* represents the bulk concentration of FA^+.

Boundary Description	Number in Figure 3	Coordinates	Equation
Solution/electrode interface (uniform surface)	5	$z=0$, $0 \leq r \leq a$	$c = \dfrac{c^* \theta}{1+\theta}$ (case 1) $\dfrac{\partial c}{\partial z} D = k_b (c_b - c) - k_f c$ (case 2)
Solution/electrode interface (basal plane)	5a = basal plane	$z=0$, $0 \leq r \leq r_{in}$ AND $r_{out} \leq r \leq a$	$0 = \nabla c \cdot \underline{n}$
Solution/electrode interface (defect)	5b = defect	$z=0$, $rin \leq r \leq r_{out}$	(case 1) and (case 2) as for boundary number 5
Meniscus/air interface	4	$0 < z < h$ $r = \left(\dfrac{r_p - a}{h}\right) z + a$	$0 = \nabla c \cdot \underline{n}$
Capillary wall	3	$r = l \tan \gamma + r_p$ $h \leq z \leq l$	$0 = \nabla c \cdot \underline{n}$
Bulk solution	2	$0 < r < z \tan \gamma + r_p$ $z = l + h$	$c = c^*$
Axis of symmetry	1	$r = 0$, $0 < z \leq l + h$	$0 = \nabla c \cdot \underline{n}$

Table 6.01: The boundary conditions for the simulation of the voltammetric response of a micropipette in the contact method.

In Table 6.01, the geometric quantities r_p, a, l, and h represent the pipette radius, the contact radius, the length of the pipette and the height of the meniscus respectively (as depicted in Figure 6.20). γ represents the pipette semi angle. $\underline{n}$ represents the inward pointing unit normal vector. c^* represents the bulk concentration. At the solution/electrode interface, there are two possible cases: Nernstian kinetics (case 1),[94] where

$$\theta = \exp\left(-\eta \cdot \frac{nF}{RT}\right) \tag{6.03}$$

and η is the overpotential, defined as $E-E^{0'}$, where $E^{0'}$ is the formal electrode potential; or Butler-Volmer kinetics (case 2),[95] where

$$k_f = k_0 \exp\left[-\alpha \frac{nF}{RT}\right] \tag{6.04}$$

and

$$k_b = k_0 \exp\left[(1-\alpha)\frac{nF}{RT}\right] \tag{6.05}$$

where k_f and k_b are the rate constants for electron transfer (reduction, k_f; oxidation, k_b) and a typical value of the transfer coefficient, $\alpha = 0.5$, has been used.

The cases outlined above are for the situation where the portion of the substrate investigated is uniformly active. Figure 6.20(*ii*) shows the simulation domain at the solution/electrode interface when the presence of a defect is taken into consideration. Here, r_{in} and r_{out} represent the inner and outer radii, respectively, of the defect, and w_{def} represents the width of the defect, where

$$w_{def} = r_{out} - r_{in} \tag{6.06}$$

For simplicity and to maintain the axisymmetric geometry, we are thus considering a ring-shaped defect but we have chosen parameters such that the equivalent length of step encapsulated by the capillary is above the maximum we might expect to find on a surface, for the case of HOPG.

It is difficult to predict the shape that the meniscus takes on contact with the surface as it depends on factors such as the hydrophilicity/hydrophobicity of the substrate electrode surface and the volume of solution contacting the electrode. However, preliminary simulations demonstrated that the meniscus shape had little effect on the steady-state current, as shown in Figure 6.17. Simulations were carried out for a micropipette with $r_p = 1$ μm, $l = 400$ μm, and a solution of concentration 2 mM with $D = 6 \times 10^{-6}$ cm^2 s^{-1} to investigate the effect of varying the value of a (the contact radius) on the current, as shown in Figure 6.17. In this plot, which is for a meniscus height, $h = 100$ nm, the currents have been normalised by the current when the contact radius is the same as the pipette, to give a normalised steady-state current, i_{ss}. It can be seen that as the radius, a, decreases from 1.0 μm (equivalent to the internal radius of the pipette) to 0.5 μm, there is essentially no change in the current. This is because the steady-state current is largely dominated by diffusion through the capillary. Only at smaller contact radii does the current fall, as the size of the electrode contact becomes more important. For subsequent simulations (unless explicitly mentioned), including the analysis of experimental data, a was given a value of r_p, which was considered to be reasonable.
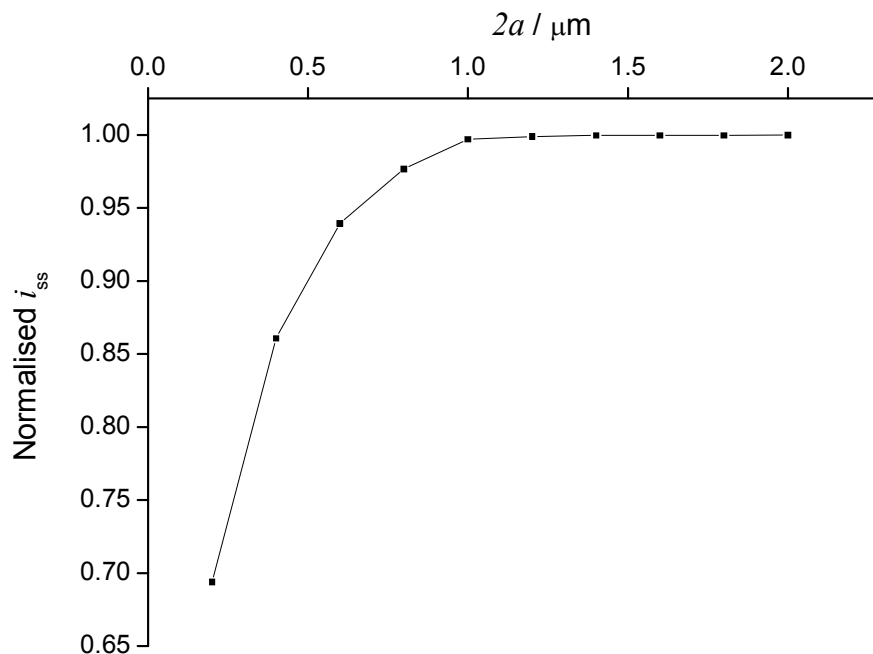
Figure 6.21: Plot of simulated data demonstrating how the steady state diffusion-limited current

(normalised as described in the text) at a 1 μm radius micropipette ($l = 400$ μm, γ=7.5°, c*=2

mM, $D = 6 \times 10^{-6}$ cm^2 s^{-1}) is affected by the meniscus radius, a.

Figure 6.22 shows the results of simulations to investigate the effect of varying the height of the meniscus. The simulation was again for a 1 μm radius micropipette (contact radius, $a = 1$ μm). For values of h between 0.2 μm (to which all steady-state currents, i_{ss}, have been normalised) and 2 μm there was a decrease in current of only 18%. The micropipette semiangle of 7.5° used in these simulations was estimated from FE-SEM images and is typical of the probes employed in practice.
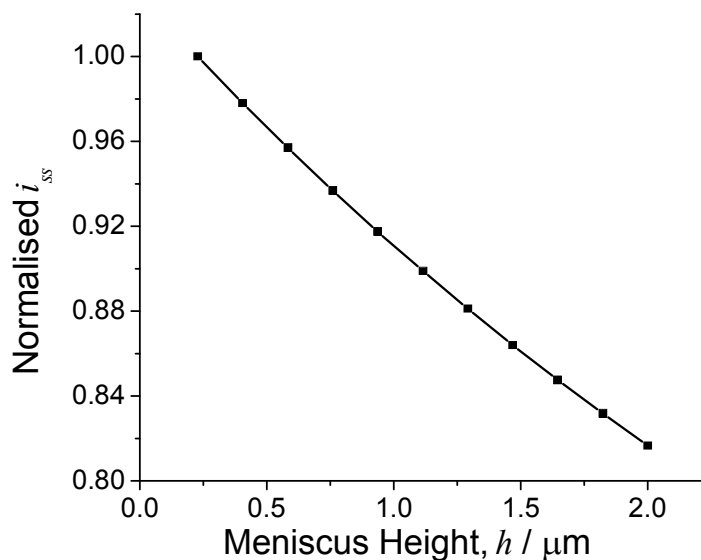
Figure 6.22: Plot of simulated data demonstrating how the steady state diffusion-limited current (normalised as described in the text) at a 1 μm radius micropipette ($l = 400$ μm, $\gamma=7.5°$, $c^*=2$ mM, $D = 6 \times 10^{-6}$ cm^2 s^{-1}) is affected by the meniscus height, h.

Figure 6.23 shows theoretical CVs obtained for a variety of scan rates, ranging from 20 mV s^{-1} to 1 V s^{-1}, for a micropipette with $r_p = 1$ μm and semiangle 7.5°, and meniscus with $a = 800$nm and height $= 200$ nm. The diffusion coefficient used was 1 x 10^5 cm^2 s^{-1}. The CVs demonstrate that, for the Nernstian case, a quasi-steady state current is ultimately attained on the timescales studied herein. The current shows a slight scan rate dependence over this range because the concentration boundary that develops is relatively large compared to the electrochemically active area.
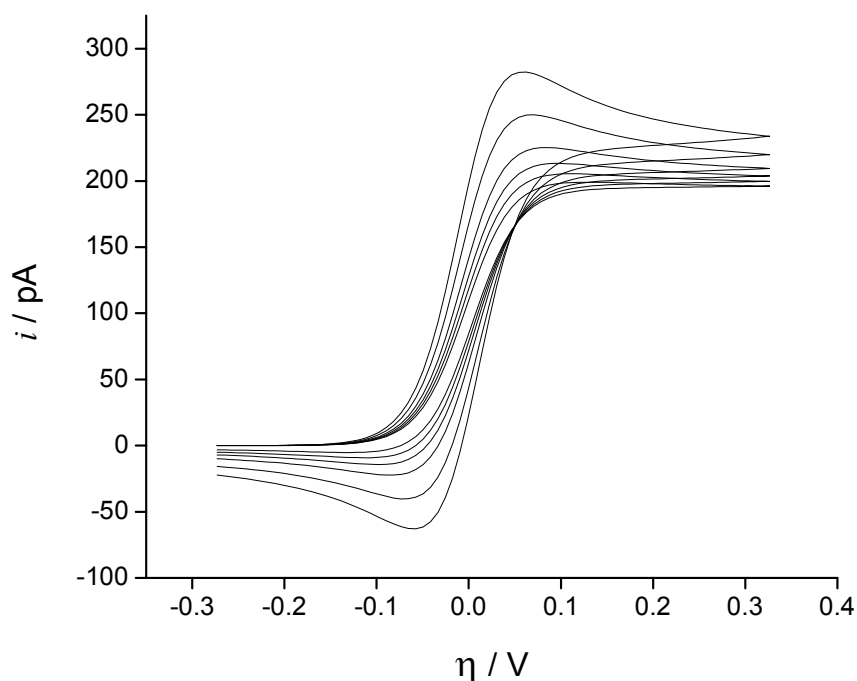
Figure 6.23: Simulated cyclic voltammograms at scan rates of 20, 50, 100, 200, 500 and 1000 mV s^{-1} for Nernstian ET at a 1 μm radius micropipette (a=800 nm, c*=5 mM, h=200 nm, γ=7.5°). The arrow indicates the direction of the scan.

Figure 6.24 highlights the influence of kinetics on the voltammetric response. It is clear that the transition from the Nernstian case to Butler-Volmer conditions induces a significant change in the shape and position of the voltammograms. Even for a standard rate constant of 0.1 cm s^{-1}, there is a measurable change in the voltammetric waveshape that could be determined experimentally, and as k_0 decreases to 0.01 cms^{-1} and 0.001 cm s^{-1} the shift in half-wave potential is siseable and easily measurable. Clearly, standard rate constants quoted for basal plane HOPG[80, 82] of 10^{-9} cm s^{-1} would result in barely any current over the voltammetric range shown, so allowing the activity of electrode surfaces to be elucidated with high confidence using this technique.
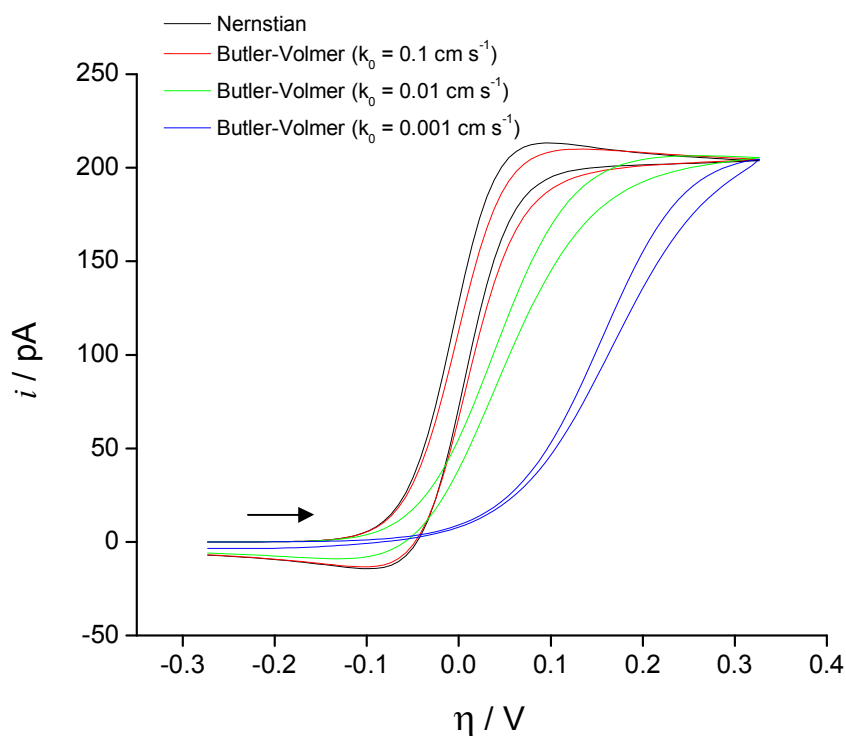
Figure 6.24: Simulations showing the effect of kinetics on the shape of cyclic voltammograms.

Black: Nernstian response. Red: $k_0 = 0.1$ cm s^{-1}. Green: $k_0 = 0.01$ cm s^{-1}. Blue: $k_0 = 0.001$ cm s^{-1}.

Scan rate 100 mV s^{-1}. The concentration of electroactive species was 5 mM, with $r_p = 1\mu$m, $a =$

800 nm, $h = 200$ nm, and $l = 400$ μm. The arrow indicates the direction of the scan.

Figure 6.25 shows a typical steady-state concentration profile within a 1 μm radius micropipette ($r_p=a=1$ μm), having a semiangle of 7.5°, where an electroactive species is consumed at the substrate electrode at a diffusion-limited rate. This demonstrates that the concentration change occurs over *ca.* 100 μm (assuming that 95% bulk concentration approximates to the bulk). A steady-state can be achieved because the pipette allows some non-linear diffusion, although clearly not to the extent that would be observed at an inlaid disk electrode. Nonetheless, this is an important feature of the micropipette method and the

relatively high mass transport rates that result are attractive for the measurement of fast kinetics.
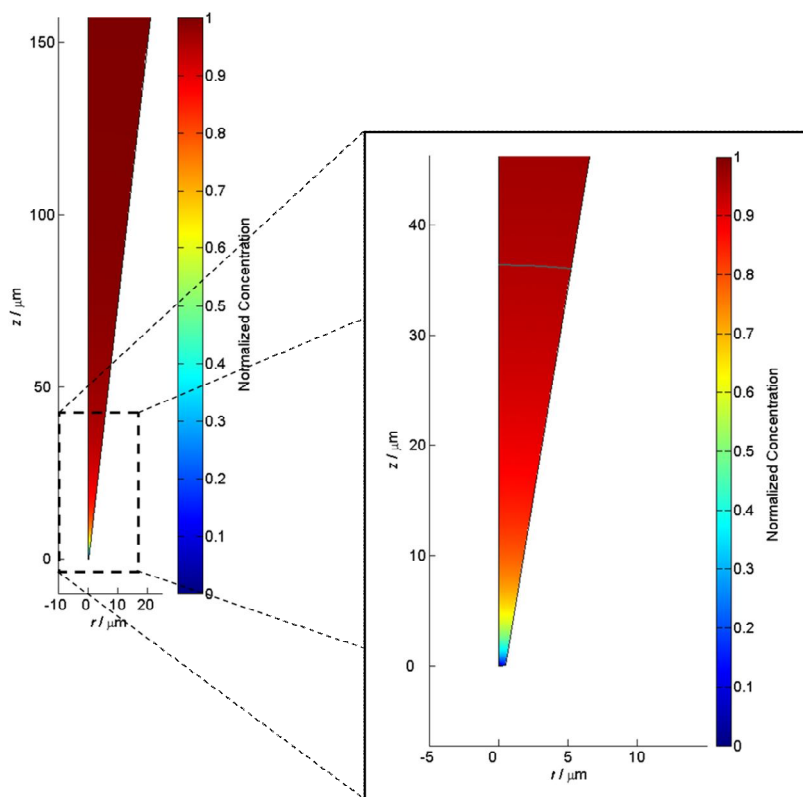
Figure 6.25: Simulated concentration profile within a micropipette where $r_p = a = 500$ nm, $c* = 2$ mM, $h = 100$ nm, and $l = 0.4$ mm. The contour line on the magnified image shows 95% concentration.

Figure 6.26 compares the response of a uniformly active surface with one where there is a 1 nm wide active step edge set in an inert (basal) plane, with $r_p = a = 250$ nm, $h = 20$ nm, $l = 400$ µm, and a solution of concentration 5 mM, with $D = 6 \times 10^{-6}$ cm^2 s^{-1}.
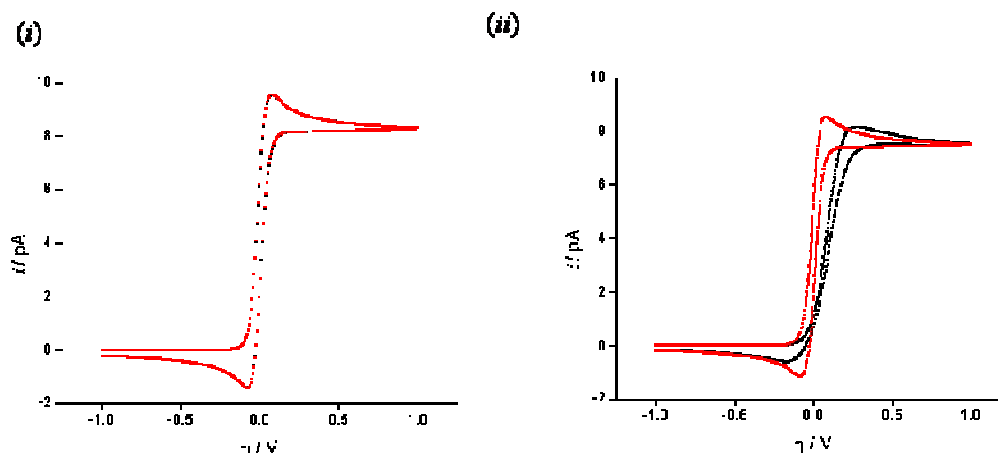
Figure 6.26: Simulations showing the voltammetric responses of (*i*) a uniform surface with Nernstian response (red) and Butler-Volmer (black) kinetics with $k_0 = 0.5$ cm s^{-1}; compared with (*ii*) a surface containing a 1 nm width step defect (see Figure 3 for geometry). In this latter situation the data are for Nernstian ET (red) and Butler-Volmer kinetics (black) with $k_0 = 0.5$ cm s^{-1} inert basal plane. A 580 nm diameter micropipette containing 2 mM redox active species ($D = 6 \times 10^{-6}$ cm^2 s^{-1}) was simulated. The arrows indicate the direction of the scans. Horizontal line to aid comparison.

Simulated CVs for a uniformly active surface are shown in Figure 6.26(*i*) for Nernstian ET (red line) and Butler-Volmer kinetics (black line) with $k_0 = 0.5$ cm s^{-1}. The two voltammetric waveshapes in this case are very similar; and the half-wave potentials are essentially coincident. Conversely, for rapid Butler-Volmer kinetics ($k_0 = 0.5$ cm s^{-1}) when only the defect is active there is a large deviation in the half-wave potential from Nernstian behavior on the step edge, as exhibited in Figure 6.26(*ii*). Notably, the limiting steady-state current is independent of the kinetics, as would be expected. However, there is a small difference in the voltammetric behavior for the case of the uniformly active surface and step edge active surface (compare the red curves in Figure 6.26 (*i*) and (*ii*); note the slight difference in the limiting currents). However, the small difference seen in the

194

simulations would be difficult to elucidate in practice. In summary, the analysis of the simulations indicates that for a uniformly active surface one can measure quite rapid kinetics with the SMCM technique. For the case where only a small step-like portion of the surface is active, even very fast kinetics ($k_0 > 0.5$ cm s^{-1}) can be distinguished due to the high mass transport rate to the step.

6.9   Conclusions

BDD microdisc array electrodes, insulated within an intrinsic diamond matrix, represent an important advance in the development of array electrodes. The arrays make use of the interesting properties of BDD in a coplanar configuration, and may be cleaned repeatedly using standard mechanical polishing procedures. Each BDD microdisc contains polycrystalline BDD with a variety of different grains exposed, as elucidated using C-AFM. SECM measurements revealed that even under apparent diffusion-limited conditions (as determined by CV experiments) the response varies slightly between individual electrodes, with some showing heterogeneous electroactivity. However, under these conditions, most electrodes demonstrate predominantly metallic behaviour.

Importantly, at applied potentials below the diffusion-limited regime, significant spatial variations in the electroactivity of individual electrodes are observed. Spatially heterogeneous electron-transfer rates are seen, and are likely to be linked to the underlying wide variations in intrinsic conductivity of individual grains. These variations cannot readily be determined from conventional, bulk-scale characterisation methods, such as CV, but are trivially visualised using SECM and FE-SEM imaging of silver deposition at the BDD microdiscs. The

results described herein suggest that BDD microdisc arrays of this type can be used for diffusion-limited amperometric detection, but also suggest that caution is advised for analysis of voltammetric wave shapes. In this case, an understanding of the underlying conductivity and spatial variations in electrode activity is required; at potentials shy of the diffusion-limited regime, differences in the turnover rate of electroactive species resulting from variations in the electron-transfer rate constant across a microelectrode surface are accentuated. It is clear that this factor would impact on the analysis of the voltammetric wave shape, as conventional models for microelectrodes assume a uniform rate constant across a surface.

SMCM has proven a valuable tool for probing the localized electroactivity of heterogeneous electrode surfaces. The small dimensions of the micropipette probe allow voltammetric measurements to be made in microscopic regions of an electroactive surface. In SMCM, the tip converges on the surface and so there are no issues related to tip-substrate separation, which can sometimes occur in SECM. Furthermore, the resolution is simply governed by the dimensions of the pipette, opening up the possibility of readily confining a measurement to a single active site or region, as shown herein. Since micropipettes can be pulled readily with high reproducibility and their geometry characterized with high precision, a key feature of the technique is that experimental measurements can be supported by detailed simulations.

The measurements on basal plane HOPG reveal essentially uniform electroactivity across the surface. The electroactivity of the basal plane is far

greater than recently reported,[80, 82] based on macroscopic CV measurements. The electrode is critically important in determining the response of basal plane HOPG.[96] Here, we point out that for SMCM measurements the solution is only in contact with the region of the surface of interest for a brief time during which a CV measurement is made and that this is critically important.

Heterogeneity in electrode surface activity, as considered herein, is common in the field of electrochemistry. The SMCM technique represents a facile mean of examining the local redox activity of electrode materials. We have shown SMCM to be highly quantitative (e.g. very well defined mass transport) and we expect it to find widespread application.

REFERENCES

(1)   K. Kinoshita In *Carbon: Electrochemical and Physicochemical Properties*; Wiley: New York, 1988, pp 1.

(2)   Y. Pleskov, A. Sakharova, M. Krotova, L. Bouilov, B. Spitsyn *J. Electroanal. Chem.* **1987**, *228*, 19.

(3)   T. Kondo, Y. Einaga, B.V. Sarada, T.N. Rao, D.A. Tryk, A. Fujishima *J. Electrochem. Soc.* **2002**, *149*, E179.

(4)   S.J. Charles, J.W. Steeds, D.J.F. Evans, J.E. Butler *Mat. Lett.* **2003**, *57*, 3690.

(5)   M. Pagels, C.E. Hall, N.S. Lawrence, A. Meredith, T.G.J. Jones, H.P Godfried, C.S.J. Pickles, J. Wilman, C.E. Banks, R.G. Compton, L. Jiang *Anal. Chem.* **2005**, *77*, 3705.

(6)   A.O. Simm, C.E. Banks, S. Ward-Jones, T.J. Davies, N.S. Lawrence, T.G.J. Jones, L. Jiang, R.G. Compton *Analyst* **2005**, *130*, 1303.

(7)   B.V. Spitsyn, L.L. Bouilov, B.V. Derjaguin *J. Cryst. Growth* **1981**, *52*, 219.

(8)   G. Janssen, W.J.P. van Enckewort, W. Vollenberg, L.J. Giling *Diamond Relat. Mater.* **1992**, *1*, 789.

(9)   R. Samlenski, C. Haug, R. Brenn, C. Wild, R. Locher, P. Koidl *Diamond Relat. Mater.* **1996**, *5*, 947.

(10)   C.E. Hall, G.A, Scarsbrook; Element Six, 2005.

(11)   P.W. May *Phil. Trans. R. Soc. Lond. A* **2000**, *358*, 473.

(12)   T. Tachibana, B.E. Williams, J.T. Glass *Phys. Rev. B* **1992**, *45*, 11975.

(13)   J.V. Macpherson, P.R. Unwin *Anal. Chem.* **2000**, *72*, 276.

(14)   C.M. Welbourn, M. Cooper, P.M. Spear *Gems Gemol.* **1996**, *32*, 156.

(15)   J.V. Macpherson, P.R. Unwin *Anal. Chem.* **1997**, *69*, 5045.

(16)   K.B. Holt, A.J. Bard, Y. Show, G.M. Swain *J. Phys. Chem. B* **2004**, *108*, 15117.

(17)   R.D. Martin, P.R. Unwin *Anal. Chem.* **1998**, *70*, 276.

(18)   J. Kwak, A. Bard *Anal. Chem.* **1989**, *61*, 1221.

(19)   S. Cannan, I.D. Macklam, P.R. Unwin *Electrochem. Comm.* **2002**, *4*, 886.

(20)   N.C. Rudd, S. Cannan, E. Bitziou, I. Ciani, A.L. Whitworth, P.R. Unwin *Anal. Chem.* **2005**, *77*, 6205.

(21)   T. Yano, E. Popa, D.A. Tryk, K. Hashimoto, A. Fujishima *J. Electrochem. Soc.* **1999**, *146*, 1081.

(22)   M.T. McDermott, R.L. McCreery *Langmuir* **1994**, *10*, 4307.

(23)   K.R. Kneten, R.L. McCreery *Anal. Chem.* **1992**, *64*, 2518.

(24)   Bowyer, W. J.; Xie, J.; Engstrom, R. C. *Anal. Chem.* **1996**, *68*, 2005 - 2009.

(25)   Kranz, C.; Friedbacher, G.; Mizaikoff, B.; Lugstein, A.; Smoliner, J.; Bertagnolli, E. *Anal. Chem.* **2001**, *73*, 2491.

(26)   Macpherson, J. V.; Unwin, P. R. *Anal. Chem.* **2000**, *72*, 276.

(27)   Amemiya, S.; Bard, A. J.; Fan, F. R.-F.; Mirkin, M. V.; Unwin, P. R. *Annu. Rev. Anal. Chem.* **2008**, *1*, 95–131.

(28)   Bard, A. J.; Mirkin, M. V., Eds. *Scanning Electrochemical Microscopy*; Marcel Dekker: New York, 2001.

(29)   Bard, A. J.; Fan, F.-R. F.; Pierce, D. T.; Unwin, P. R.; Wipf, D. O.; Zhou, F. *Science* **1991**, *254*, 68-74.

(30)   P. Sun, F.O. Laforge, M.V. Mirkin *Phys. Chem. Chem. Phys.* **2007**, *9*, 802.

(31)   Wittstock, G.; Burchardt, M.; Pust, S. E.; Shen, Y.; Zhao, C. *Angew. Chem. Int. Ed.* **2007**, *46*, 1584.

(32)   J. Kwak, A.J. Bard *Anal. Chem.* **1989**, *61*, 1794.

(33)   R.C. Engstrom, M.Weber, D.J. Wunder, R. Burgess, S. Winquist *Anal. Chem.* **1986**, *58*, 844.

(34)   Kwak, J.; Bard, A. J. *Anal. Chem.* **1989**, *61*, 1221-1227.

(35)   S.B. Basame, H.S. White *J. Phys. Chem.* **1995**, *99*, 16430.

(36)   A.J. Bard, F-R. F. Fan, D.T. Pierce, P.R Unwin, D.O. Wipf, F. Zhou *Science* **1991**, *254*, 68.

(37)   Wipf, D. O.; Bard, A. J. *Anal. Chem.* **1992**, *64*, 1362-1367.

(38)   A. Schulte, S. Belger, M. Etienne, W. Schuhmann *Mater. Sci. Eng., A* **2004**, *378*, 523.

(39)   Eckhard, K.; Schuhmann, W. *Electrochimica Acta* **2007**, *53*, 1164-1169.

(40)   Díaz-Ballote, L.; Alpuche-Aviles, M.; Wipf, D. O. *Journal of Electroanalytical Chemistry* **2007**, *604*, 17-25.

(41)   Wilson, N. R.; Guille, M.; Dumitrescu, I.; Fernandez, V. R.; Rudd, N. C.; Williams, C. G.; Unwin, P. R.; Macpherson, J. V. *Analytical Chemistry* **2006**, *78*, 7006-7015.

(42)   Basame, S. B.; White, H. S. *Anal. Chem.* **1999**, *71*, 3166.

(43)   Basame, S. B.; White, H. S. *Langmuir* **1999**, *15*, 819.

(44)   I. Serebrennikova, S. Lee, H.S. White *Faraday Discuss.* **2002**, *121*, 199.

(45)   A.J. Bard, F.Fan, J. Kwak, O. Lev *Anal. Chem.* **1989**, *61*, 132.

(46)   M.A. Edwards, S. Martin, A.L. Whitworth, J.V. Macpherson, P.R. Unwin *Physiol. Meas.* **2006**, *27*, R63.

(47)   Unwin, P. R.; Bard, A. J. *J. Phys. Chem.* **1992**, *96*, 5035-5045.

(48)   Martin, R. D.; Unwin, P. R. *J. Chem. Soc., Faraday Trans.* **1998**, *94*, 753-759.

(49)   C. Demaille, P.R. Unwin, A.J. Bard *J. Phys. Chem.* **1996**, *100*, 14137.

(50)   M. Mirkin, F. Fan, A.J. Bard *J. Electroanal. Chem.* **1992**, *328*, 47.

(51)   N.J. Gray, P.R. Unwin *Analyst* **2000**, *125*, 889.

(52)   B.B. Kateman, W. Schuhmann *Electroanalysis* **2002**, *14*, 22.

(53)   Y. Shao, M.V. Mirkin, G. Fish, S. Kokotov, D. Palanker, A. Lewis *Anal. Chem.* **1997**, *69*, 1627.

(54)   P. Sun, M.V. Mirkin *Anal. Chem.* **2006**, *78*, 6526.

(55)   P. Sun, F.O. Laforge, T.P. Abeyweera, S.A. Rotenberg,J. Carpino, M.V. Mirkin *Proc. Nat. Acad. Sci.* **2008**, *105*, 443.

(56)   Tel-Vered, R.; Walsh, D. A.; Mehrgardi, M. A.; Bard, A. J. *Anal. Chem.* **2006**, *78*, 6959.

(57)   M. Etienne, E.C. Anderson, S.R. Evans, W. Schuhmann, I. Fritsch *Anal. Chem.* **2006**, *78*, 7317.

(58)   T. Suter, H. Böhni *Electrochim. Acta* **1997**, *42*, 3275.

(59)   T. Suter, H. Böhni *Electrochim. Acta* **1998**, *43*, 2843.

(60)   F. Assi, H.Böhni *Wear* **1999**, *233*, 505.

(61)   H. Böhni, T. Suter, F. Assi *Surface and Coatings Technology* **2000**, *130*, 807.

(62)   A. Hassel, M. Lohrengel *Electrochim. Acta* **1997**, *42*, 3327.

(63)   M. Lohrengel, C. Rosenkranz, I. Kluppel, A. Moehring, H. Betteremann, B. Van den Bossche, J. Deconinck *Electrochimica Acta* **2004**, *49*, 2863.

(64)   L. Eng, E. Wirth, T. Suter, H. Bohni *Electrochim. Acta* **1998**, *43*, 3029.

(65)   P.K. Hansma, B. Drake, O. Marti, S.A.C. Gould, C.B. Prater *Science* **1989**, *243*, 641-643.

(66)   C.B. Prater, P.K. Hansma, M. Tortonese, C.F. Quate *Rev. Sci. Instrum.* **1991**, *62*, 2634-2638.

(67)   Y.E. Korchev, M. Milovanovic, C.L. Bashford, D.C. Bennett, E.V. Sviderskaya, I. Vodyanoy, M.J. Lab *J Microsc-Oxford* **1997**, *188*, 17-23.

(68)   Y.E. Korchev, C.L. Bashford, M. Milovanovic, I. Vodyanoy, M.J. Lab *Biophys J* **1997**, *73*, 653-658.

(69)   Y.E. Korchev, J.Gorelik, M.J. Lab, E.V. Sviderskaya, C.L. Johnston, C.R. Coombes, I. Vodyanoy, C.R.W. Edwards *Biophys J* **2000**, *78*, 451-457.

(70)   D. Pastre, H. Iwamoto, J. Liu, G. Szabo, Z.F. Shao *Ultramicroscopy* **2001**, *90*, 13-19.

(71)   A.I. Shevchuk, J. Gorelik, S.E. Harding, M.J. Lab, D. Klenerman, Y.E. Korchev *Biophys J* **2001**, *81*, 1759-1764.

(72)   J. Gorelik, Y.J. Zhang, A.I. Shevchuk, G.I. Frolenkov, D. Sanchez, M.J. Lab, I. Vodyanoy, C.R.W. Edwards, D. Klenerman, Y.E. Korchev *Mol Cell Endocrinol* **2004**, *217*, 101-108.

(73)   L.M. Ying, S.S. White, A. Bruckbauer, L. Meadows, Y.E. Korchev, D. Klenerman *Biophys J* **2004**, *86*, 1018-1027.

(74)   W. Shin, K.D. Gillis *Biophys J* **2006**, *91*, L63-L65.

(75)   E.N. Ervin, H.S. White, L.A. Baker, C.R. Martin *Anal. Chem.* **2006**, *78*, 6535.

(76)   D.A. Walsh, J.L. Fernández, J. Mauzeroll, A.J. Bard *Anal. Chem.* **2005**, *77*, 5182.

(77)   A. Hengstenberg, C. Kranz, W. Schuhmann *Chem. Eur. J.* **2000**, *6*, 1547.

(78)   L.M. Ying, A. Bruckbauer, D.J. Zhou, J. Gorelik, A. Shevchuk, M.Lab, Y. Korchev, D. Klenerman *Phys Chem Chem Phys* **2005**, *7*, 2859-2866.

(79)   K.T. Rodolfa, A. Bruckbauer, D.J. Zhou, Y.E. Korchev, D. Klenerman *Angew Chem Int Edit* **2005**, *44*, 6854-6859.

(80)   C.E. Banks, T.J. Davies, G.G. Wildgoose, R.G. Compton *Chem. Comm.* **2005**, *7*, 829.

(81)   M.T. McDermott, K. Kneten, R.L.McCreery *J. Phys. Chem. B* **1992**, *96*, 3124.

(82)   Davies, T. J.; Hyde, M. E.; Compton, R. G. *Angew. Chem.* **2005**, *117*, 5251.

(83)   K. Kneten Cline, M.T. McDermott, R.L. McCreery *J. Phys. Chem.* **1994**, *98*, 5314.

(84)   C.E. Banks, R.R. Moore, T.J. Davies, R.G. Compton *Chem. Comm.* **2004**, *16*, 1804.

(85)   Banks, C. E.; Compton, R. G. *Anal. Sci.* **2005**, *21*, 1263.

(86)   Y. Liu, M.S. Freund *Langmuir* **2000**, *16*, 283.

(87)   Fleming, B. D.; Bell, S. G.; Wong, L.-L.; Bond, A. M. *J. Electroanal. Chem.* **2007**, *611*, 149.

(88)   Bowling, R. J.; Packard, R. T.; McCreery, R. L. *J. Am. Chem. Soc.,* **1989**, *111*, 1217-1223.

(89)   R.S. Robinson, K. Sternitzke, M.T. McDermott, R.L. McCreery *J. Electrochem. Soc.* **1991**, *138*, 2412.

(90)   M.N. Szentirmay, C.R. Martin *Anal. Chem.* **1984**, *56*, 1898.

(91)   H. Chang, A.J. Bard *Langmuir* **1991**, *7*, 1143.

(92)   http://www.2spi.com/catalog/new/hopgsub.shtml.

(93)   D.S. Burnett *Finite Element Analysis*; Addison-Wesley: USA, 1987.

(94)   A.J. Bard, L.R. Faulkner *Electrochemical Methods: Fundamentals and Applications*; Wiley: New York, 2001, p152.

(95)   C.M.A. Brett, A.M.O. Brett *Electrochemistry: Principles, Methods and Applications*; Oxford University Press: Oxford, 2000, p. 74.

(96)   Guille, M., et al *in preparation*.

Conclusions

The overall aim of this thesis was to examine the underlying physical basis of dentinal hypersensitivity and to assess methods of treating this cause using imaging techniques. The scanned probe microscopy (SPM) techniques ware then extended to the study of carbon-based electrode surfaces, as described in the final chapter.

SECM and SICM have been shown to be powerful techniques for imaging dentine. SECM was utilised in order to investigate the effect of blocking agents on the flow of fluid, namely a redox mediator, through the dentine substrate. The results obtained using SECM suggest that alginate may be an effective active for the occlusion of dentinal tubules across a range of pH values. SICM has been developed and calibrated using two substrates, and has allowed high resolution images of dentine to be obtained. There is much scope for further development of this technique and in future it may be applied to investigate the movement of ions across the dentine substrate.

LSCM has been shown to be a sensitive means of visualising fluid flow through dentine over relatively large areas, and for evaluating the effect of surface treatments on flow. The capacity of the technique for capturing time series is of particular use for observing the dynamic action of certain treatments. By combining the fluorescence data with pressure–time data, it is possible to elucidate further information about the system in question. This enhanced understanding of the nature of fluid flow and of the effect of occlusion agents on

this flow will be valuable in the development of more effective treatments for dentinal hypersensitivity. The new technique is versatile and has the capacity to be applied to other areas concerned with the flow of fluid through a substrate or membrane. The studies herein have shown that brushing the dentine caused higher levels of fluorescence over the time period of the experiment, hence it may be concluded that brushing the dentine allows more facile flow, by opening up tubules that may have remained occluded after acid etching. The pressure–time data obtained lends further support: there was a much smaller increase in pressure for brushed dentine than for unbrushed dentine over a 120 s experimental period. In contrast, the commercial varnish (Cervitec®) occluded the vast majority of the tubules, as evidenced by the fluorescence data (which showed no flow) and pressure–time data recorded for these samples. The placebo paste and alginate paste both occluded the tubules to a certain extent, but under pressures in excess of 6 kPa, material deposited on the surface to occlude flow was expelled from the dentine into the receptor solution. It should be noted that the natural pressure across dentine in the oral cavity is estimated to be *ca.* 2 kPa19 and so these pastes are likely to withstand this. The alginate paste resulted in a larger increase in pressure than the placebo paste, and thus alginate appears to be a successful candidate for the treatment of dentinal hypersensitivity.

Localised dissolution of dental enamel has been achieved by the application of a proton flux to the enamel surface from a UME positioned in close proximity to the enamel, in aqueous solution. The etch pits characteristic of this approach may be analysed using optical microscopy, white light interferometry and other techniques. Measurements can give information on the nature of the dissolution

of the enamel, and the effect of inhibitors, such as fluoride, on this dissolution. It has been shown that fluoride causes changes in the morphology of the etch pits that form. Preliminary simulations reveal that the etching process in a solution of 0.1 M KNO_3 occurs at a diffusion-limited rate.

BDD microdisc array electrodes, insulated within an intrinsic diamond matrix, represent an important advance in the development of array electrodes. The arrays make use of the interesting properties of BDD in a coplanar configuration, and may be cleaned repeatedly using standard mechanical polishing procedures. Each BDD microdisc contains polycrystalline BDD with a variety of different grains exposed, as elucidated using C-AFM. SECM measurements revealed that even under apparent diffusion-limited conditions (as determined by CV experiments) the response varies slightly between individual electrodes, with some showing heterogeneous electroactivity. However, under these conditions, most electrodes demonstrate predominantly metallic behaviour.

Importantly, at applied potentials below the diffusion-limited regime, significant spatial variations in the electroactivity of individual electrodes are observed. Spatially heterogeneous electron-transfer rates are seen, and are likely to be linked to the underlying wide variations in intrinsic conductivity of individual grains. These variations cannot readily be determined from conventional, bulk-scale characterisation methods, such as CV, but are trivially visualised using SECM and FE-SEM imaging of silver deposition at the BDD microdiscs. The results described herein suggest that BDD microdisc arrays of this type can be used for diffusion-limited amperometric detection, but also suggest that caution

is advised for analysis of voltammetric wave shapes. In this case, an understanding of the underlying conductivity and spatial variations in electrode activity is required; at potentials shy of the diffusion-limited regime, differences in the turnover rate of electroactive species resulting from variations in the electron-transfer rate constant across a microelectrode surface are accentuated. It is clear that this factor would impact on the analysis of the voltammetric wave shape, as conventional models for microelectrodes assume a uniform rate constant across a surface.

SMCM has proven a valuable tool for probing the localised electroactivity of heterogeneous electrode surfaces. The small dimensions of the micropipette probe allow voltammetric measurements to be made in microscopic regions of an electroactive surface. In SMCM, the tip converges on the surface and so there are no issues related to tip-substrate separation, which can sometimes occur in SECM. Furthermore, the resolution is simply governed by the dimensions of the pipette, opening up the possibility of readily confining a measurement to a single active site or region, as shown herein. Since micropipettes can be pulled readily with high reproducibility and their geometry characterized with high precision, a key feature of the technique is that experimental measurements can be supported by detailed simulations.

The measurements on basal plane HOPG reveal essentially uniform electroactivity across the surface. The electroactivity of the basal plane is far greater than recently reported, based on macroscopic CV measurements. Here, we point out that for SMCM measurements the solution is only in contact with

the region of the surface of interest for a brief time during which a CV measurement is made and that this is critically important.

Heterogeneity in electrode surface activity, as considered herein, is common in the field of electrochemistry. The SMCM technique represents a facile mean of examining the local redox activity of electrode materials. We have shown SMCM to be highly quantitative (e.g. very well defined mass transport) and we expect it to find widespread application.

Overall the aims of this thesis have been achieved. SECM and LSCM have proved to be valuable tools in the analysis of fluid flow through dentine and the effect of treatments on this flow. SICM has shown to be a promising technique for imaging dentine. Localised dissolution of enamel has complemented the studies into dentinal hypersensitivity. The heterogeneities of carbon electrode surfaces have been explored using established techniques, and the new technique of SMCM has been introduced.